

Force Spectroscopy with Optical and Magnetic Tweezers

Richard Conroy

1 Introduction

Micromanipulation of individual cells and molecules is increasingly important for a wide range of biophysical research because, although ensemble biochemical analysis provides excellent qualitative and quantitative descriptions, it seldom describes phenomena at the molecular level. By observing the force spectroscopy of single molecules, the kinetics, mechanics, and variation of structure, function, and interactions can be fully explored to provide a more complete physiological picture.

The use of electric and magnetic fields for manipulating particles dates back more than a century, with a rich tapestry of applications in separation, filtering and trapping. Recognizing the non-contact advantages of magnetic manipulation, Crick and Hughes probed the physical properties of a cell's cytoplasm more than fifty years ago using magnetic particles [1]. Two decades later, with the development of intense electromagnetic fields from lasers, the manipulation of latex particles with light was experimentally demonstrated by Ashkin in 1970 in his "levitation traps" [2]. Ashkin went on to pioneer optical trapping of both atoms and biomolecules, leading to one of the most successful technology transfers from a physics lab to cell biology.

For many applications, in particular for characterizing biomolecules and their interactions, it is desirable to have a non-contact technique for exerting a force. A non-contact technique allows the behavior of a single molecule under stretching or torsional forces to be measured and manipulated without complicating surface effects or material response limitations. Non-contact techniques also benefit from being easier to multiplex into exerting force on multiple sites of the same molecule or multiple heterogeneous molecules, or to collect parallel statistics on homogeneous copies of the same system. In general they are not limited by access constraints to the interaction volume, and therefore integrate more readily with the desired environmental conditions and other imaging and spectroscopic techniques. For these reasons, and practical reasons such as low cost and biocompatibility, optical and magnetic tweezers have become prominent methods for manipulating and measuring single biological entities and their interactions.

To experience a force in an optical or magnetic field, a molecule must possess either dielectric or magnetic contrast against the surrounding medium. Often the entity under observation does not have favorable intrinsic properties either for imaging or for generating a force, and it is necessary or desirable to label the molecule with a particle or tag to improve contrast. These particles or tags can be multifunctional, acting passively as a position and force sensor and actively as a handle through which a force can be exerted on the attached molecule.

To carry out single-molecule measurements of biological structures and processes requires detection of nanometer displacements and piconewton forces with millisecond resolution. These imaging requirements can be realized using a microscope equipped with CCD cameras and photodiodes, while optical and magnetic tweezers can generate forces in the range 0.1 to 200 pN, making this approach ideal for single-molecule biophysics.

The first half of this chapter will focus on the basic science and the technologies involved in generating these forces using optical and magnetic fields and how force at the piconewton level and displacement at the nanometer scale can be measured. Optical and magnetic tweezers complement other single-molecule manipulation techniques, as detailed in Table 1, by providing extremely sensitive, non-contact manipulation. At one extreme, contact force transducers have high spatial resolution and applied force capabilities. Furthermore, probe tips can be used to provide high resolution chemical and electrostatic information. At another extreme, the global force from fluid flow or an electric field is advantageous in manipulating ensembles of particles using their intrinsic properties. Optical and magnetic tweezers have many of the advantages of either extreme, for example being able to trap multiple particles, and can be readily combined with the other techniques to exploit their relative advantages for the requirements of the system under study.

The energies involved in determining the structure and interactions of biomolecules are carefully balanced to be stable against thermal fluctuations, yet pliable compared to more permanent covalent and ion bonds as illustrated in Figure 1. From a cellular perspective, molecules are ideally reconfigurable using the energy available from nucleotide triphosphate (NTP) hydrolysis, the most common fuel source. Hydrogen bonds ($\sim 2\text{--}7 k_B T$), hydrophobic interactions ($1\text{--}5 k_B T$), and electrostatic forces ($0.2\text{--}10 k_B T$) have an energy $1\text{--}30 \text{ pN nm}$ whereas covalent bonds ($\sim 100 k_B T$) and strong ligand-receptor binding ($\sim 20\text{--}35 k_B T$) have energies at least an order of magnitude higher, in the range $\sim 80\text{--}2000 \text{ pN nm}$. Clearly, hydrolysis of individual ATPs ($\sim 20 k_B T$) provides sufficient energy to separate low energy bonds, to reconfigure molecules and drive interactions without disrupting covalent bonds. Optical and magnetic tweezers can produce forces up to 200 pN, which for non-covalent bonds of length of order one nanometer, is sufficient to study

Table 1. Comparison of force spectroscopy techniques.

	Magnetic Tweezers	Optical Tweezers	Electrophoresis	AFM	Micropipette	Fluid Flow
Type	Global/ Point	Point	Global	Point	Point	Global
	Non-Contact	Non-Contact	Non-Contact	Contact	Contact	Non-Contact
Force Range (pN)	0.1–200	0.1–200	0.01–50	10– 100000	1–1000	0.1–1000
3D Trap	Yes	Yes	No	Yes	Yes	No
Stiffness (pN nm^{-1})	$10^{-6} - 0.1$	$10^{-6} - 0.1$	-	10–10000	0.01–1000	-
Energy Dissipation	No	Yes	Yes	No	No	No
Surface Considerations	No	No	No	Yes	Yes	No
Low Cost	Yes	Yes	Yes	No	Yes	Yes
Parallel	Yes	Yes	Yes	No	No	Yes
Access inside a cell	Yes	Yes	Yes	No	No	No
Self-assembly	Yes	No	Yes	No	No	No

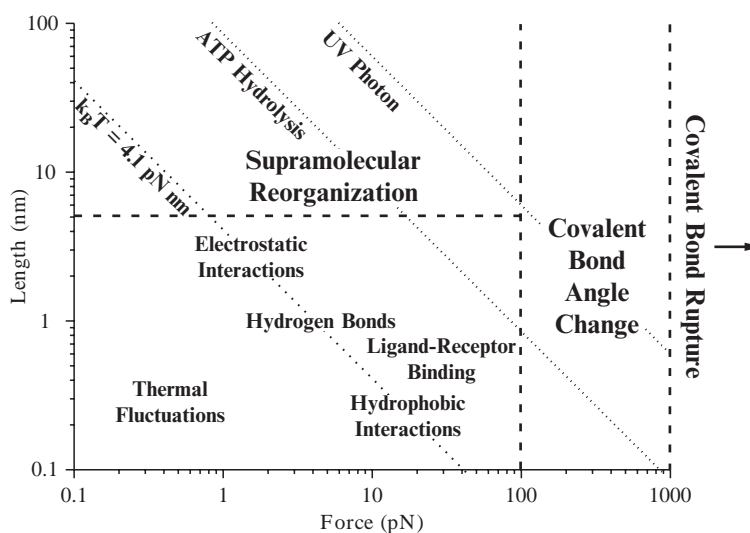


Figure 1. Forces and length scales involved in biomolecular organization. The dotted lines represent the energies associated with thermal noise ($k_B T$), ATP hydrolysis, and a UV photon.

all the processes normally fuelled by NTP hydrolysis. It is worth noting that visible and ultraviolet photons ($\sim 70\text{--}150k_B T$) carry sufficient energy to disrupt nearly all types of bonds if directly absorbed and provide an important limitation to any form of optical imaging. These energy scales provide the setting for the second half of this chapter, which will focus on the force spectroscopy measurements which have been carried out using optical and magnetic tweezers on intracellular biomolecules and their interactions as well as cellular level mechanics and interactions.

2 Optical Tweezers

2.1 Introduction

The effect of light on matter has been known for over four hundred years, dating from Kepler's observation that comet tails always point away from the sun. Indeed, light from the sun can exert a pressure up to $5\text{ }\mu\text{N/m}^2$ on a totally reflecting surface, ten orders of magnitude less than the force on a cube of the same dimensions due to gravity on the earth's surface. Although resulting in an extremely small force, radiation pressure from sunlight can be significant, for example as the driving force behind solar sails where gravity is negligible. At the beginning of the twentieth century, using thin plates suspended in a evacuated radiometer, Lebedev [3] was the first to experimentally measure the radiation pressure proposed by Maxwell-Bartoli, showing that the pressure for a reflective surface is twice that of an absorbing surface. In 1969 Arthur Ashkin at Bell Laboratories realized that the radiation pressure from an intense laser was sufficient to manipulate dielectric particles [2], demonstrating levitation by balancing radiation pressure with gravity or by using multiple beams. While an axial force on particles in a laser beam was understood in terms of radiation pressure, a radial trapping force was unexpected and it was the 1980s before Ashkin and colleagues showed that a single focused beam could create a three-dimensional optical trap [4]. Following this revelation, demonstrations of the trapping and manipulation of viruses [5] and cells [6] quickly followed, blossoming over the last twenty years into the ubiquitous "optical tweezers."

Optical tweezers are technically a subset of dielectrophoretic (DEP) traps, where an alternating electromagnetic field is used to create a force on objects with dielectric contrast against the surrounding medium, trapping particles of interest at either a maximum (positive trap) or minimum (negative trap) in the field intensity. However, DEP traps typically refer to geometries using two or more electrodes and operating at a frequency below 100 GHz. These traps can be inexpensively microfabricated and used to characterize and trap a wide variety of molecules, cells, and particles [7]. Although terahertz [8] and mid-infrared [9] frequencies are used for spectroscopy, they have not been used for detecting and trapping single biomolecules, providing a clear distinction between the low frequency electrode traps and the purely optical, high frequency traps. Although the higher optical frequencies provide the greatest intensity and the smallest trapping volumes, terahertz and mid-infrared tweezers may have advantages in addressing specific bonds and in cell characterization.

The basis for a dielectric trapping force originates in the polarizability of a particle in an electromagnetic field. From Earnshaw's theorem it is known that a charged particle cannot be held at rest purely by electrostatic fields in free space, yet DEP traps in general and optical tweezers specifically form a stable three-dimensional trap. These traps are stable because the field gradient is three-dimensional, dynamic and not dominated by the scattering force. However, it should be noted that even for simple one-dimensional gradient fields, for example in attractive force magnetic tweezers, stability can be achieved by using a second unrelated force, (e.g., fluid flow) or by modifying the boundary conditions (e.g., at a fluid interface). Nevertheless the unique ability of optical tweezers to form a stable, three-dimensional trap in free space without feedback has been a powerful motivation factor in their adoption beyond specialized physics laboratories.

In recent years, optical tweezers have matured into several commercial products (e.g., Cell Robotics Inc., Arrayx Inc., PALM Microlaser Technologies, Elliot Scientific); however, laboratory setups are still at the cutting edge of development, exploiting new methods of light generation, manipulation, and detection, particularly through advances in nanopositioning and optics. In the past decade the range of biologically inspired problems to which optical tweezers have been applied has greatly expanded from cell sorting and classification [10] to intracellular surgery [11] and so-called optical scalpels and scissors [12]. Although not considered here in detail, optical tweezers have also found application in more traditional areas of physics from self-assembly [13] and photolithography [14] to probing for violations of the second law of thermodynamics [15]. There is a rich variety of force interactions which can be probed from colloids [16] to actuators and small turbines driven by light [14], covered in more detail in many of the comprehensive review articles on optical trapping [17, 18, 19]. However, the focus for this section is on the basic science behind how force is generated in an optical trap and how it can be calibrated and used to characterize the force spectroscopy of biomolecules.

2.2 Theory of Radiation Pressure

The interaction between light and matter is a complicated one which is not understood fully for all cases, but informative approximations are available under a number of limits. The origin of a force on matter because of an electromagnetic wave can be understood qualitatively by an electric field exerting a force on charges within a particle, and a magnetic field exerting a force on currents. From Maxwell's equations, an electromagnetic field in a vacuum exerts a force:

$$\begin{aligned} F_{\text{mech}}(r,t) &= q[E(r,t) + v(r,t) \times B(r,t)] \\ &= \int_V [\rho(r,t)E(r,t) + j(r,t) \times B(r,t)] dV \end{aligned} \quad (1)$$

on a single charge, q , moving with velocity $v(r,t)$ in the first expression and a distribution of charges in the second, satisfying the charge conservation law. The conservation of linear momentum in an arbitrary volume V around the charges gives:

$$\frac{d}{dt} [P_{field}(r,t) + P_{mech}(r,t)] = \int_V \nabla \cdot T dV \quad (2)$$

where $F_{mech} = \frac{d}{dt} P_{mech}$ and the field momentum is $P_{field} = \frac{1}{c^2} \int_V [E \times H] dV$.

Assuming a particle has the linear relationships $D = \epsilon E$ and $B = \mu H$, the Maxwell stress tensor, T , can be written as:

$$T = \frac{1}{4\pi} \left[\epsilon \epsilon_0 E E - \mu \mu_0 H H - \frac{1}{2} (\epsilon \epsilon_0 E^2 - \mu \mu_0 H^2) \delta \right] \quad (3)$$

where δ is the Kronecker delta function. The field momentum is zero when it is averaged over one oscillation period; and applying the Gauss integration law, the time-averaged force becomes:

$$\langle F \rangle = \int_V \nabla \cdot T dV = \int_{\delta V} \langle T(r,t) \rangle \cdot n(r) da \quad (4)$$

where δV is the surface of V , $n(r)$ is the unit element perpendicular to the surface, and da is a surface element. This equation, using a generalized Maxwell stress tensor, is generally applicable and is only constrained by assuming the particle is rigid.

The radiation pressure, P , can be found from integrating Maxwell's stress tensor on an infinite planar surface A , perpendicular to the Poynting vector direction z :

$$P n_z = \frac{1}{A} \int_A \langle T(r,t) \rangle \cdot n_z da \quad (5)$$

Assuming an incident plane wave $\left(I_0 = \frac{1}{2} c \epsilon_0 E_0^2 \right)$ interacting with a particle with complex reflection coefficient R , the electric field outside the particle can be written as a superposition of two counter-propagating waves:

$$E(r,t) = E_0 \operatorname{Re} \left[\left(e^{ikz} + R e^{-ikz} \right) e^{-i\omega t} \right] n_x \quad (6)$$

and using Maxwell's equations, the magnetic field is:

$$H(r,t) = \sqrt{\frac{\epsilon_0}{\mu_0}} E_0 \operatorname{Re} \left[\left(e^{ikz} - R e^{-ikz} \right) e^{-i\omega t} \right] n_y \quad (7)$$

Under these conditions the Maxwell stress tensor reduces to:

$$\langle T(r,t) \rangle \cdot n_z = -\frac{1}{2} \langle \epsilon_0 E^2 + \mu_0 H^2 \rangle n_z = \frac{\epsilon_0}{2} E^2 [1 + |R|^2] n_z \quad (8)$$

And the radiation pressure on the particle can be expressed as:

$$P = \frac{I_0}{c} [1 + |R|^2] \quad (9)$$

As observed experimentally by Lebedev, the pressure on a perfectly absorbing body ($R = 0$) is half of that for a perfectly reflecting particle ($R = 1$). While many objects have irregular

shapes and nonlinear response and are illuminated by a complex spatial, spectral, and temporal light source, this approach of simple integration of the Maxwell stress tensor provides a good approximation for computing the forces on dielectric spheres trapped by optical tweezers.

It is intuitively helpful to consider the two component forces in an optical trap, the gradient force and the scattering force, independently. Generally both forces are present in a light beam but the scattering force dominates, exerting a force in the direction of propagation of the light. However, by tightly focusing a near diffraction limited light source, the gradient force created is sufficient to overcome the scattering force and form a trap at the region of highest intensity.

More in-depth analysis of the approximations and limitations in modeling optical traps have been discussed extensively in a number of publications [20, 21, 22], though to gain an insight into their basic operation and optimization we will consider the two component forces (gradient and scattering force) and the two scaling limits (Rayleigh and ray optic regimes).

2.2.1 The Gradient Force

Light incident on a particle creates a dielectric response, due to the polarizability of the constituent atoms or ions. For one of these atoms or ions in a monochromatic, linearly polarized, continuous light field, E , the time-averaged induced dipole moment is:

$$p = \alpha E \quad (10)$$

where $\alpha = \alpha' + i\alpha''$ is the relative complex polarizability of the particle to the surrounding medium. The interaction of the induced dipole with the electric field of the light creates an electrostatic potential:

$$U = -p \cdot E \quad (11)$$

Thus in a light field with a spatially varying intensity, there is a gradient force:

$$F_{grad} = -\nabla U = -p \cdot \nabla E = -\alpha (E \cdot \nabla) E \quad (12)$$

For a small particle of radius r_p , this leads to the force relation [4]:

$$F_{grad} = -\frac{n_m^3 r_p^3}{2} \left(\frac{n_c^2 - 1}{n_c^2 - 2} \right) \nabla E^2 \quad (13)$$

Thus the gradient force is linearly dependent on the spatial variation of the intensity of the light field and on the dielectric contrast of the particle to be trapped relative to the surrounding media, which can be described by the Clausius-Mossotti relation. For particles with a refractive index higher than the surrounding medium, the gradient force acts toward the point of highest intensity, that is to say the focal point of a diffraction-limited beam in optical tweezers. Conversely, particles with a lower refractive index can be trapped at a minimum in the light field intensity.

The strength of the restoring gradient force in an optical trap of radius r can be characterized as a Hookean spring with stiffness, κ , where the force is linearly proportional to small displacements ($d < r/2$):

$$F = -\kappa \cdot r \quad (14)$$

and the trap period, a measure of correlation time, is:

$$\tau_0 = \frac{6\pi\eta r_p}{\kappa} \quad (15)$$

where η is the viscosity of the surrounding medium. A schematic of the axial and radial potentials and their resulting stiffnesses is shown in Figure 2.

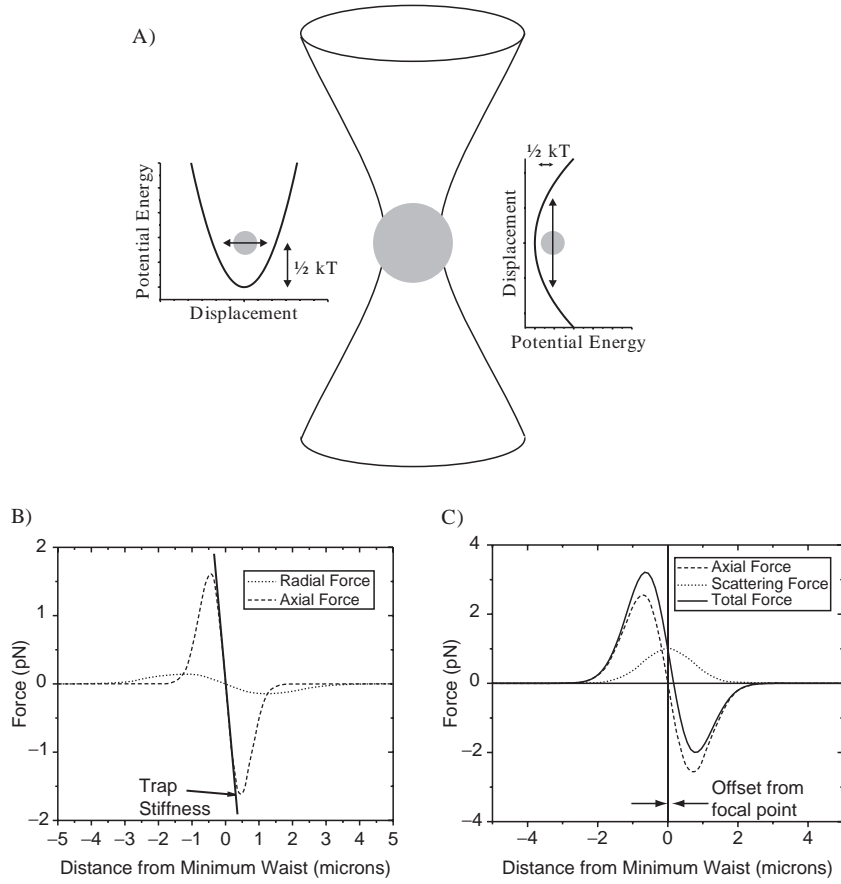


Figure 2. (A) The axial and radial trapping potentials of a bead in an optical trap lead to (B) differing stiffnesses and extents. (C) With the addition of the scattering force, the trap center is offset from the focal point.

Techniques for measuring the stiffness of an optical trap are described later, but for a $1\text{ }\mu\text{m}$ diameter polystyrene bead in a typical optical tweezers setup, the stiffness can be varied easily in the range 10^{-6} – 0.1 pN/nm by adjusting the laser power from 10 – 1000 mW . These characteristics complement the stiffness of physical cantilevers such as AFM tips (10 – 10^4 pN/nm), which cannot be as easily tuned after fabrication. The trap stiffness is important in determining the minimum force which can be measured through displacement detection and sets an upper limit for the maximum useful sampling rate through the trap frequency. Although not immediately obvious from these simple expressions, the trap stiffness is greatest when the particle to be trapped is the same size as the beam waist; as particle size decreases, the restoring force decreases rapidly, but decreases only modestly when the particle size increases.

2.2.2 The Scattering Force

The second force component in an optical trap arises from the scattering of light and is a consequence of photons having momentum. This force acts in the direction of propagation of the light and is dependent on the light intensity rather than the gradient. The momentum of a single photon of energy E is:

$$p = \hbar k = \frac{h}{\lambda} = \frac{En_m}{c} \quad (16)$$

A beam of incident photons can be scattered from the particle, resulting in two impulses: one along the direction of light propagation, and the other opposite the direction of the scattered photon. For isotropic scattering, dependent on the size of the particle, the latter impulse has no preferred direction and results in a net force in the direction of light propagation.

The change in momentum, or force, of a particle can be calculated by considering the photon flux impinging on and leaving an object under the conservation of momentum:

$$F_{scat} = \frac{n}{c} \iint (S_{in} - S_{out}) dA = \frac{n_m \sigma \langle S \rangle}{c} \quad (17)$$

where n_m is the refractive index of the surrounding medium, $\langle S \rangle$ is the time-averaged Poynting vector, c is the speed of light, and σ is the particle's optical cross section. In the case of a small, spherical, dielectric particle, the Rayleigh scattering cross-section is:

$$\sigma = \frac{8}{3} \pi \left(\frac{2\pi n_m}{\lambda} \right)^4 r_p^6 \left(\frac{n_c^2 - 1}{n_c^2 + 2} \right)^2 \quad (18)$$

where r_p is the particle radius, $n_c = \frac{n_p}{n_m}$ is the refractive index contrast between the particle (n_p) and the medium (n_m), and $k = \frac{2\pi}{\lambda}$ is the wave vector of the trapping light. The scattering force on a Rayleigh particle can then be written in terms of the light intensity I_0 [4]:

$$F_{scat} = \frac{128\pi^5 r_p^6}{3\lambda^4} \left(\frac{n_c^2 - 1}{n_c^2 + 2} \right)^2 \frac{n_m I_0}{c} \quad (19)$$

Thus the scattering force is dependent on the photon flux or light intensity, the wavelength of the trapping light, the particle size, and its refractive index contrast against the liquid in which it is immersed.

For larger particles ($r_p \gg \lambda$), the scattering cross-section can be expressed as $\sigma = Q_{scat} \pi r_p^2$ where Q_{scat} approaches the limit of 2. However, for intermediate sizes, an accurate force estimate needs to be numerically evaluated using Mie theory [23], in part because the scattering of incident photons is no longer isotropic.

To maximize the gradient force, the particle's radius should be comparable to the wavelength of the trapping laser and its associated minimum focal spot size and consequently is most appropriately described by the intermediate, Mie regime. The need to numerically solve Mie scattering theory is one of the complications in developing a simple model for optical tweezers and makes direct comparison of the gradient force and scattering force difficult. However, one variable which can be controlled and optimized is the refractive index contrast between the trapped particle and the surrounding medium. The optimal refractive index contrast is 1.2–1.3, which maximizes the gradient force with respect to the scattering force to $F_{max} = \frac{0.49 n_m P}{c}$ for the incident optical power P . Conveniently, polystyrene beads in water have a refractive index contrast of $n_c = 1.59/1.33 = 1.2$, close to optimal, with a potential maximum force of $F_{max} = 2.2$ pN/mW, though optical tweezers generally operate at around 2/3 of this value [24].

Adding the two force components results in the equilibrium position for an optical trap being displaced a distance proportional to the light intensity from the minimum beam waist in the direction of the light propagation, typically 100–500 nm, and illustrated in Figure 2c. This distance can be found experimentally by translating a trapped bead into a surface and measuring the displacement of the bead in the trap when it is in the focal plane of the surface, or comparing it to a bead previously fixed to the surface.

2.2.3 Rayleigh Regime ($r \ll \lambda$)

In the two particle size limits, the Rayleigh regime ($r \ll \lambda$) and the ray optics regime ($r \gg \lambda$), a theoretical treatment for calculating the radiation pressure is relatively straightforward and provides a number of useful insights.

In the Rayleigh regime, particles can be treated as a collection of dipoles polarized by the envelope of the light field forming the trap, with the phase of the field being approximately constant throughout the particle. In the previous sections, equations were presented for the gradient and scattering forces on small dielectric particles; however, in practice, it is difficult to exert sufficient force to trap a dielectric particle below 100 nm in size with current optics and laser limitations. As particle size increases, the difference between Rayleigh and Mie scattering becomes measurable for particles larger than 200 nm for visible trapping fields [25], and Rayleigh approximations break down for most trappable objects.

However, exploiting a nonlinearity such as a plasma resonance, ionic resonance, or intensity dependent refractive index, using a microstructured meta-material or reduction of homogeneous and inhomogeneous broadening can enhance the dielectric contrast to trap particles down to 5 nm in size [26]. Alternatively, the medium surrounding the particle can be modified to minimize Brownian motion to the extreme of trapping and cooling small numbers of atoms in an ultrahigh vacuum chamber [27]. In general, however, the complications and limitations associated with these approaches mean that optical traps rarely operate in a pure Rayleigh regime, and predictions can be inaccurate without experimental validation.

2.2.4 Ray Optics Regime ($r \gg \lambda$)

In the other limiting case, where the size of the particle to be trapped is much larger than the wavelength of light, and has a small refractive index contrast with the surrounding medium, the component forces can be modeled using ray optics. An incident monochromatic light beam can be decomposed into individual rays with appropriate intensity, momentum, and direction. In a uniform, nondispersive media these rays propagate in a straight line and can be described by geometric optics. For a uniform dielectric sphere the optical forces, including the scattering component, can be calculated directly from ray optics [20]:

$$F_{scat} = \frac{n_m P}{c} \left(1 + R \cos(2\theta_R) - \frac{T_F^2 (\cos(2\theta_R - 2\theta_T) + R \cos(2\theta_R))}{1 + R^2 + 2R \cos(2\theta_T)} \right)$$

$$F_{grad} = \frac{n_m P}{c} \left(R \sin(2\theta_R) - \frac{T_F^2 (\sin(2\theta_R - 2\theta_T) + R \cos(2\theta_R))}{1 + R^2 + 2R \cos(2\theta_T)} \right) \quad (20)$$

where R & T_F are the Fresnel coefficients, and θ_R and θ_T are the angles for reflection and transmission of the incident rays. Figure 3 schematically illustrates the origins of the axial and radial forces due to diffraction and how the component forces add together. For non-spherical and complex particles approximations can be computed [28]. The ray optics regime is increasingly accurate for dielectric particles of radius $r_p > \frac{5n_c \lambda}{\pi n_m}$, though for these larger

particles the radial trapping force diminishes. However, increasing the focal spot size to compensate would decrease the axial trapping force.

As mentioned earlier, trapping efficiency is highest for objects which are approximately a wavelength in size and therefore fall in the intermediate regime between the Rayleigh and ray optics regimes. Early approaches to analytically modeling this intermediate regime used a generalized Lorenz-Mie approach [29], though recently there has been progress through the extension of Rayleigh theory to larger particles [30]. Forces from both models compare well

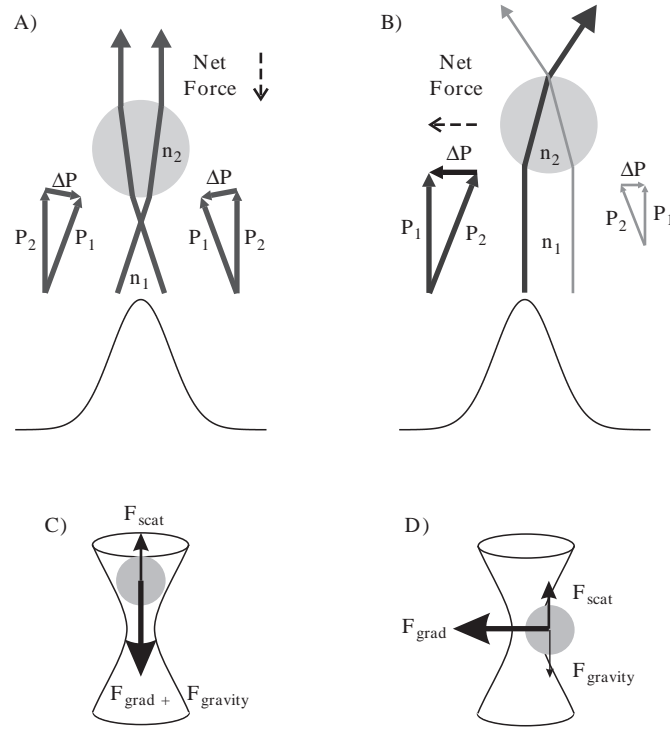


Figure 3. Schematic of the optical forces in the ray-optics regime. Summing the rays gives an (A) axial force due to vertical displacement from trap center; (B) radial force due to lateral displacement from trap center. Taking into account gravity and scattering, (C) the axial and (D) radial gradient force must be the dominant component to form an optical trap.

and have helped in trap calibration through the prediction of the far-field interference pattern resulting from a trapped object; potentially they will help in trap design and optimization.

These theoretical models generally assume a continuous, diffraction limited monochromatic beam focused by a high numerical aperture lens to trap a rigid dielectric sphere with a refractive index higher than the surrounding medium. All of these assumptions can be broken through choice of trap geometry, light source, and particle to be trapped. For the remainder of this section we will consider some of the trap designs, light sources, and particles which have been or can be used.

2.3 Types of Optical Traps

The standard optical trap uses a single high numerical aperture lens, typically a 100x objective with an NA of ~ 1.3 , to focus a near infrared laser to a diffraction limited spot and trap a polystyrene sphere approximately $1 \mu\text{m}$ in size. Imaging of the bead can be done through the same lens, opening one side of the sample, to manipulation or examination using another technique. Access to higher numerical apertures are limited by lens design and total internal reflection, while the spot size is limited by diffraction, and the maximum power is limited by damage thresholds. With the trap center at the maximum intensity, the maximum power is also limited by considerations of heating and damage to the trapped object and optics. Therefore, irrespective of design, it is unlikely that a conventional single beam optical trap will ever offer forces higher than a nanonewton because of these limitations.

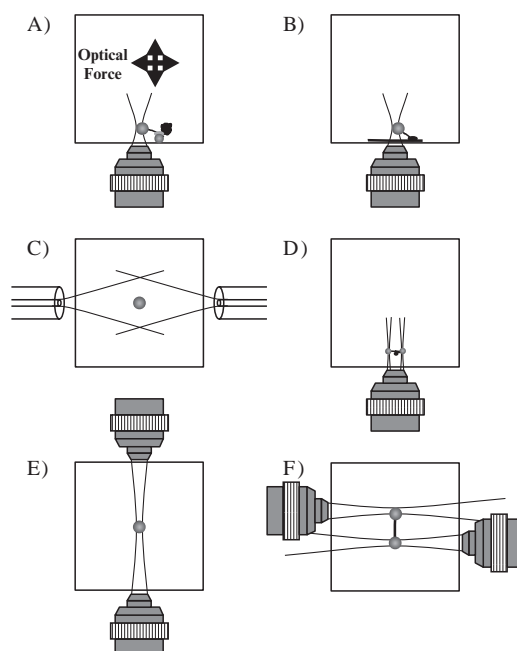


Figure 4. Optical trap designs: (A) immobilized enzyme with substrate tether; (B) immobilized substrate and tethered enzyme; (C) optical divergence trap using optical fibers; (D) multiple traps using the same objective; (E) dual objective trap with one or both objectives used to trap a single particle; (F) dual objectives in a horizontal configuration trapping independent particles.

A second major disadvantage of the standard design is the combined use of the objective for controlling force on the bead and imaging, which, while saving space, limits the direction in which forces can be applied and the range over which particles can be translated and imaged. Finally, light from a single beam can generally only trap a single bead, limiting the rate at which statistics can be collected and systems can be manipulated. Therefore, while the single beam design is an ideal and cost effective introduction to optical trapping, a number of other approaches have become increasingly popular. Figure 4 illustrates a number of common optical trap arrangements, and Figure 5 illustrates a number of common modifications to improve imaging or introduce other techniques.

2.3.1 Single Beam Optical Trap

The most common form of optical tweezers, the single beam optical trap, has matured into a turnkey package commercialized by a number of companies as a non-contact micro-manipulator for cell biologists. These systems provide a rapid and convenient method for nonspecialists to work with optical traps.

For manipulation there are two possibilities, movement of the trapping light or movement of the specimen. In general it is preferable to translate the specimen using a stage to avoid changing the optical beam path, even though optical deflection at high speeds can be more readily precise and reproducible.

A single beam optical trap typically has a radius of 250 nm and an intensity-dependent stiffness of 1–500 pN/μm, generating a maximum force in the range 0.2–100 pN. This enables single beads to be moved with velocities up to 1 mm/s, dependent on the trap stiffness. Using the methods described later, displacements down to 1 nm can be measured, corresponding to applied forces down to 100 aN [31].

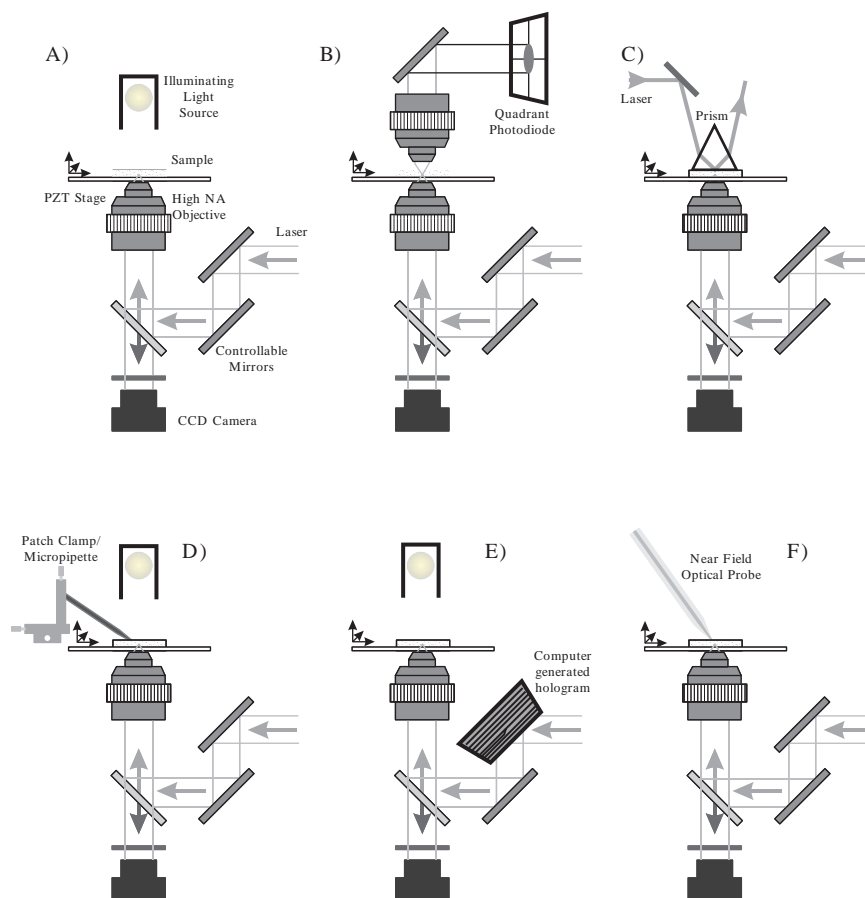


Figure 5. Common extensions to optical traps: (A) steerable mirrors to move trap position; (B) imaging of trapped particle onto a quadrant photodiode; (C) evanescent field excitation of trapped particles near a surface; (D) incorporation of a micropipette or patch-clamp; (E) dynamic trap configurations with a spatial light modulator; (F) excitation and imaging with a near-field optical probe. (*See Color Plates*)

Without feedback about the particle's position with respect to the trap center, single beam traps operate in the constant extension regime, providing a loading rate dependent on the speed at which the trap center is translated. A single beam trap also requires that the system under study be tethered to a solid surface to provide an anchor against which the force can be applied. Ideally, working in such close proximity to a surface is not desirable because it increases the risk of non-specific interactions and modifies parameters such as the drag coefficient because of the stationary boundary. For many applications, however, these limitations do not restrict the results which can be obtained; but to extend the range of operation, other approaches can have more favorable characteristics.

2.3.2 Multiple Beam Optical Traps

In the 1970s the second generation of stable optical traps used a second counter-propagating beam to counteract the scattering force from a single beam [2]; a modern incarnation is composed of two optical fiber tips a short distance apart and is known as an "optical stretcher" or optical fiber divergence trap [32]. Any trapped elastic object will be stretched along the axis between the fibers as a result of the asymmetry of the applied forces, and can result in deformation forces of 0.1–0.3 pN/mW for cells tens of microns in size. Trapping can be

achieved with relatively modest powers of tens of milliwatts and stretching achieved without the need for labeling, though large trapping volume and whole cell interactions are traded against trap strength, three-dimensional manipulation, addressing of submicron voxels, and position detection. In combination with microfluidics, an optical stretcher has the potential for high throughput screening [33], though the clinical impact remains to be seen. The use of multicore fibers, multiplexed fibers, and microfabricated optical waveguides should also provide increased flexibility for these traps. The extension of these fibers to subwavelength scales and the near field regime is discussed later in this section.

Closer in design to the single-beam setup, a second objective can be used to focus light counter-propagating and overlapping with the first objective. For identical objectives and illumination, the scattering forces will cancel, permitting the use of longer focal length objectives, and creating higher trapping forces than with the same intensity through a single objective. Alternatively, the objectives can be misaligned to create two independently controllable traps. The primary disadvantages are technical, in the alignment of the counter-propagating beams and loss of a large solid angle of access by the proximity of the second objective to the sample. The higher forces afforded by dual-beam optical tweezers have been used to over-stretch DNA [34, 35], though in general it is easier to scale the laser source to access higher trapping forces than to use a second objective.

For two or more independent traps using a single objective, a single beam can be easily split multiple times by a polarizing beam splitter to form two or more continuous and independent beams. This can be an attractive approach if a high power laser is available; however, independent manipulation of individual beams is non-trivial. An alternative to spatial separation of the beam is to “time-share” it between multiple points, by moving the light rapidly in the back focal plane of the objective using a deflector [36]. As long as the dwell time at each trap is sufficient to give a strong enough restoring force, the scanning rate is faster than the trap period and the beam can exactly repositioned; then multiple particles can be trapped at arbitrary locations in the same plane [37, 38]. Increasing the number of traps decreases the duty cycle for each trap, and to maintain the same trap stiffness the intensity must be increased. For a large number of traps, the fly time becomes a significant percentage of the duty cycle and wastage of the trapping power. The beam can be deflected at large angles using a pair of scanning galvanometer mirrors at rates of up to a kilohertz, but with limited reproducibility. Acousto-optic and electro-optic modulators, although more expensive and less efficient, can sweep smaller angles at up to megahertz frequencies with higher accuracy and stability. Limitations of this time domain modulation approach are that long term thermal stability is required for nanometer reproducibility, programming multiple trap trajectories can be complicated, and the high intensities required to maintain trap stiffness can lead to sample damage.

2.3.3 Holographic Optical Traps

One of the most significant advances in optical trap design recently has been the use of spatial light modulators (SLMs) to create dynamic, holographic traps [39]. The kinoforms required to manipulate the phase of an incident optical beam to create the traps can be computer generated and optimized from the inverse Fourier transform of the required image [40]. These kinoforms are then written to a spatial light modulator to imprint the new transverse phase mask, which results in the desired pattern of constructive and destructive interference in the focal plane of the objective [41]. Spatial light modulators working in reflection mode have higher efficiency compared to diffractive optics such as volume holograms because there are no diffracted orders; and they perform better than galvanometers in creating multiple traps, though currently they have a slow frame rate. Intrinsically they work in a narrow wavelength range and are limited to creating optical features defined by the degree of constructive and destructive interference available, with efficiency falling rapidly for features below half

a wavelength in size. The demand for projection systems has helped drive the development of SLMs which now have megapixel arrays with $>100:1$ contrast ratios and frame rates of up to 100 Hz [42], and these undoubtedly will improve.

Computing power limits trap geometries to predetermined configurations, though for many experiments this is not a significant limitation. Currently the spatial resolution of the available light modulators limits their performance and wider usage; though potentially they could allow parallel operation and faster data collection than that of the single trap geometries, but will never reach the update rates available from acousto-optic or electro-optic modulators. The future is bright for SLMs because the ability to manipulate multiple arbitrary particles using diverse transverse modes in three dimensions would be of benefit in many applications, such as intracellular manipulation and surgery, if the resolution, rate, and contrast can be improved.

2.3.4 Near-Field Optical Traps

The evanescent field created by total internal reflection at a surface [43] or at the metal-coated end of a fiber tapered to sub-wavelength dimensions [44] can be used to create a near field optical trap. These traps are generally only two-dimensional and have limited axial displacements, typically only a few tens of nanometers within 100 nm of a surface. However they can potentially describe sub-wavelength features, are not limited by the transmission of the surrounding medium, and do not require a high-NA objective. Using this approach, interference patterns have been used to manipulate and sort particles and cells on a surface [45]. However, the limitations of working near a surface and the difficulty of forming a three-dimensional trap have restricted the wider application of near-field techniques.

2.4 Types of Optical Beams

The spatial-temporal distribution of the electric field around the focal point of an optical trap is to a large extent controlled by the coherent properties of the light used. For example, a decrease in the spectral coherence of the light, corresponding to an increasing line width, will result in lower trapping efficiency due to increasing chromatic aberration. In the case of decreasing temporal coherence, pulsing of the light source will increase the peak intensity in the focal region while maintaining a substantially lower average power, which can be used to exploit nonlinear effects and minimize thermal effects. These are some of the many variables to manipulate in a laser light source relating to the spatial, temporal, and spectral coherence. One of the simplest examples is to switch the normal linear polarization used to circular polarization. As Beth observed in 1936, circularly polarized light carries angular momentum, which can generate torque on a birefringent particle [46]. However, it has been manipulation of the spatial coherence of the light which has had the most impact on optical trapping.

Spatial coherence, classically demonstrated in Young's double-slit experiment, is the ability for one spatial position of a wavefront to interfere with another. As with the other forms of coherence, the spatial coherence of a laser is determined by the type of optical cavity and gain medium used. Typically in optical tweezers, the laser cavity is a stable geometry, which produces the lowest order Hermite-Gaussian (TEM_{00}) transverse electromagnetic mode resulting in a diffraction-limited beam, giving the smallest waist and highest intensity at the focal point. However, there are a wide range of other coherent transverse modes, including higher-order Hermite-Gaussian modes, Laguerre-Gaussian modes, and Bessel modes.

2.4.1 Hermite Gaussian Beams

In rectangular coordinates, the individual solutions of the paraxial wave equation subject to boundary conditions, in the case of a laser boundaries defined by its mirrors, are described by Hermite-Gaussian modes. The spatial wavefront of the electric field of these transverse electromagnetic modes is described by two numbers corresponding to the number

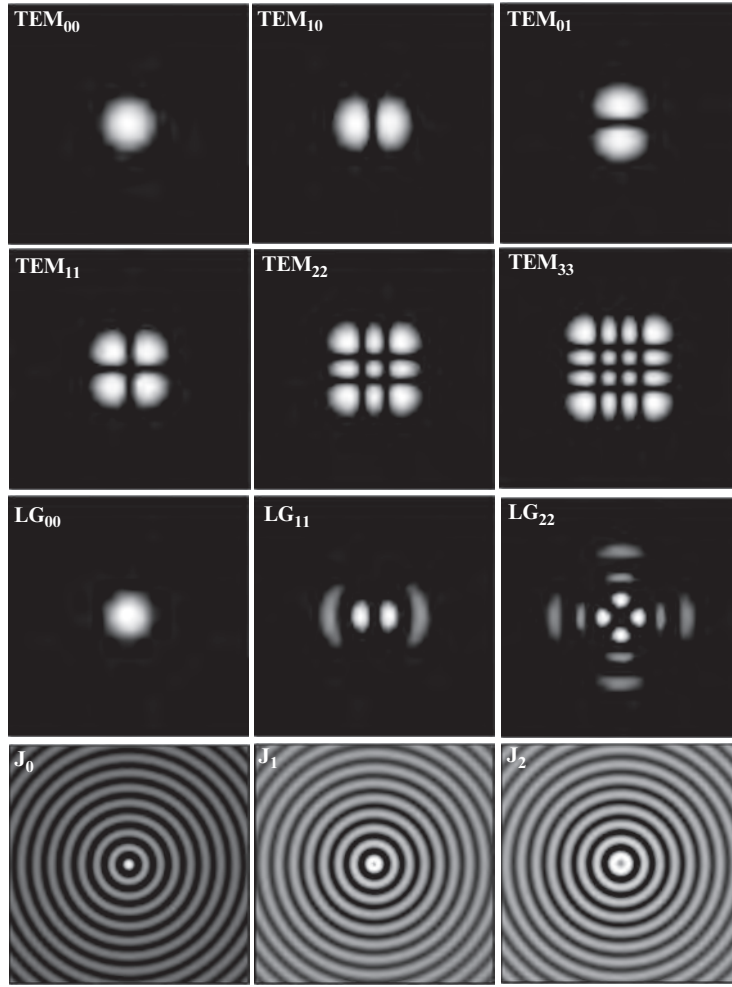


Figure 6. Intensity profiles for the Hermite-Gaussian ($TEM_{x,y}$), the Laguerre-Gaussian ($LG_{m,n}$), and the Bessel function (J_m) transverse electromagnetic modes.

of minima in each of two orthogonal directions to the direction of propagation. A (transverse electromagnetic) TEM_{00} beam is the lowest order Hermite-Gaussian mode with a single high-intensity lobe and the smallest divergence at the “diffraction limit,” while a TEM_{33} mode looks like a tic-tac-toe board and diverges significantly faster. A number of TEM modes are illustrated in Figure 6. The majority of optical traps use a diffraction limited beam in order to maximize intensity at the focal point of a single trap; however, it is also possible to trap using higher order modes from a laser [47], which offers a number of advantages including increased axial trapping force, as well as the ability to trap at both multiple maxima and local field minima. High order modes can be generated by tilting one mirror of the laser cavity or by using a computer generated hologram; however, to a large extent holographic optical traps have superseded static designs because they can be dynamically tuned and are not limited to only Hermite-Gaussian modes.

2.4.2 Laguerre-Gaussian Beams

For a circularly symmetric aperture, the paraxial wave equation can also be solved in polar coordinates, yielding Laguerre-Gaussian modes. The helical or corkscrew topology of

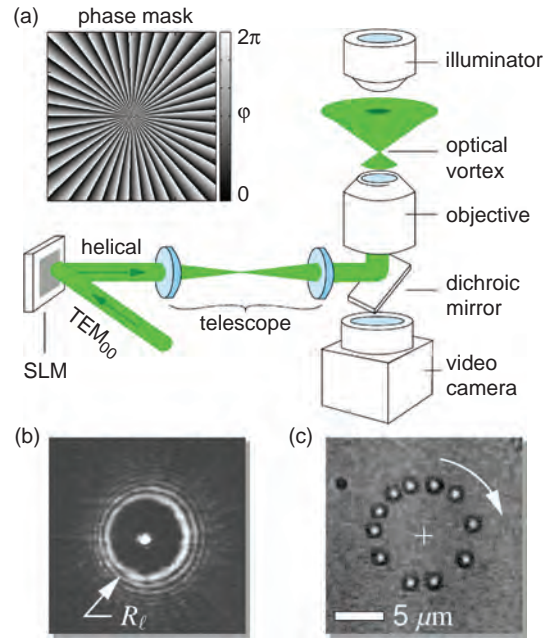


Figure 7. (A) Generation of a Laguerre-Gaussian mode from a Hermite-Gaussian TEM₀₀ beam using a computer generated phase mask on a spatial light modulator, (B) producing a radially symmetric intensity profile, (C) which can be used for the controlled rotation of trapped objects [Reprinted Figure with permission of Ref. 309 by the American Physical Society]. (See Color Plates)

the phase results in destructive interference along the optical axis, producing a ringed intensity structure, illustrated in Figure 7. For higher order modes the lack of axial light is helpful for trapping scattering, reflecting, or absorbing particles [48, 49], particles with a refractive index lower than the surrounding liquid [50], and large particles [51].

What distinguishes these optical beams is that they can impart orbital angular momentum [52], generating torque on a trapped dielectric particle. This radially induced motion has led to these traps being referred to as “optical vortices” [53] and “optical spanners” [54]. Interfering with these beams, for example, with a plane wave to create a multiple armed vortex, can produce many new and novel intensity profiles and consequently trap structures. By superimposing two Laguerre-Gaussian modes that are phased so that they destructively interfere, an optical bottle trap can be formed, where the dark central region is surrounded completely by regions of higher intensity, providing three-dimensional structure [55]. Controlled phase changes of any of these interference patterns will result in rotation of the high intensity regions and objects trapped there.

Rotational control of optically trapped particles has however not been exploited to the same extent as with magnetically trapped particles, in part because it is difficult to impart a defined number of turns to the particle. In most cases a constant torque is applied while the particle is illuminated by the trapping light, making precise control of, for example, the supercoiling of DNA difficult. There are many areas, such as in mixing within microfluidic channels, where this would not be a limitation.

2.4.3 Bessel Beams

Diffraction limits the range over which an optical intensity or spatial light profile can be maintained. Therefore it was a surprise when, less than twenty years ago, it was noted that Bessel functions provide wavelength scale transverse features which do not change along the

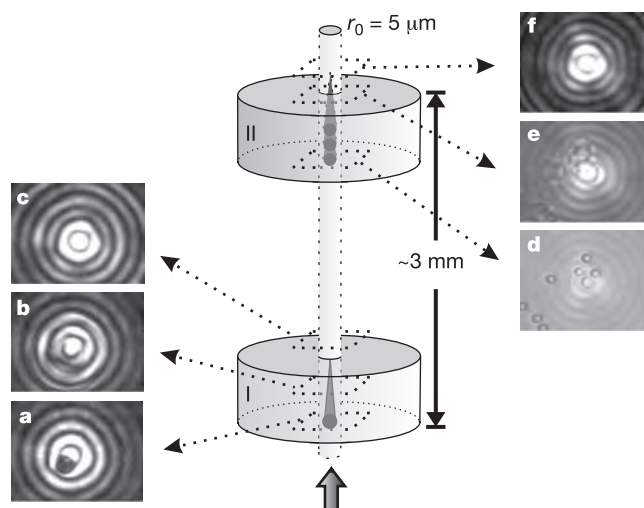


Figure 8. A diffractionless Bessel beam can be used to trap beads in two chambers separated by 3 mm [Reprinted from Ref. 58 by permission of Macmillan Publishers Ltd].

beam axis. Approximating with quasi-Bessel beams, this non-diffracting quality was used to optically manipulate particles in two separate chambers three millimeters apart in 2001 (Figure 8) [56]. Bessel beams do not form three-dimensional traps because there is no axial gradient, but they can trap both high and low refractive index particles simultaneously, as well as multiple particles along the optical axis, and do not require an objective [57]. The waveform is also to some extent self-healing and can be used to trap multiple particles along the axis of the beam, providing the ability to manipulate three-dimensional structures [58]. Again, the implications of using these beams for force spectroscopy of biological samples has not yet been fully explored, though potentially they open new regimes in which particles can be manipulated by light.

2.5 Types of Particles

Optical tweezers are capable of trapping particles composed of a wide range of materials, shapes, and sizes. The primary characteristics sought in a good particle have been low scatter and low absorption, with a surface which can be chemically modified. Traditionally micron-sized dielectric spheres have been trapped at the center of a diffraction limited beam; however, using higher order beams with a dark center, it is possible to trap reflecting and absorbing [49] particles as well as low index particles [50]. The size range of objects which can be trapped spans more than three orders of magnitude, from small metallic particles (5 nm) [26] to large ($>10\mu\text{m}$) beads [51] and cells. Core-shell or variable index particles, while potentially difficult to make, may offer a number of advantages both from a trapping and a functional perspective.

The composition of particles has not been as widely exploited, primarily limited to dielectrics and metals [59]. Some metals, for example gold, have a plasmon resonance in the visible spectrum and attractive thiol chemistry which can be exploited. In addition, particles containing light and environmentally sensitive compounds offer the possibility of local reporting and delivery—for example, using controlled hyperthermia to melt a low-melting point polymer containing a drug. Optical tweezing of carbon nanotubes has been demonstrated [60], reinvigorating the possibility of self-assembly and the use of carbon chemistry.

Nanocrystalline particles, in particular those containing rare earth ions, could be used both for enhancing the dielectric contrast, providing bright, narrowband, continuous fluorescence, and for providing localized heating. In addition, the quantization of the band gap and nonlinear phenomena of small particles have yet to be fully exploited in optical traps—for example, using two-photon excitation of resonances and stimulated emission/depletion to determine particle location within a trap.

This wide range of particles offers the possibility of optical tweezers as a unique and versatile tool for the three-dimensional, non-contact manipulation of microscopic objects. The ability to dynamically tune trap properties and the ease of integration with other techniques has led to them being applied to a wide range of problems in force spectroscopy. Before considering some of these applications, we will first consider the closely related field of magnetic tweezers.

3 Magnetic Tweezers

3.1 Introduction

The use of magnetic particles for biophysical measurements dates back more than fifty years. In 1950 Crick and Hughes [1] used magnetic particles for a study of the viscoelastic properties of the cytoplasm, pioneering the field of magnetic twisting cytometry and cell rheology. Microrheology investigations have since been carried out on a wide range of biopolymer networks, cells, and tissue types to provide insight into cytoskeletal and extracellular organization and the dynamics of biochemical processes [61]. The use of magnetic particles to investigate the force spectroscopy of single biomolecules has been a natural extension of these techniques, offering an alternative to optical tweezers.

Commercially, magnetic particles have come to prominence as an effective, generic technique for separating and purifying target cells and biomolecules [62]. By labeling superparamagnetic particles with chemical or biological species that selectively bind a target analyte in a reversible reaction, repeated separation and concentration can be achieved using a simple, inexpensive magnet. Superparamagnetic particles are used because their response is several orders of magnitude higher than diamagnetic or paramagnetic particles, but they have no remnant field, so they can easily be dispersed. There are also fewer restrictions on their size, transparency, and composition because these properties are not critical to their operation. So this enables size to be optimized, whether high force or large surface area is required, while their response to a magnetic field can be tuned by composition without influencing the optical properties or biochemical tagging.

This flexibility in particle size and functionality has led to magnetic particles being used *in vivo*—for example, as MRI contrast enhancement agents with submillimeter voxel resolution [63,64], and in hyperthermia treatments [65] for targeted energy delivery. These characteristics have not been widely exploited to date in force spectroscopy studies; however, directed energy transfer and localized magnetic resonance imaging using magnetic cantilevers may prove useful in single-molecule studies. One of the other unique characteristics of magnetic beads is that they can exert an attractive or repulsive force on nearby objects. The decay in the magnetic field from the surface of a small particle is very localized, decreasing as a function of the particle's radius, making it ideal for studying nanometer phenomena in a small volume. The resulting high field gradient and hence force can also be used to self-assemble beads into lattices [66], providing sensitive detection and characterization of biomolecules as well as a platform for directed cell growth.

The force due to a magnetic field is analogous to the optical gradient force, with a potential energy due to the response of the particle to an external field. A magnetic field is distinct from an optical field, however, in that a maximum cannot be created in free space

and cannot be manipulated other than by shaping the magnetic elements. This results in the ability to create a uniform force over a large area, enabling many systems to be probed at once, resulting in fast data collection [67]. The orientation of the field can also be manipulated independent of the gradient, permitting controlled rotation, attractive for studying phenomena such as supercoiling. However, these properties also make it difficult to form a stable trap without feedback, to manipulate single particles, and to change dynamically the trap characteristics.

“Magnetic tweezers” is an umbrella term for a number of different techniques, only a subset of which form a stable three-dimensional trap, while others rely on the fact that one end of the system under study is tethered to a surface. A stable trap can be formed either using feedback or by balancing the magnetic force with another force—for example, fluid flow. However, for the majority of experiments described in the second half of this chapter, a simple magnetic gradient is used to create a constant force experiment.

This section will mirror the discussion of optical tweezers, with an introduction to the origin of the magnetic force, followed by a discussion of magnetic tweezer design and the particles which can be manipulated. From a practical perspective, the decoupling of the imaging path from the force generation axis is advantageous for both tweezer design and particle selection. Magnetic fields also have the advantage that they are less likely to damage sensitive biological specimens. However, these advantages also place more reliance on the addition and placement of a responsive bead, through which a force can be applied and the results studied.

3.2 Theory of Magnetic Force

Magnetism plays an important role in many aspects of our daily life, from computer storage to electric motors. Qualitatively, materials can be described by their response to an applied field, as illustrated in Figure 9. If a material is placed in a magnetic field of strength H , the individual atomic magnetic moments in the material contribute to its overall magnetic induction response:

$$B = \mu_0(H + M) \quad (21)$$

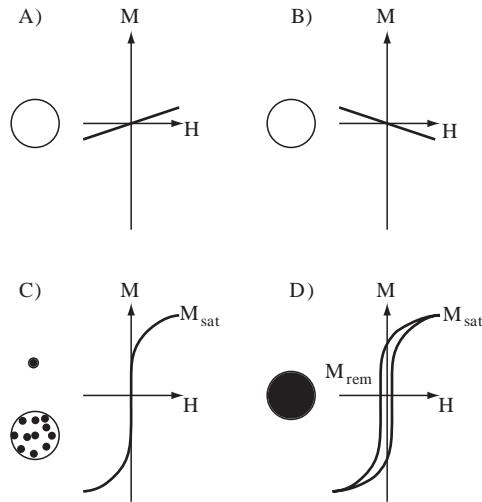


Figure 9. Magnetic response of different materials: (A) paramagnetic, (B) diamagnetic, (C) superparamagnetic, and (D) ferromagnetic.

where B is the magnetic induction, H is the external magnetic field strength, M is the magnetization and μ_0 is the permeability of free space. The magnetization of the material can be classified in terms of its magnetic susceptibility:

$$M = \chi_m H \quad (22)$$

where χ_m is the dimensionless magnetic susceptibility. In paramagnetic materials, χ_m is small and positive ($\chi_m = 10^{-6} - 10^{-1}$), locally strengthening the magnetic field by weakly aligning the magnetic dipoles present in the material with the external field. In contrast, the local field is weakened by the presence of a diamagnetic material, with the magnetic dipoles aligning anti-parallel to the external field ($\chi_m = -10^{-6} - -10^{-3}$). If the magnetic susceptibility is nonlinear and the dipoles can spontaneously align without an applied field, then the material is ferromagnetic ($\chi_m = 10^1 - 10^3$). Superparamagnetism occurs when a ferromagnetic particle is smaller than the domain size required for spontaneous alignment (typically 10–100 nm), because thermal fluctuations cause moment reversals on time scales much shorter than the experimental time frame, resulting in a net zero field in the absence of an external field. As the strength of an external magnetic field increases, the number of aligned dipoles within a superparamagnetic material increases up to some saturation level, giving a characteristic sigmoidal response without the hysteresis of ferromagnetism.

Analogous to optical tweezers, the potential of a single magnetic dipole m in a constant magnetic field B is given by:

$$U_m = -m \cdot B \quad (23)$$

A gradient in the magnetic field will result in a potential gradient and a force on the magnetic dipole:

$$F_m = (m \cdot \nabla) B \quad (24)$$

Thus, because the magnetic dipoles in a particle respond to an external field, the force on the particle is dependent on the number and type of dipoles present. The force on a superparamagnetic bead in a magnetic field gradient is:

$$F_m = M(B) \nabla B \quad (25)$$

where $M(B) = \frac{m}{V}$ is the external field dependent volumetric magnetization of the particle, V is the volume of the bead, and ∇B is the magnetic gradient. In a liquid medium, the susceptibility contrast of the particle relative to the water can be expressed as $\Delta\chi = \chi_{\text{particle}} - \chi_{\text{liquid}}$, which in turn gives $M = \Delta\chi H$, and the force can be expressed as:

$$F_m = \frac{V \Delta\chi}{\mu_0} (B \cdot \nabla) B \quad (26)$$

If there are no currents or time-varying fields, then we can apply Maxwell's equation, $\nabla \times B = 0$ to the above expression:

$$F_m = V \Delta\chi \nabla \left(\frac{B^2}{2\mu_0} \right) = V \Delta\chi \nabla \left(\frac{1}{2} B \cdot H \right) \quad (27)$$

where the force is related to the differential of the magnetostatic field energy density. From this equation a particle can be a high field seeker or a low field seeker, dependent on the liquid in which it is immersed, and the force is dependent on the volume magnetization. It is no surprise that equation 27 is comparable to equation 12, which described the gradient force for an electrostatic potential, because they are intertwined in electromagnetic theory.

In both cases the force is dependent on the particle volume (assuming homogeneity), the field gradient, and the contrast of the particle against the surrounding medium—the only differences really arising from the different ways in which the fields are generated.

A magnetic field falls as the inverse of the distance from the surface of a large bar magnet with corrections for the size of the magnet, the rate increasing as the magnet becomes more point-like. For the large magnet, the magnetic field gradient and the force decrease are the inverse square of the distance. One complexity of magnetic tweezers arises because the magnetization of a superparamagnetic particle is dependent on the applied field below saturation. This field and hence position dependence makes extrapolation for calibration and dynamic control of particles non-trivial for three-dimensional traps.

As with optical tweezers, magnetic particles are typically observed with a microscope, to maximize temporal, spatial, and spectral resolution. Alternatively, giant magnetoresistive sensors [68] (illustrated in Figure 10) and miniaturized Hall sensors [69] can also be used

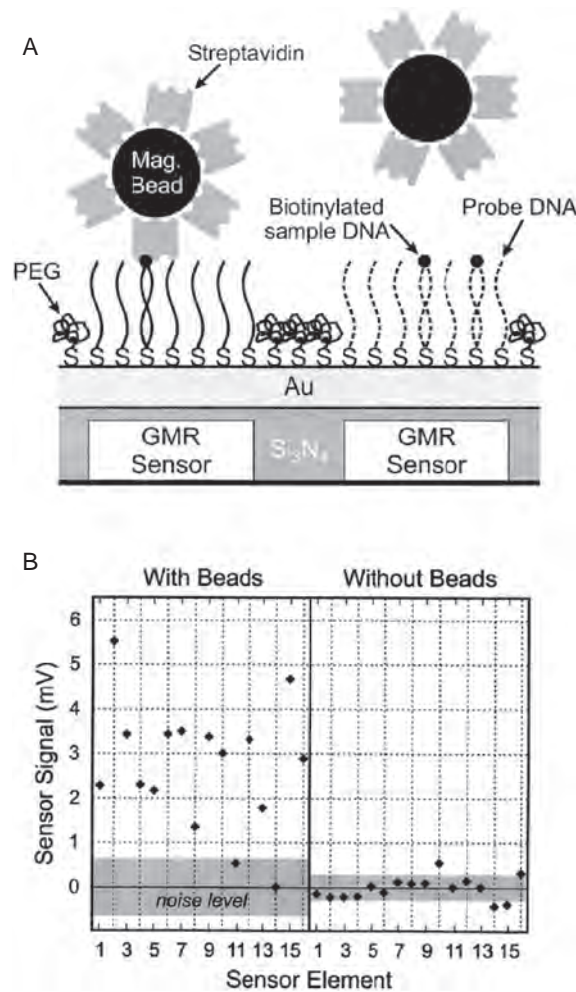


Figure 10. A) Schematic of the bead-array counter (BARC). Thiolated DNA probes specifically bind to complementary DNA strands on magnetic beads, the presence of which can be detected by a GMR sensor. The impact of non-specific binding can be minimized by applying a magnetic force before detection to remove excess beads. B) Binding events can be detected by electrical readout with the signal intensity dependent on the number and distance of the beads from the detector [reprinted from Ref. 310 by permission of Elsevier]

to detect the presence and orientation of beads above their surface, introducing the potential for low cost detection of multiple samples. Magnetic fields already have applications in micro-electromechanical systems and biomedical applications [70], for pumping, detection, filtering, and concentrating; and along with the diverse spectrum on functionalized superparamagnetic particles available, they will play an increasingly significant role in the concept of lab-on-a-chip analysis [71].

3.2.1 Torque

In addition to creating a force, a magnetic field can also be used to exert a torque on a particle. When the magnetic moment of a particle and the external field are not parallel, then a torque

$$\Gamma_m = \mathbf{M} \times \mathbf{B} = mB \sin(\vartheta) \quad (28)$$

is exerted on the particle, where θ is the angle between the external field and the magnetic moment. Torques of several hundred pN nm can be generated by rotating the magnetic field, either by physically rotating the magnet or using phased electromagnets. In contrast to the constant torque induced by circularly polarized light in optical tweezers, magnetic tweezers induce constant twist.

In practice, for free particles at low frequencies and low viscosities, the torque results in rotation of the particle. There is a drag torque on the particle [72]

$$\Gamma_{drag} = 8\pi\eta r^3 \omega \quad (29)$$

and the rotation frequency, ω , can be evaluated under dynamical equilibrium with rates of tens of hertz easily achieved for micron-sized particles.

For particles attached to a tether, the torsion stored in the tether is [73]

$$\Gamma_{tether} = \frac{C\Omega}{L} \quad (30)$$

where C is the torsional modulus, Ω is the twist angle, and L is the contour length of the tether. If the tether is twisted sufficiently far it will undergo a buckling transition [74] and plectonemes will be formed, with the transition characterized by:

$$\Gamma_b = \sqrt{2L_p k_B T F} \quad (31)$$

where L_p is the persistence length of the tether and F is the applied linear force.

The winding and unwinding of DNA has been explored extensively using magnetic tweezers [75], though the torsional properties of few other biopolymers have been characterized. This is surprising, because twist can induce conformational changes in the substrate to mimic protein activity. For example, structural proteins rely on torsion as part of their rigidity, and diverse rotational molecular motors create torque during their operation, providing a wealth of studies uniquely suited to magnetic tweezers.

3.3 Types of Magnetic Tweezers

There is greater flexibility in the construction of magnetic tweezers than in that of optical tweezers because the microscope objective is no longer required as part of the force transducer setup. Figure 11 illustrates some of the designs used in magnetic tweezer experiments. Instead, a magnetic element must be placed in close physical proximity to the beads

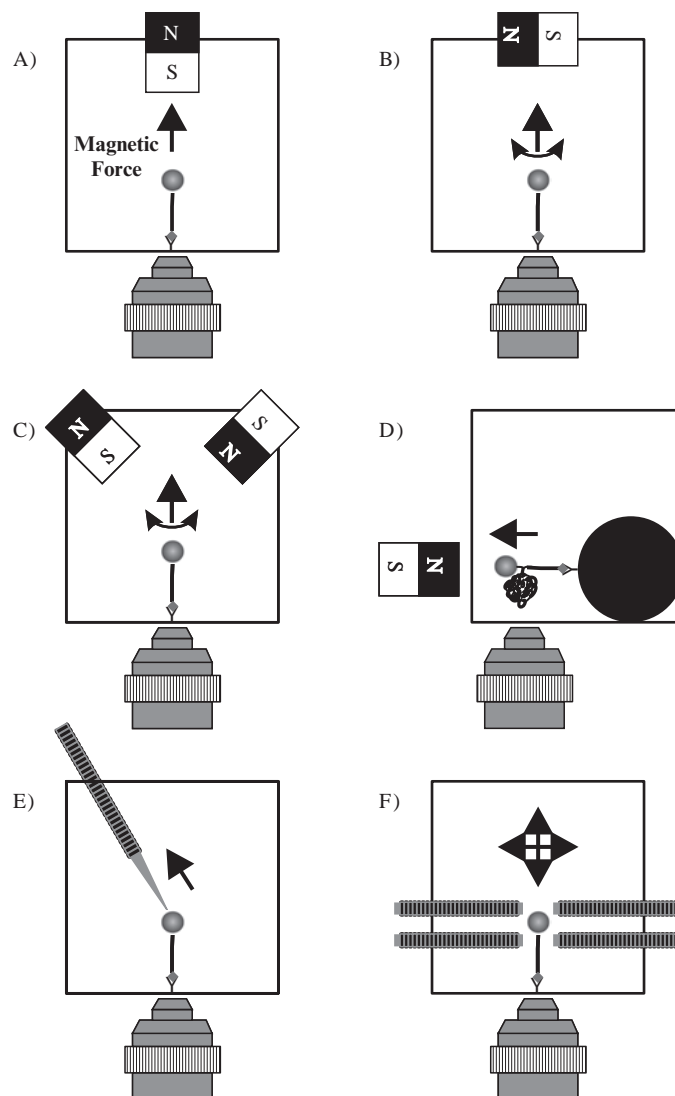


Figure 11. Magnetic tweezer configurations. (A) simple attractive force in parallel to optical axis; (B) magnetic poles perpendicular to optical axis; (C) multiple poles symmetric around optical axis providing rotation; (D) attractive force perpendicular to optical; (E) electromagnet needle; (F) multi-pole electromagnets with feedback providing a 3D magnetic trap.

in order to generate a force, introducing different constraints. The magnetic elements can be either permanent magnets, where their distance to the beads is adjusted to generate different forces; or electromagnets, where the current is adjusted to change to force. The size of the magnet also needs to be considered, with small magnets producing steeper gradients, but which need to be placed closer to the beads; and larger magnets producing shallower gradients, but which can be used at a greater distance and over a larger field. As a rule of thumb, to generate a high force on a superparamagnetic bead, the distance from a permanent magnet must be less than the width of the magnet for sufficient field gradient and magnitude.

A practical consideration is the orientation of the magnetic field and the gradient with respect to the optical axis of the microscope. If the gradient is perpendicular to the optical axis, then a single magnet can be used in the plane of the sample to give a simple attractive force, and displacements can be observed in one direction of the focal plane while the force is calibrated in the other. If the gradient is parallel to the optical axis, then displacements will result in defocusing of the beads, while motion in the focal plane will be due to Brownian motion. Rotation of the beads can also be more easily detected with the gradient parallel to the optical axis, though this requires a ring magnet to avoid blocking the optical illumination path. In addition, for rotation of a tethered particle, the field gradient should be parallel to the optical axis and rotation axis to generate torque or rotation at constant force in the image plane. For self-assembly of beads at a surface, the direction of the field should be perpendicular to the surface and usually parallel with the optical axis, while the generation of columns within the field of view is best done with the field direction perpendicular to the axis.

In order to create a three-dimensional magnetic trap, as opposed to an attractive gradient, at least six magnetic elements are required, as well as a feedback system to control the force toward each. Practically, this can only be achieved using electromagnets and optical feedback and by compromising the force available from a single magnet. Multipole arrangements do however have a number of other advantages, including rotation using phased currents [76], and integration with other approaches such as microfluidics.

As with optical tweezers, magnetic tweezers have been combined with a number of other techniques, most notably glass microneedles [77]. Surprisingly, the widespread use of overlapping optical and magnetic traps in cold atom research has yet to carry through to single-molecule studies. Superparamagnetic beads are also useful as a calibration tool—for example, to calibrate the stiffness of a microneedle or other cantilever by applying a known force.

A number of general papers on the construction and characterization of magnetic tweezers have been published [78, 79], discussing the advantages, disadvantages, and trade-offs involved. Here we will briefly consider the choice of magnet system and magnetic particles to highlight some of the possible approaches.

3.3.1 *Permanent Magnetic Tweezers*

A wide range of permanent magnets are available, which can be used to create strong magnetic field gradients, most notably those made from neodymium, iron, and boron (NIB, $\text{Nd}_2\text{Fe}_{14}\text{B}$). These rare earth magnets have the highest residual magnetic flux density ($>12,000\text{ G}$) of any permanent magnet and can be machined or sintered into any required shape. A single magnet can be used to create an attractive force of up to 200 pN with a resolution as low as 10 fN [80]. NIB magnets have the highest quality factor for a magnet, implying that a required magnetic flux can be obtained with a smaller volume of the material. The other permanent magnetic materials with attractive properties for magnetic tweezers are the alnico family of alloys of aluminum, nickel, and cobalt with iron. Some of these alloys have higher remnant fields than NIB magnets and a coercive field of less than 0.1 T , which may be beneficial for bi-stable switching.

The high surface flux densities of permanent magnets can be exploited by placing small, soft ferromagnetic structures in close proximity to enhance the local field. For example, adding a stainless steel needle to the surface of a NIB magnet can enhance the force to more than 1 nN in the region of the needle tip [81]. An alternative approach is to use the gradient created perpendicular and close to the corners of two opposing magnets in close proximity to each other. In this way, the field gradient again can be enhanced above 1 T/mm and used to levitate and trap paramagnetic particles against gravity or flow [82]. Emptying the trap can be done by increasing fluid flow to exceed the upward repulsive force of the magnets, illustrating one way in which the fixed force limitation of permanent magnets can be overcome.

3.3.2 Electromagnet Tweezers

Electromagnets have the benefit of precise control of the magnetic field and the ability to easily switch the magnitude and direction of the field as well as the number of poles energized. Permanent magnets need to be mechanically moved in order to exert temporal control of the field at a point in space, making rapid changes and vibration-free rotation difficult to achieve. However, heat dissipation, magnetic hysteresis, and lower field magnitudes have hampered the more widespread use of electromagnets.

The magnetic field gradient available at the end of an electromagnet's core is primarily determined by its composition and geometry. Ideally, the core is composed of a soft ferromagnetic material with no residual magnetic field and a large magnetic susceptibility, to maximize the magnetic flux density for a given solenoid current. If the field generated by the solenoid can be made sufficiently high, then iron is the ideal choice as the core material, with a saturation field of up to 2 T, though with a low relative permeability ($\mu_r = 7,000$), it is less attractive at low fields. Mu-metal and the other nickel iron alloys of the same family are better choices for a low field solenoid, with a higher permeability ($\mu_r = 300,000$) but a lower saturation field (0.77 T). High purity, single crystal, orientated iron would outperform both these materials, but would not be stable or practical to use in these experiments. Independent of the choice of material, the core piece is at risk of heating and expanding and may have a limited frequency response, which needs to be considered in any design.

The gradient can also be enhanced by shaping the core into a point with a small radius of curvature, most commonly a needle shape. Simple, single core devices used to create an attractive gradient can be mechanically engineered to create forces up to 1 nN [77], and more recently up to 50 nN [83], by electropolishing. However, it should be noted that there is a trade-off between the enhancement gained from shaping the core and the decrease in spatial extent of the desirable gradient. Working with a radius of curvature less than 100 μm requires consideration of access and thermal expansion, but can also be advantageous in being able to address a single bead in a field and manipulating it. Although not extensively employed to date, these devices have the potential to create local repetitive stain by low frequency amplitude modulation and to create localized heating around single beads by high frequency modulation.

Microfabricated magnetic traps, for integration with microfluidics, have also been constructed [84]. This initial demonstration showed that in an external magnetic field, $1 \times 4 \mu\text{m}$ magnetic pads could trap individual beads from up to 5 μm away with a force of up to 100 pN.

Microfabricated designs allow complex material and topological constructions such as the use of field enhancing soft ferromagnetic structures to generate gradients up to 2 T/cm from micron-sized wires [85]. The flexibility in creating arbitrary trap shapes and distributions on a surface using many different material characteristics, for example in the form of electrically-driven magnetic spin valves capturing different magnetically labeled species, is potentially very powerful but has not been fully realized. The difficulty in implementing a strong, fully three-dimensional magnetic trap is an unresolved problem, and perhaps best addressed using microfabrication [86] if there is sufficient need.

Macroscopic three-dimensional magnetic traps, or true magnetic tweezers, have been built using Hall probes to measure the magnetic fields of an octopole arrangement of electromagnets symmetric around the trap center [87]. With a distance of 7.5 mm between opposing 5.5 mm diameter poles, the maximum force on a 2.8 μm diameter beads was 1 pN for a surface field of 0.05 T and could generate a torque of 0.01 pNm. Haber and Wirtz reported a two-coil electromagnet configuration with water cooling perpendicular to the optical axis, which produced a gradient of up to 1 T/cm for 1.5 cm separation and forces up to 10 pN [78]. More recently a hexapole arrangement above the sample plane produced a trap with a stiffness of

0.1 pN/ μm and a maximum force of 5 pN, moving beads at up to 10 $\mu\text{m/s}$ [79]. To ensure linear feedback in these magnetic traps, a square root function needs to be applied to the error signal, but is complicated by the field-dependent magnetization of the bead below saturation, making displacement and force correlation difficult.

Dynamic electromagnetic traps have a number of advantages over optical tweezers, including a much larger trapping volume preventing loss of the trapped particle because of transients, and a greater range of motion, not limited by the working distance of a high numerical aperture lens; though these are gained at the expense of complexity in operation and lower trapping forces.

3.3.3 Other Magnetic Force Devices

A range of other devices which utilize a magnetic force have been developed to manipulate magnetic particles for biological applications. As mentioned at the beginning of this section, active microrheology, manipulating small magnetic particles to measure viscoelastic response [88], has been used extensively to characterize the viscoelastic properties of living fibroblast [89], macrophage [90], and endothelial [91] cells. A range of magnetic separators have also been developed, including the use of packed columns, multipole arrangements [92], and fluid flow fractionation [93]. Methods for preparing [94], tracking, and selecting [95] immunomagnetic particles and their targets have complemented these separators. Red blood cells, cancer cells [96], bacteria [97], and Golgi vesicles [98] have also been tracked and separated using magnetic particles. The negative susceptibility contrast, between diamagnetic particles and a liquid with a positive susceptibility, has also been exploited to form a weak-field-seeking trap [99]. A stable trap for particles can also be formed by exploiting gravity [100], using a ferrofluid [101], or using additional DC/AC electric fields [102], illustrating the wide range of possible magnetic trap setups.

3.4 Types of Magnetic Particles

The choice of particle composition and size is determined by the application and the force required. Primarily, superparamagnetic particles, and to a lesser extent ferrofluids, are used because of their large positive susceptibilities and zero residual fields. Large ($> 500\text{ nm}$) particles can easily be tracked with light microscopy or magnetic resonance imaging and used to create multiple linkages or for distributing the force over a larger area. Smaller particles ($< 50\text{ nm}$) can address single molecules in vivo and be fluorescently labeled or enhanced optically for imaging with optical or electron microscopy.

The force generated by a particle increases with iron content, but does not necessarily correspond directly to particle volume because of density constraints to keep the particles superparamagnetic and the randomness involved in their synthesis. The magnetic moment and frequency-dependent susceptibility of beads can be measured using a SQUID magnetometer/susceptometer, and the magnetic field using a Hall probe. From these measurements a sample often shows significant variation because of the random number of iron oxide grains which are incorporated in each bead. Ferrofluids, composed of single iron oxide particles, have a more uniform distribution, though they are difficult to manipulate at the single-molecule level.

The success of functionalizing superparamagnetic beads for separation has stymied development of other composite magnetic particles. Although depositing a shell of magnetic material onto a polystyrene or quantum dot core would produce a more uniform sample of beads, most metals are too refractive or toxic to be presented on the surface. Pure cobalt nanoparticles have been made; and the pigments used in magnetic recording devices such as nanoCAP and barium ferrite have attractive properties, though it remains to be seen whether they can have a biological impact. Gold or silver coatings may be an alternative to embedding in a polymer matrix and can improve optical detection of small particles; however alloy

formation may be a problem. Organic magnetic particles can be embedded in micelles and vesicles [103], and iron-sequestering proteins like ferritin have the potential to be engineered into molecular magnets [104]; though neither has been developed to the stage of being used by the wider community. The all-round flexibility of superparamagnetic polystyrene beads is difficult to beat, though changing applications may drive the marketplace in new directions utilizing these alternative technologies.

3.4.1 Superparamagnetic Particles

A large number of companies (e.g., Dynal Inc., Bangs Laboratories Inc., Duke Scientific, Miltenyi Biotec) offer 0.1–100 μm diameter superparamagnetic beads with a wide range of chemically or biologically labeled surfaces that have traditionally been used for magnetic separation. These beads are typically composed of ~10–20 nm iron oxide (both magnetite and maghemite) particles embedded in a porous polymer matrix. Typically, an outer polystyrene shell isolates the iron and provides a surface for adsorption of antibodies or other reactive groups.

The magnetic properties of the 2.8 μm diameter M280 beads from Dynal Inc. were analyzed [87] and found to have an average momentum per bead of $1.42 \times 10^{-13} \text{ Am}^2$ at a saturation field of $1.4 \times 10^4 \text{ A/m}$ with no detection of hysteresis. The standard deviation in the magnetization of a sample of particles was 40%, because of a variation in the number of Fe_2O_3 grains within the polystyrene matrix of individual beads. The average grain diameter was estimated to be 15 nm, half of the single-domain size limit, with a bead containing ~200,000 grains with a mean separation of 50 nm. Without an applied force, the density of the beads is 1.3 g/cm^3 , and the mass is 15 pg, resulting in a downward force of 34 fN in solution due to gravity. The magnetic susceptibility of the beads quoted by the manufacturer was 0.1, but was found to be closer to 1 at low field strengths. Thus a saturated M280 bead in a 1 T/cm field gradient would experience a force of approximately 14 pN, the threshold for pulling apart the two strands of dsDNA at room temperature. Using a larger 4.5 μm diameter bead, forces of up to 200 pN are possible with a single NIB magnet.

3.4.2 Ferrofluids

Ferrofluids, discovered and popularized by NASA in the 1960s, are typically composed of ~10 nm magnetite ferromagnetic particles in a nonpolar medium containing a surfactant. The liquid is superparamagnetic with low hysteresis, while the small size of the particles and the surfactant helps prevent agglomeration. Ferrofluids have found many diverse applications in damping loudspeaker cones and in forming liquid seals in hard discs, and are also starting to find applications in biotechnology, in particular as a drug carrier and hyperthermia target. Related to ferrofluids are magnetorheological fluids, which contain micron-sized superparamagnetic particles able to overcome Brownian fluctuations and form chains in the presence of a magnetic field, causing an increase in viscosity. This has led to their use in brakes, actuators, and valves.

Although both types of liquids and magnetostrictive solids have been used for generating force in the macroscopic [105] and microscopic [106] world, they have not been used in force spectroscopy at the nanoscale; in part because the particles are difficult to functionalize, to image with white light, and to keep dispersed in physiological buffers.

While magnetic tweezers are attractive because the force transducer is decoupled from the imaging path, and optical tweezers are attractive because it is significantly easier to dynamically trap and manipulate an object in three dimensions, both techniques are excellent for non-contact force spectroscopy in the range 0.1–200 pN, with a high degree of flexibility and adaptability. The similarity in these techniques often permits the same imaging and tracking techniques to be used for resolving displacements and forces. These common construction and characterization techniques will be discussed in the next section.

4 Construction and Characterization of an Optical/Magnetic Trap

4.1 Building a Non-Contact Micromanipulator

A basic optical or magnetic tweezers system can be constructed from scratch or added to a good research microscope for less than \$10,000. A number of practical primers have been published on how optical [107, 108, 109, 110] and magnetic [78, 79] systems can be constructed, aligned, and characterized. The major limitations of basic systems are in the strength and stability of the trap produced, which places constraints on force calibration and analysis. With increased funds, a more powerful laser with improved intensity and pointing stability, an objective with a higher numerical aperture and chromatic correction in the infrared, an anti-vibration table, a piezoelectric stage, and better image capture and processing software could provide single-molecule tracking and manipulation with nanometer and millisecond accuracy.

In addition to the generic components of an optical or magnetic trap considered in this section, the properties of a trap are also determined by the size, shape, and composition of the particles to be trapped and the surrounding medium. For most single-molecule experiments the medium is generally a physiological buffer, such as phosphate buffer saline (PBS) or TRIS-EDTA buffer, containing 100 mM Na⁺ and possibly other ions, with the optical properties of a dilute salt solution. The particles to be manipulated are mostly if not all polystyrene, around a micron in size and best imaged with a broadband light source.

4.1.1 Trap Configuration

The spatial arrangement of the imaging path and force transducer is determined by the requirements of the experiments to be carried out and the limitations of the equipment available. Inverted microscope designs are the most prevalent for measuring biological forces because gravity ensures surface wetness, and that particles will congregate on the surface, liquids can be easily exchanged, and the use of oil or water immersion lenses will be straightforward. In the case of optical traps, the imaging light path is most commonly co-linear with the laser light used to form the trap, maintaining constant illumination if the trap, stage, or objective is translated. For attractive magnetic tweezers, the magnetic field gradient is typically perpendicular to the optical axis.

Arrangements in other orientations offer different trade-offs. For example, side-imaging into a flow cell reduces background at the expense of increased difficulty in finding particles to trap and in maintaining objective immersion. An upright design can permit direct liquid immersion, reducing the impact of the coverslip, but can be limited by fast evaporation of the small liquid volume. While commercial microscopes can readily and quickly be modified to include optical or magnetic tweezers, home-built systems typically offer the highest degree of stability and flexibility.

4.1.2 Objective

For imaging there is a trade-off to be considered between the magnification of the objective, and the working distance. An increase in magnification, generally associated with an increase in numerical aperture, decreases the working distance and field of view, but also increases the axial trapping force for optical tweezers. The primary constraint is that the working distance must exceed the thickness of the coverslip used as a substrate to hold the liquid sample. A coverslip is typically 50–200 μm thick, so in order to have a sufficient gradient to prevent axial escape, the trap is typically limited to within 100 μm of a surface for conventional high magnification ($> 60\times$) objectives ($\text{NA} > 1.2$) and a diffraction limited beam in an inverted design. Higher numerical apertures are possible, though they do not offer improvement for regular white light imaging, instead being used for total internal reflection studies. Long working distance,

high magnification objectives are also available, though this involves sacrificing numerical aperture, which may not be critical if photon counts are not limited.

4.1.3 Light Source

The choice of laser for an optical trap determines and is determined by a number of considerations including the required force and trap stiffness, sample, imaging, and trap geometry, incorporation of dynamic elements, and the wavelengths of least perturbation to the objects to be trapped. Cost plays a significant role, with additional money often correlating with improved pointing and amplitude stability, mode quality, reduced thermal drift, and increased wavelength tunability. As a rule of thumb, the maximum trapping force increases 0.1 pN/mW of light in a diffraction limited beam delivered to the specimen plane with a high NA objective, and scales to a maximum incident optical power of ~2 W before damage becomes an issue [21].

Expanding the input laser beam to overfill the back aperture of the objective can help increase the ratio of axial to radial force at the expense of overall intensity [20]. For high power lasers, this aperturing can result in heating and thermal fluctuations of the objective mount.

The majority of modern optical traps employ a near-infrared laser with a wavelength of 700–1100 nm. This range generally corresponds to the lowest risk of optical damage for biological specimens, though even within this range there is a large variability; for example, there is a small absorption peak around 980 nm. The growth in optical data storage and communications has provided a wealth of inexpensive and high power visible and infrared lasers, though they often do not have a single transverse mode in both orthogonal directions and have a high degree of astigmatism. Diode-pumped solid state lasers, such as Nd:YAG operating at 1064 nm and its siblings, are the workhorse of many single-molecule experiments because of their high output powers and higher quality optical outputs. At the most expensive end of the laser spectrum, Ti:sapphire lasers provide the most versatile light source, with wavelength tunability and a range of modes of operation, including mode-locking, dual wavelength operation, and synchronization with other light sources, useful for spectroscopic techniques such as Raman scattering.

For particle imaging in both optical and magnetic traps, a high brightness source is desirable, whether in bright-field, fluorescence, or image contrast mode. Halogen and mercury lamps are staples of microscope design, though as discussed later, light emitting diodes and lasers operating below and above threshold offer advantages for high resolution position detection. For complementary confocal and two-photon imaging, a separate imaging path is required, complicating, though not necessarily limiting, trap design.

4.1.4 Piezoelectric Stage

One of the most significant advances in optical trap design in the past decade has been the development of three-dimensional piezoelectric stages with capacitive feedback. These stages provide subnanometer position control over distances up to two hundred microns and submicro-radian straightness during translation, for driving frequencies up to 1 kHz. The introduction of capacitive sensing and feedback has dramatically improved the positioning and reproducibility of piezoelectric stages, eliminating the traditional problems of hysteresis and drift. The accuracy and speed of these stages can be incorporated as part of a force-clamp loop for optical tweezers, to maintain centered quadrant photodiode tracking or adding dithering to improve resolution.

4.1.5 Imaging Systems

High resolution imaging systems are required to track submicron displacements and quantify piconewton forces. Modern, digital, silicon-based charge-coupled devices (CCD cameras), which can provide megapixel images at tens of hertz and are sensitive to light from

400 nm to 1000 nm, are the workhorses of video microscopy. Cooled, slow-scan CCDs push the quantum detection efficiency to more than 80%, allowing the spatial motion of single fluorophores to be observed [111]. Alternatively, by binning and defining regions of interest, the capture rate can increase to more than 100 Hz. Using CMOS chips, the partial frame rates can be pushed up to and beyond 100 kHz, though it is worth remembering that there is an increased requirement for light intensity and image storage working at these speeds. At the fastest end, streak cameras can be used to measure picosecond events. Flash photography, using the light source rather than the camera frame rate, can also be used to study dynamics, for example, fluorescence recovery after photobleaching (FRAP).

Temporal statistics of low brightness sources can be collected at up to gigahertz frequencies using sensitive photomultiplier tubes and photodiodes, though these systems do not provide spatial information. Linear photodiode arrays and quadrant photodetectors offer the compromise of limited spatial information while maintaining high sensitivity with fast readout rates.

Simple spectral information can be collected using RGB filters like those found in color CCD cameras. For more detailed spectral information, light from the sample can be diffracted using a grating and imaged onto a 1D array of photodiodes, or the grating can be tuned and a single photodiode used. Single shot spectra can be obtained from Fourier transform spectrometers.

Moving away from silicon and detection of visible light, and still at the exploratory stage, high-resolution and fast imaging can be pushed into the mid-infrared using InGaAs and InSb detector arrays and photodiodes. The development of optics in these regions still has to catch up with the quality available in the visible range; however, there are a wide range of phenomena which can be detected and manipulated with micron to millimeter wavelengths, which may drive development.

4.2 Particle Tracking

Force cannot be measured directly in either an optical or magnetic tweezer setup; instead it is inferred either from displacement measurements from the center of a three-dimensional trap, or from the extension of a calibrated elastic molecule tethered to a surface.

Measuring these displacements and extensions for accurate calibration requires nanometer resolution. Bright-field imaging of the tagged polystyrene particles is the most common method, tracking the center of mass using digital image processing of a CCD image. Sufficient light needs to be refracted or scattered from these particles to form an image, limiting their size to >100 nm. In this size range a functionalized bead can tag one or more of the desired, smaller biomolecules and can potentially constrain the biomolecule's activity through steric effects.

Tagging the biomolecules of interest with fluorescence markers, such as dyes, quantum dots, or fluorescent proteins can remove size limitations and permit fluorescence microscopy. However, each of these techniques has a disadvantage in terms of duration, consistency, or intensity of the fluorescence it produces; and none of them contribute towards exerting a force. Their dipole nature does however make them extremely versatile, providing sensitivity to their environment—for example, in ion concentration sensing or distance to other fluorophores through resonant energy transfer. The small size of these fluorophores is also advantageous in intracellular and diffusion studies or in advanced microscopy techniques such as two-photon, confocal, or stimulated emission/depletion microscopy. The development of fluorescent proteins and their incorporation as gene reporters has provided a powerful, quantifiable technique for *in vivo* gene expression and will aid in understanding the effects of force on cells. To date there are no magnetic equivalents to the diversity of optical reporters and probes, though undoubtedly they will be developed.

For any optical tracking system, the exposure time should be sufficiently short compared to the correlated motion time $\left(\tau_0 = \frac{\gamma}{\kappa}\right)$ of the particle to prevent blurring, while the time between acquisitions should be longer than the correlation time to prevent oversampling and correlated measurements. As the spring constant decreases, corresponding to a weaker optical trap or longer tether, the desirable sampling rate can fall to a few hertz, limiting detection of fast phenomena. Both conditions can be fulfilled by video and photodiode imaging systems, and the merits of both are now considered.

4.2.1 Video Tracking Systems

Video-based tracking systems can make use of an existing CCD camera attached to a microscope port to give ~ 5 nm accuracy, at the video acquisition rate (< 120 Hz). For the highest accuracy, the pixel scaling needs to be calibrated against a length standard, the image needs to be digitally processed, and a centroid-finding algorithm needs to be used [112]. Typically these algorithms are implemented in offline image processing packages such as IDL and ImageJ and require large quantities of data storage or in real time using LabView or custom-written applications.

Calibration of both the camera and the stage can be carried out by imaging first a length standard and then translating a fixed bead with the stage in each of the three orthogonal directions. Axial calibration can be obtained by measuring the diffraction rings visible around a fixed particle on a surface as a function of distance above the surface, again leading to a resolution of approximately 10 nm.

Real time tracking of multiple objects in three dimensions using a single camera has been demonstrated with ~ 10 nm resolution [79] and is indispensable for long-term studies of complicated dynamics. While stiff traps cannot be optimally imaged by CCD cameras because their correlated motion time is < 10 ms, video tracking is suitable for tracking multiple particles, tracking events involving discontinuous or large displacements, offline analysis, absolute displacements, and as a reference for other detection schemes.

4.2.2 Position-Sensitive Detectors

Quadrant detectors have proved to be a convenient, sensitive, high speed method for tracking single particles. The basic idea is to use the magnification of the microscope to image a micron-sized symmetric particle onto a millimeter-sized four-quadrant photodetector. The symmetric image of the particle will create equal voltages in each of the four quadrants. If the particle moves down, then more light will fall on the upper quadrants, which can be observed by summing and subtracting the relevant quadrants. Similarly, movement can be detected in the other three directions of the focal plane. If the particle moves out of focus, this can also be detected by a change in the overall light level falling on all four quadrants. In this way, nanometer movements in the position can be observed.

Although the response of a quadrant photodiode is linear for small displacements, it quickly becomes nonlinear within the range of typical usage; and therefore for accurate measurements the voltage outputs of the quadrants need to be calibrated with known displacements using a piezoelectric stage. Typically this is done by raster scanning a fixed bead with the stage and averaging a number of runs or beads to create a calibration map for the detector, taking care to calibrate axial positions, in particular the offset of an optical trap from the focus.

Axial displacements are more challenging to measure with the same resolution, because microscopes are designed to image in two dimensions and calibration of focal shifts is non-trivial. A number of methods have been described for determining focal shifts, including the intensity of scattered light [113], two-photon fluorescence [114], and evanescent wave excitation of fluorescence [115]. Perhaps the simplest approaches, however, are to sum the intensities of the four quadrants [116], or use a linear photodiode array or CCD to analyze the diffraction rings [79].

The laser light used to form the trap can also be used to find the axial position of a trapped particle by one of two methods. Using polarization interferometry [117], displacement of the particle results in a phase delay in one of the arms of a Wollaston-based interferometer, though in practice this technique is limited to one dimension and small displacements. Alternatively, by looking at the interference between the forward and unscattered trapping laser light at a phase conjugate of the back focal plane, particle displacements can be tracked in both lateral directions [118]. Often it is more practical to implement a second laser for detection, separated in wavelength from the trapping laser, particularly in characterizing multiple or moving traps [119].

The major distinctions between video-based tracking and the use of quadrant detectors are that video tracking provides a measure of absolute displacement at low frequencies for multiple particles, while quadrant detectors are more sensitive and have a higher bandwidth for measuring relative displacements of a single particle in a stiff trap.

4.2.3 Limitations to Tracking Resolution

The sensitivity of all detection systems is ultimately limited by noise. Noise sources include light source fluctuations, mechanical vibrations, electronic noise, stray light, and thermal drift. Acoustic and mechanical noise can be minimized by working in a quiet laboratory with the microscope system mounted on a vibration-isolation table and enclosing the observation area to reduce air currents, acoustic noise, and stray light. Thermal drift is more problematic for long-term observation, and requires isolation of heat sources and stable air conditioning.

Light source fluctuations, both from power and pointing variations, can register as anomalous particle movements, but even with a continuous light level, shot noise will limit detection accuracy at short time scales and low light levels. For example, with arc-lamp illumination, photon shot noise can introduce an uncertainty of several nanometers for a one micron bead imaged on a quadrant detector with a bandwidth of 15 kHz [108].

Although significantly spatially and spectrally brighter, laser illumination of particles is hampered by coherent artifacts, such as speckle, and anomalous correlated Brownian motion. Therefore, for passive position tracking, a laser diode operating just below threshold is used to provide a high brightness, incoherent illumination source [120], with a high light level which can be more precisely filtered than an arc lamp, while avoiding the coherent artifacts of a laser operating above threshold.

Low light levels increase the susceptibility of the detection system to electronic dark noise and Johnson noise. With careful circuit design, suitable choice of bandwidth, and isolation, these noise sources can be minimized. Random noise can be filtered digitally using arbitrary cut-off frequency filtering, local averaging, wavelet-based filtering, and nonlinear filters to remove noise outside the frequency range of interest and excessive noise within the range of interest. What remains then as the major source of noise is Brownian motion in determining a particle's position in a well configured tweezers, which is both an advantage and a disadvantage.

4.2.4 Photo-Induced Damage

Often the desired light level and high signal-to-noise is sacrificed in order to minimize photo-induced damage. Biological specimens absorb the most weakly in the wavelength region 800–1000 nm, and many optical tweezers operate in this range to minimize photodamage and optocution [121]. However, even in this range, photodamage of cells [122, 123] and proteins [124] occurs within a few minutes and has been linked to modification of ion channels [125]. As a rule of thumb, cells directly illuminated with 1064 nm light will experience a temperature rise of $\sim 1^\circ\text{C}/100\text{mW}$ [126], which can be calibrated more accurately using a low melting temperature wax [108]. This limits the power of direct illumination to a few

hundred milliwatts in the infrared [127] and less than 100mW in the visible [5] before cell damage or death occurs.

Photodamage and heating can be minimized by working at a wavelength with the lowest absorption and scattering and by minimizing impurities and imperfections. An alternative approach is to use hollow beam traps and low field seeking particles; in this case the trapping region is dark, minimizing heating because inelastic scattering is minimized. As with almost any disadvantage, heating can also be employed productively, for example in locally melting DNA base-pairs, if required.

Particle tracking in itself is useful for understanding intracellular transport, such as the movement of vesicles and membrane diffusion, in terms of velocity and correlation; and group behavior, such as the swarming of *E. coli* and cellular taxis. For single-molecule force spectroscopy, the primary goal is to understand biological interactions in terms of their energy landscape, which can be measured by position and force. In optical and magnetic tweezers there is no direct readout of force and it must be inferred from motion. Thus particle tracking is central to both position and force measurement and is a critical part of any optical or magnetic tweezer setup.

4.3 Force Calibration

Force information can be extracted from a system using two methods. Either the force can be kept constant (“force clamp”) and the extension measured, or a constant rate of extension applied (“position clamp”) and the displacement measured. The first approach describes the basic operation of a simple attractive gradient magnetic tweezers, while the latter describes optical tweezers. Using feedback in either setup can reverse which variable is clamped.

In a position clamp experiment, the rate at which the trap is displaced provides control of the loading rate. As might be expected, loading rate can have a profound effect on the viscoelastic behavior of biomolecules. This has caused some concern over the range of loading rates which should be studied and has opened up a distinction between dynamic and static force spectroscopy [128], in particular for studies using atomic force microscopy. Static force spectroscopy experiments, using a constant force, tend to operate closer to equilibrium. The energy landscape of a complex can start to be established by measuring dissociation under different load conditions and extrapolating to zero load, and though this plot may not be linear, often the thermal dissociation rates for a bound system can be determined [129].

A special case of passive particle tracking exists when the force is always adjusted to be zero by centering the trap continuously to the particle’s position. In contrast, negative feedback can be used to enhance trap stiffness and change the time constants involved in maintaining a trapped particle’s position (“position” clamp), to the point of underdamping. The peak-to-peak thermally driven movements of a trapped bead are approximately 20–60 nm, but with negative PID feedback the position can be clamped to approximately 1 nm [130], with the required trap displacements characteristic of the forces acting on the bead.

A number of in-depth reviews for calibrating the force in optical [21, 118, 131] and magnetic [79] tweezers have been published. Currently theoretical analysis is limited to calibrating only spherical particles, though of course irregular particles can be trapped and tracked and the force estimated. There are three commonly used methods for measuring the force in both optical and magnetic tweezers which will now be briefly considered.

4.3.1 Equipartition Theorem Analysis

Analysis of the motion of particles underlies the field of microrheology. Laser tracking microrheology is an extension of this concept, using low intensity light to illuminate and measure particle motion without exerting a significant force.

Unbound particles in a medium and in thermal equilibrium with their surroundings will undergo Brownian motion, executing a random walk as they are bombarded by the molecules

making up the medium, if they are unhindered. In an optical or magnetic trap, the bead will also undergo Brownian motion, but there is a restoring force created by the potential of the field. Thus, because we know the energy associated with Brownian motion and the motion of the particles can be tracked, the gradient of the potential can be estimated. The restoring force experienced by a trapped bead can be modeled in one dimension by Hooke's law:

$$F_x = -\kappa(x - x_0) \quad (32)$$

where κ is the spring constant, or trap stiffness. In a well-aligned optical tweezers system, the trap is radially symmetric, with the axial spring constant typically an order of magnitude lower than the radial constant. The stiffness of a three-dimensional magnetic trap is dependent on the PID of the active feedback loop, but is approximately the same order of magnitude.

Decoupling the three orthogonal directions so they can be considered independently and using the equipartition theorem, the time-averaged potential energy in the x-dimension associated with the trap is:

$$\langle U(x) \rangle = \frac{1}{2} \kappa \langle (x - x_0)^2 \rangle = \frac{1}{2} k_B T \quad (33)$$

where x_0 is the equilibrium position, k_B is Boltzmann's constant, and T is the temperature. Thus the random distribution of the particle's position within the parabolic trap is a Gaussian:

$$p(x) = e^{-\frac{U(x)}{k_B T}} \quad (34)$$

and the trap stiffness can be found by dividing the thermal energy by the mean square of the displacement. Furthermore, the validity of the Hookean spring approximation can be tested by plotting the probability density function and comparing it to a Boltzmann distribution.

For optical traps the radial displacements are easier to calibrate than axial excursions; though with more complicated image analysis and comparison to immobilized particles, the same resolution can be achieved axially. By observing the bead position at video rate and using image analysis software, the trap stiffness can be calibrated in several seconds.

In the case of magnetic particles attached to a tether, the force can be found by considering the assembly as a pendulum. Using the equipartition theorem, the transverse fluctuations of the bead relative to a tether of length L are related to the force on the bead:

$$F_x = \frac{k_B T L}{\langle (x - x_0)^2 \rangle} \quad (35)$$

This calibration technique assumes there is no directed motion, for example due to gravity, underlying the Brownian fluctuations, or any inhibition due to a tether. Any issue will become apparent by deviations in the Gaussian distribution, and this can be used as a helpful diagnostic. Measurements can be made relatively quickly using this method, with typical errors in the range of 1–5%, although calibration in all three dimensions requires more effort.

4.3.2 Viscosity Calibration

A number of methods for calibrating the force on a particle use knowledge of the viscosity of the surrounding medium. The viscous drag force on small spheres in the laminar flow regime (Reynolds number for the beads is $\sim 10^{-5}$) can be found from the Stokes formula:

$$F_{vd} = 6\pi\eta r_p v = \gamma v \quad (36)$$

where η is the fluid viscosity, γ is the drag coefficient, r_p is the bead radius, and v is the relative velocity of the fluid to the bead. Thus by measuring the terminal velocity of spheres of known size in a liquid with a known viscosity, the force on the free bead can be measured.

Beads can be dispersed in a range of liquids with known viscosities, from water (1 cps) to silicone fluids (> 12500 cps) and tracked using video microscopy to determine both their size and velocities. Increasing the liquid viscosity decreases the terminal velocity, keeping speeds within the range which can be measured in the field of view of the camera, typically < 0.1 mm/s, and allows higher forces to be measured. Near a surface or other solid object, the drag is modified, but can be estimated by Fraxen's law [21].

Equating the drag and magnetic forces for a magnetic particle far from a surface gives the velocity of the particle relative to the gradient of the magnetic field [132]:

$$v = \frac{\Delta\chi r_p^2}{9\mu_0\eta} \nabla(B^2) = \frac{\xi}{\mu_0} \nabla(B^2) \quad (37)$$

where ξ is the magnetophoretic mobility of the particle, and a measure of how easy it is to manipulate. It is worth noting that as the force on a particle increases as the volume, the viscous drag force increases only linearly with the radius (inertial drag is dependent on the cross-section), making magnetic separation with large beads extremely fast and efficient in low viscosity liquids like water.

Many variations of the viscous drag method exist: particles can be dragged through the liquid at a known rate by displacing a trap repetitively at a known velocity [20]; the liquid can be displaced past a stationary trap by moving the stage or flowing the surrounding medium; or for magnetic particles, their terminal velocity at varying distances from the magnet can be measured. When the measurement is carried out with low particle density, in an isodense liquid in a region far from a surface, the estimation of the force can be better than 5%.

One advantage of these methods is that a trap can be characterized in all three dimensions both by a static force and by rapid displacement right to the edges of the trapping volume, where the response is no longer linear. In addition, measurement of the escape force provides a crude measurement of the trap depth to complement knowledge of its shape. The disadvantages include the need for a calibrated translation stage, imaging system, and surrounding liquid, long calibration and analysis times, as well as uncertainty in the drag coefficient because of irregularly shaped particles or the presence of nearby surfaces. This last issue can however also be used to provide height calibration to within ± 50 nm [133].

4.3.3 Power Spectrum Analysis

The previous methods have required a calibrated position detector to determine trap stiffness; however, it is possible to also calculate the spring constant of a trap using relative position measurements and knowledge of the particle's viscous drag coefficient. The motion of a trapped particle of mass m , undergoing Brownian motion by a random, fluctuating force F_L , can be described by Langevin's stochastic differential equation:

$$\frac{d^2x}{dt^2} + \frac{\gamma}{m} \frac{dx}{dt} + \frac{\kappa}{m} x = \frac{F_L}{m} \quad (38)$$

where x is the displacement of the particle from its equilibrium position, $\gamma = 6\pi\eta r_p$ is the Stoke's viscous drag coefficient, and κ is the trap stiffness in the x -direction. Assuming the

system is overdamped and the inertial term can be omitted (low Reynold's number approximation), the two-sided power spectrum of the particle is of the Lorentzian form:

$$|S(v)| = \frac{|F_L|}{\pi^2 \gamma (f_c^2 + v^2)} \quad (39)$$

where f_c is the 3dB corner frequency:

$$f_c = \frac{\kappa}{2\pi\gamma} \quad (40)$$

If no distinction is made between positive and negative fluctuations, then the one-sided power spectrum or power spectral density (PSD) is:

$$PSD = 2|S(v)|^2 \quad (41)$$

A typical power spectrum of a trapped bead is illustrated in Figure 12. Physically, this is the power spectrum corresponding to a bead attached to a spring immersed in a viscous liquid and excited by a thermal white noise source. At frequencies below the corner frequency, the power spectrum is that of a Hookean spring of stiffness κ , whereas at higher frequencies the inverse square frequency dependence is characteristic of the viscosity.

Experimentally the spring constant is found from a Lorentzian fit of the displacement power spectrum measured by a quadrant photodiode. The bandwidth of the detector system should be tens of kilohertz, substantially above the corner frequency (~ 1 kHz for a $0.8 \mu\text{m}$ -diameter sphere in water) in order to resolve the rollover in the power spectrum and to avoid problems with phase lag.

The accuracy of the stiffness measurement, $\sqrt{1/f_c T_m}$, increases inversely with the number of samples. For stiff traps, the corner frequency and hence the sampling rate are in

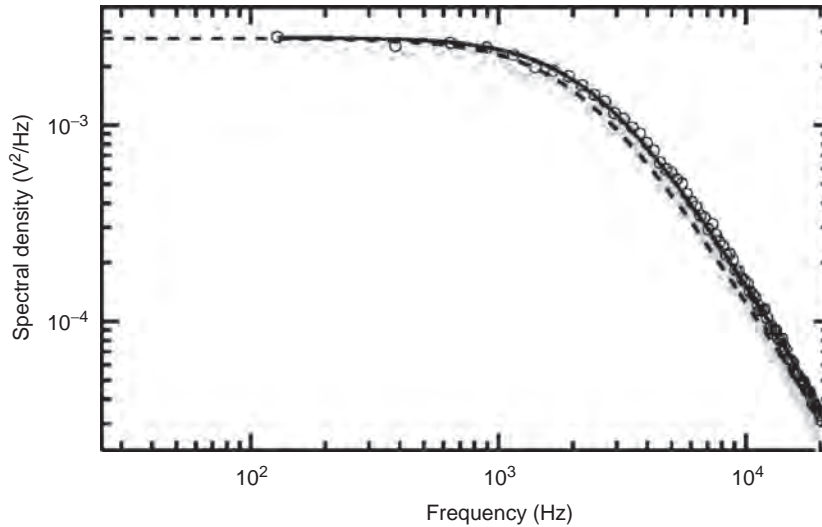


Figure 12. Power spectrum of an optically trapped $0.5 \mu\text{m}$ diameter polystyrene bead trapped $1.2 \mu\text{m}$ above a surface. The result is fitted with a corrected Lorentzian with a roll-off frequency of 2.43 kHz and a stiffness of 0.08 pN/nm [reprinted, with permission, from Ref. 110. Copyright 2004 American Institute of Physics].

the kilohertz range. To obtain good statistics and an accuracy of <5% only a few seconds of sampling is required. For weak traps (<1 pN/μm) the acquisition rate is much slower and requires many minutes before the error is reduced below 10%. The power spectrum is also a powerful diagnostic, with a non-Lorentzian spectrum or peaks in the spectrum characteristic of noise and misalignment.

Also, an analysis of the autocorrelation function, the inverse Fourier transform of the power spectral density, can be used to calculate the trap stiffness. The correlation function can be rapidly calculated as:

$$\langle x(t)x(t+\tau) \rangle = \frac{k_b T}{\kappa} e^{-\frac{\tau}{\tau_0}} \quad (42)$$

where τ_0 is the trap correlation period defined in equation 15. Again, analysis of the correlation function can be used to diagnose problems and to determine sampling and exposure periods in order to avoid oversampling and blurring.

These high sampling rate methods are well suited to characterizing the force on strongly trapped particles, which can be carried out within a few seconds to an arbitrary degree of accuracy. The disadvantages are that the viscosity needs to be well calibrated and only stiff three-dimensional traps can be calibrated in this way.

The construction and characterization of optical and magnetic tweezers is well documented and straightforward, forming part of many undergraduate laboratory classes. The complexity of the setup can be scaled to meet resources and requirements, but even with the most basic systems there is a degree of wonder in the ability to manipulate micron-sized particles with light alone and in measuring distances and forces many orders of magnitude below those of our normal day-to-day experiences. The application of these techniques to measure and study the influence of force in biological systems is perhaps the most fascinating aspect and has acted as a draw for people from all backgrounds.

5 Applications of Optical and Magnetic Tweezers in Force Spectroscopy

5.1 Introduction

Force spectroscopy is a powerful, dynamic technique for measuring the mechanical properties and interactions of individual molecules. Many cell functions have a positional dependence and mechanical component, whether through bond rearrangement or movement. Requirements for access in biological systems make probing and manipulating without a sub-micron, non-contact technique difficult, especially for intracellular work, the topic of the second half of this section and an ideal regime for force spectroscopy with optical and magnetic tweezers.

At the beginning of this chapter the forces and energies involved in determining the structure and interactions of biomolecules were discussed, with an emphasis on low energy processes. In the first half of this section, focusing on in vitro single-molecule experiments, the diversity of molecules which have been studied will help illustrate that most biological interactions and structures are determined by these relatively low energies.

For a physics audience it should be noted that the force spectroscopy of biomolecules is rarely simple to predict, analyze, or carry out. Biological adhesion is not typically mediated by a single, high-affinity bond, but by many weak ones, some of which may be nonspecific, adding diversity and also frustrating analysis, often requiring prescreening of results in order to make sure the system being observed is the one expected. Contamination

and environmental changes are a constant battle in working with a single molecule for long periods of time, as well as coping with transients and drift. That said, nanometer and piconewton scale phenomena such as the stepwise motion of single kinesin motors [117] and the discrete rotation of ATP synthase [134] have been observed, highlighting the power and excitement associated with force spectroscopy carried out by optical and magnetic tweezers.

5.2 Inter- and Intra-Molecular Force Spectroscopy

Not surprisingly, experiments have focused on commonly available, simple systems, in particular biopolymers and proteins which can be purified easily and have defined properties which have been characterized by other techniques. Over the past decade, optical and magnetic tweezers have most often been applied to measuring the tensile strength of ligand/receptor interactions, measuring the elastic properties of biopolymers, following and manipulating the activity of enzymatic proteins and investigating molecular motors. Each of these areas will now be considered briefly.

5.2.1 Ligand/Receptor Interactions

Interactions between biomolecules are mediated by a complex array of intermolecular and intersurface forces, which form a number of specific, noncovalent bonds. For example, antibodies binding to cell surface antigens form a complex with specific lock-and-key interactions which can include steric, electrostatic, and van der Waals forces. These forces are governed by the chemical and physical structure of the molecules, both of which are influenced by their environment. The net interaction profile of all the specific and nonspecific forces provides a complex energy potential landscape. To infer the strength and nature of these interactions, equilibrium and kinetic measurements of bulk samples can be carried out by flow shearing, circular dichroism spectroscopy, surface plasmon resonance, calorimetry, titration, and a wealth of binding assays.

Ligands, referring to extracellular substances, bind to membrane-bound receptors, providing recognition of intracellular signaling molecules and metabolites. Ligands are small molecules, such as vitamins and hormones, which can be isolated relatively easily from the environment. Complete transmembrane receptor proteins can be difficult to isolate, though complete peripheral and anchored receptors or functional subunits can be isolated, providing source material for *in vitro* analysis. In the second half of this section, experiments to measure receptor binding *in vivo* will also be discussed.

The primary goals of single-molecule studies of ligand/receptor systems are to confirm the binding affinity or dissociation constant measured by ensemble methods, to determine whether loading rate significantly alters dissociation rate, and to determine the number of binding sites and presence of intermediate states.

The dissociation rate of a simple bond under an applied force F is related to the zero force rate by

$$k_{off}(F) = k_{off}(0)e^{\frac{Fx}{k_B T}} \quad (43)$$

with x interpreted to be the width of the potential bound state and $k_{off}(0)$ the thermal dissociation rate. Thus the dissociation rate is expected to increase exponentially with force, under the Bell model. Single-molecule measurements can be related to ensemble measurements by considering the unbinding rate as a function of applied force [135]

$$F = \frac{k_B T}{x} \ln \left(\frac{r_l}{k_{off}(0) \frac{k_B T}{x}} \right) \quad (44)$$

where r_l is the loading rate. From a plot of F vs. $\ln(r_l)$, the zero force rate and width of the potential can be found from the sloped and intercept, respectively. Multiple transition states can be modeled in a similar way by evaluating the association and dissociation rates between each state.

The majority of ligand/receptor measurements have been carried out with atomic force microscopes because of the large range in loading rate. For example, the interacting force between two adhesion proteoglycan carbohydrates, used as an adhesion system in aggregating cells, was found to be 40 ± 15 pN using an AFM [136]. Optical tweezer systems, with their higher force sensitivity, could potentially provide a more accurate description, though they do not have the same loading rate range.

5.2.1.1 Biotin/(Strept)avidin: There has been a lot of experimental effort, particularly with AFMs, in studying the interaction of the small ligand biotin, with a pair of closely related receptor proteins, avidin and streptavidin. Avidin, derived from egg white, and biotin, or vitamin H, are widely used as a model system because of their unusually high affinity (the thermal dissociation rate of biotin/strepavidin is $2.4 \times 10^{-6} \text{ s}^{-1}$ [137]) and ready availability, as well as extensive structural and thermodynamic data.

The binding free energy of biotin is 22 kcal/mol, corresponding to pulling with a constant force of ~ 160 pN over the binding pocket size of 1.0 nm. Experimental measurements of biotin/avidin using an AFM has suggested intermediate transition states because of an increase in rupture force from 5 pN to 170 pN for loading rates 0.05–60000 pN/s [138], while a later study measured forces from 120 to 300 pN for loading rates 100–5000 pN/s [139].

The dissociation of biotin/strepavidin has recently been explored using magnetic tweezers in a parallel system, measuring dissociation at a constant force (Figure 13) [140]. The dissociation rate of $k_{\text{off}} = 0.9 - 1.4 \times 10^{-4} \text{ s}^{-1}$ at zero force was calculated by observing the rate at which beads functionalized with strepavidin unbound from a surface coated with BSA-biotin. This dissociation rate is nearly two orders of magnitude larger than that from an ensemble experiment and is attributed to unfavorable steric interactions.

5.2.1.2 Antibody/Antigen: Antibodies, proteins which are produced as part of the immune system, are designed to specifically recognize target molecules, antigens, and mediate the immune system response. It is therefore useful to look at this lock-and-key interaction using force spectroscopy to determine the operating range and constraints of this process.

Optical tweezers have been used as an immunoassay strategy for detecting bovine serum albumin (BSA) [141]. Latex beads 4.5 μm in diameter were covalently labeled with different concentrations of BSA and immobilized on a surface with anti-BSA antibodies. The force required for dissociation was found to be concentration dependent, with a minimum detectable BSA concentration of $1.5 \times 10^{-15} \text{ mol/L}$. Optical tweezers have been used to passively observe the dissociation rate of a microsphere coated with IgE from a sphere coated with N- ϵ -2,4-dinitrophenyl-L-lysine, for different coating concentrations and with and without a tether [142]. The presence of the tether reduced the dissociation rate and caused the dissociation rate to decrease with concentration, while the absence of the tether increased the dissociation rate and caused it to increase with increasing concentration. These results show how important experimental design and the effect of surfaces are in determining what exactly is being measured.

There are still many ligand/receptor combinations to be probed at the single-molecule level, with optical tweezers providing an excellent way of measuring loading rate dependent dissociation for weakly bound complexes, while magnetic tweezers provide an excellent way of collecting statistics in parallel. Inhibition of binding needs to be more clearly understood to provide a truly complementary analysis to ensemble experiments.

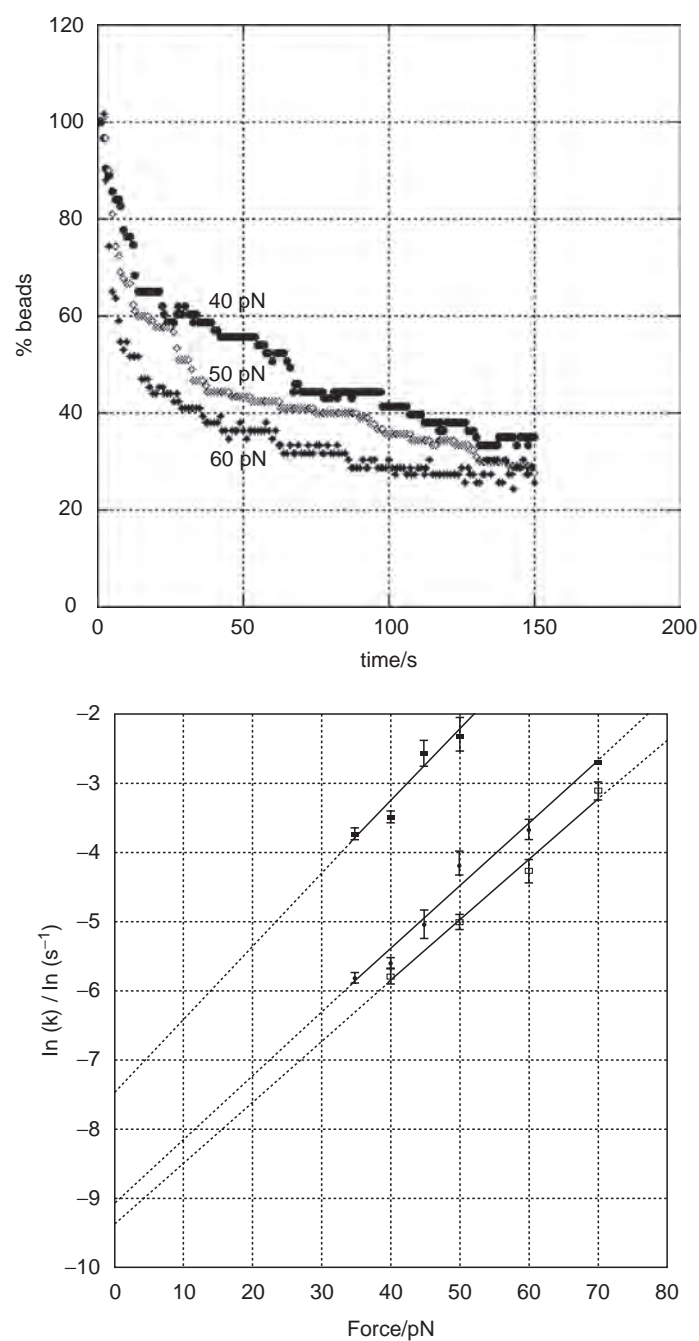


Figure 13. Dissociation of (strept)avidin-coated, $4.5\ \mu\text{m}$ diameter magnetic beads from BSA-biotin immobilized on a surface. (A) With increasing constant force the dissociation rate of avidin coated beads decreases to the non-specifically bound baseline. (B) The rate constants for avidin (open white diamond) and streptavidin (solid black diamond) can be found by extrapolating the force dependent dissociation rate to zero force [reproduced with permission from Ref. 140. Copyright 2005 American Chemical Society].

5.2.2 Biopolymers

Long-chain biopolymers provide many central services in cellular life. From the information coding DNA and RNA, to functional proteins and structural microtubules, the chemical and physical properties of polymers are exploited in many ways. Structurally, biomolecules do not fold randomly but adopt configurations based on specific intramolecular interactions, and an understanding of the folding process will help in understanding the structure and function of unknown proteins and in fine tuning models of molecular dynamics.

The mechanical properties of polymers are typically characterized by the contour length (overall end-to-end length) and the persistence length, a measure of the correlation length. For stiff biopolymers, the persistence length is much longer than the monomer length, and they are modeled with some form of the worm-like chain model; while flexible biopolymers, where the persistence length is close to the monomer length, are best described by the freely-jointed chain model. There is good agreement for a quadratic relationship between the linear density of a polymer and the persistence length, as well as between the fourth power of the radius and the persistence length, though there are exceptions to both relations.

Many of the common biopolymers have already been examined using optical and magnetic tweezers as described below. There are a large number of less common biopolymers including mucin [143], amyloid fibrils [144] which have been characterized by other techniques but not yet by optical or magnetic tweezers.

5.2.2.1 DNA: The right-handed helical structure of deoxyribonucleic acid (DNA), discovered by Watson and Crick more than fifty years ago, is a classic example of intramolecular interactions determining structure. Hydrogen bonding between complementary base pairs in the two strands of the DNA and minimization of hydrophobicity provides a stable structure in a wide range of environmental conditions, while the electrostatic repulsion of the two negatively charged phosphate-sugar backbones determines width and twist. Steric hindrance between the sugar residues attached to the backbone favor a twisted stacking, and particular sequences and conditions can result in either an A or Z conformation rather than the usual B form. It is no coincidence that these unusual conformations have biological relevance, for example, in protecting against radiation damage and activating interferons. Despite being composed of a pseudo-random sequence of four different base monomers, DNA is remarkably uniform and stable, acting as a superior genetic storage carrier. Yet it is capable of being processed by protein enzymes powered by the hydrolysis of phosphate bonds, suggesting that many of its properties and interactions can be probed by optical and magnetic tweezers.

To complement ensemble measurements and passive imaging, single-molecule manipulation of DNA started in 1992 [145] using magnetic beads to measure the force-extension relation for double stranded DNA (dsDNA). A persistence length of 50–400 nm for B-DNA, dependent on salt concentration, was observed, with a value of around 50 nm now generally accepted for physiological buffers at room temperature. Four years later, this time using a dual beam optical tweezer to access higher force, the Bustamante group complemented their earlier work by reporting a structural transition in dsDNA for forces greater than 60 pN [34]. If the dsDNA is not free to rotate, a much less cooperative transition at a force of 110 pN is observed [146]. Despite significant work on this S-DNA phase, the exact nature of its structure remains a subject for debate [147], perhaps to be resolved using other techniques such as electron microscopy. In addition to S-DNA, twisting the dsDNA while stretching using magnetic beads has revealed three more forms of DNA: a Pauling-like form P-DNA, a Z-DNA form with a left-handed helical structure, and an over-twisted, supercoiled sc-P form [146], resulting in a phase diagram of DNA for stretching and twisting (Figure 14a).

Single-stranded DNA (ssDNA) has also been characterized by a force-extension curve, producing a response at high force similar to that of the overstretched S-DNA, a stretching modulus of 800 pN, and a persistence length of 0.75 nm [34] to 3 nm [148]. However, deviations from the normally well-fitting FJC model in the stretching of ssDNA at high and low salt concentrations have been observed [149]. More in-depth reviews on the theoretical and experimental work that has been carried out on the mechanical stretching of DNA can be found in a number of recently published reviews [150, 151, 152].

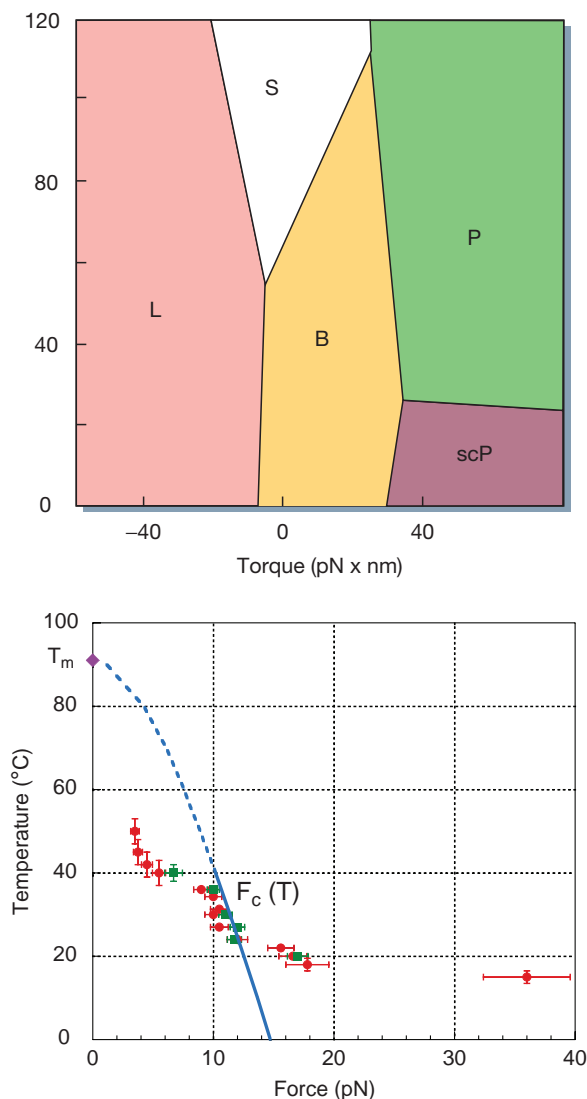


Figure 14. (A) Force-supercoiling phase diagram for dsDNA identifying five phases of double-stranded DNA and (B) Force-temperature phase diagram for unzipping dsDNA, where the blue line represents a simple thermodynamic model [(A) reprinted from Ref. 152 by permission of Macmillan Publishers Ltd; (B) reprinted Figure, with permission, from Ref. 160 by the American Physical Society]. (See Color Plates)

As mentioned earlier, the winding and unwinding of DNA has also been extensively explored. A typical extension versus supercoiling curve is shown in Figure 15. Supercoiling of DNA and the formation of plectonemes are important in DNA packing and processing because of the change in conformation which can be induced by or is a result of enzyme activity. Positive and negative supercoiling have been observed to have similar effects at low force and to agree with the expectations of twisting an elastic rod in a thermal bath [153], but the limits of elastic behavior are evident at higher torques ($> +34$ pN nm, > -9.6 pN nm) with different behavior and possibly different structure [76]. The torsional modulus of dsDNA has been measured to be $C = 344$ pN nm² with magnetic tweezers [154] and $C = 410$ pN nm² with optical tweezers [155], somewhat larger than the generally accepted value of 300 pN nm² from ensemble measurements. As well as studying the effect of supercoiling DNA, rotation can also be used as a diagnostic for determining the number of tethered molecules and also to braid multiple strands of DNA [156]. A good primer on the protocols involved in these single-molecule DNA experiments using magnetic beads has been published recently [157].

In addition to stretching and twisting DNA, the two strands of the double helix can be pulled apart by attaching one strand to a fixed object and the other to a bead which can be manipulated. Sequence dependent force induced unzipping, which is strongly temperature dependent [160], has been measured using both optical [158] and magnetic [159] tweezers. At room temperature partial unzipping starts with an applied force around 12 pN, in agreement with a consideration of the free energy difference between dsDNA and ssDNA. The phase diagram for dsDNA melting by force and temperature, illustrated in Figure 14b cannot, however, be modeled by simple thermodynamic considerations.

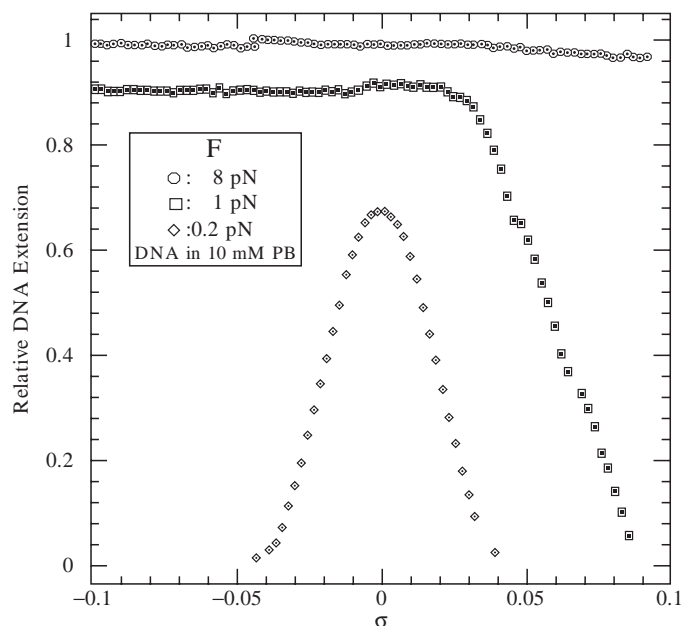


Figure 15. Relative extension of lambda phage DNA versus supercoiling for three different stretching forces, illustrating three different regimes. For forces < 0.4 pN (open diamonds) the response is symmetric, while at intermediate forces (> 0.5 pN, < 3 pN) the extension is insensitive to negative supercoiling, and finally at high force (> 3 pN) the extension is independent of both positive and negative supercoiling [reprinted from Ref. 76 by permission of the Biophysical Society].

The trapping and manipulation of DNA in chromosomes has been investigated [161], with the unfolding of individual nucleosomes observed [162]. Using an optical trap to pull on dsDNA wound round nucleosomes, dissociation of the nucleosomes was observed to increase linearly with the logarithm of the loading rate for forces above 15 pN, releasing 76–80 bp/nucleosome [163], in agreement with the earlier study [162]. There is still much to be discovered about how DNA is packed into a variety of structures, and whether it is purely a stochastic process or whether there is an underlying structure to the process, for which single-molecule approaches may provide useful insight.

One of the unresolved challenges is to tie this single-molecule work on the mechanical properties of DNA to physiologically relevant scenarios. For example, can single-molecule studies provide useful insight into the packing of DNA and the impact of particular sequences, such as those involved in creating unusual conformations, promoter regions, and repetitive tracts?

5.2.2.2 RNA: Over the last two decades, the diversity of the roles ribonucleic acid (RNA) plays within the life cycle has become apparent. In addition to the three major RNA types (mRNA, tRNA, rRNA), small, non-coding RNAs are now recognized as playing a major role in the cell cycle [164]; and a number of viruses transfer their genetic material in the form of double stranded (dsRNA) or single stranded (ssRNA) ribonucleic acid. RNA also plays an active role through RNA interference (RNAi) and micro-RNA (miRNA) in eukaryotes.

dsRNA is structurally similar to A-DNA, forming a right-handed helical structure with a hydrodynamic radius of 2.6 nm and a rise per base pair of 0.27 nm. However, it has a slightly increased rigidity and is less unstable than DNA, primarily due to the 2' OH on RNA which intermediates under basic conditions and the higher energy of the backbone structure of RNA. The secondary structure of ssRNA is also rich, with many intramolecular bonds forming a range of hairpin motifs, which have a role in function.

The persistence length of dsRNA has been measured using a number of techniques, though without the same accuracy as dsDNA [165]. Recently the force extension curve and persistence length of dsRNA was measured (Figure 16) using magnetic tweezers and AFM to be 63 nm [166], less than the 70–75 nm from ensemble measurements and larger than dsDNA. The torsional properties of RNA have not yet been explored, though they are perhaps of less interest because RNA is not processed in the same way by enzymes.

Instead, work has focused on the folding and unfolding of RNA molecules which is critical to understanding the activation and incorporation of RNA but which is complicated by free energy landscapes. A RNA molecule can fold along many pathways and into many intermediate states before arriving at a stable, low energy state, which may or may not be unique. Single-molecule studies, using the techniques of FRET (fluorescence resonance energy transfer) [167] and FCS (fluorescence correlation spectroscopy) in particular, have helped provide significant thermodynamic and kinetic information [168]. Reversible unfolding of RNA, dependent on the concentration of multivalent ions, was first observed using a microneedle [169] with follow-up research using optical tweezers identifying kinetic barriers in RNA, which require forces of 10–30 pN to cross [170]. Work from the same group showing the reversible and irreversible unfolding of small RNA hairpins using optical tweezers [169] required a force of about 15 pN to pull apart the structures, similar to the force required to unzip dsDNA. The pulling and relaxing force curves for some of the hairpins were found to be indistinguishable, suggesting reversibility, while in other RNA sequences the metal binding pockets could be identified.

The diversity and importance of RNA structure will lead to more in-depth studies of RNA under different conditions, to understand phenomena like self-splicing. The interactions of RNA and proteins, RNA and DNA, and DNA and proteins are also important, and optical and magnetic tweezers are the ideal tools to map out their energy landscapes.

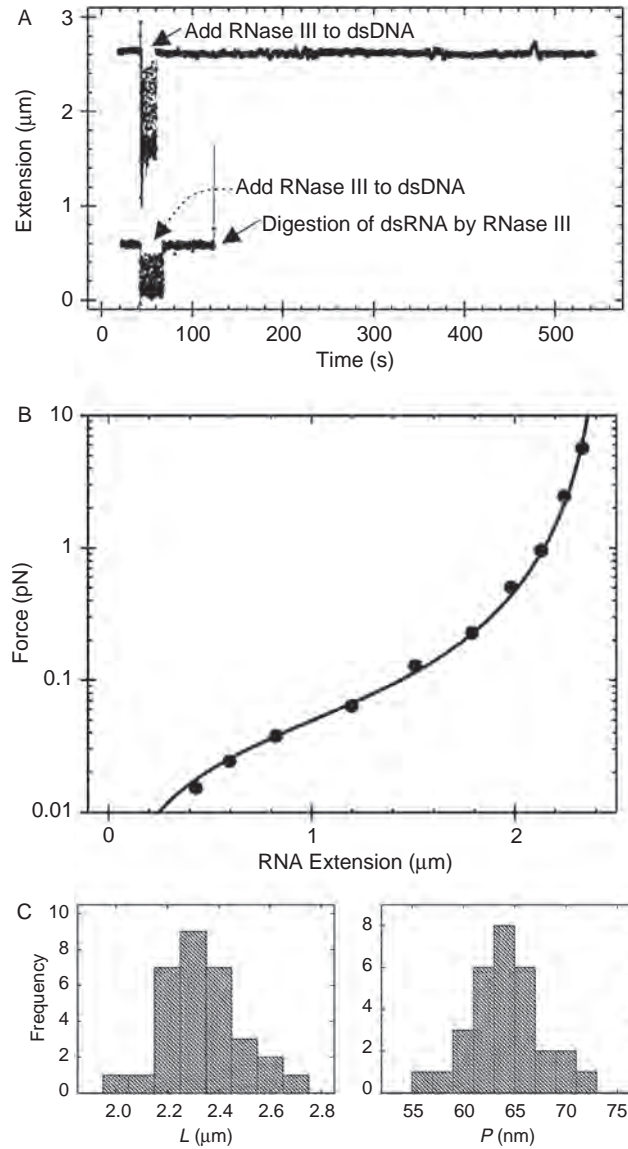


Figure 16. (A) Stretching of a 8.3 kb dsRNA molecule using magnetic tweezers. (B) The force extension curve for a single dsRNA polymer is well characterized by the worm-like chain model, while (C) for a sample of 31 strands the mean contour and persistence length were 2.33 μm and 64 nm, respectively [Reprinted from Ref. 166 by permission of the Biophysical Society].

5.2.2.3 Actin: Filamentous actin (F-actin), a polarized biopolymer of globular actin (G-actin) monomers, is one of the main components of a cell's cytoskeleton, and is involved in the construction of dynamic structures such as filopodia, microvilli, and lamellipodia. The filaments have a right-handed double helix structure with a diameter of 5–7 nm and are up to a few microns in length with a persistence length of $\sim 15 \mu\text{m}$ [171], making them semiflexible. The stretching modulus of actin is $\sim 400 \text{ pN}$, less than DNA, while the torsional modulus is $6000\text{--}7000 \text{ pN nm}^2$, an order of magnitude larger than DNA [172]. Interestingly, the breaking force of the actin-actin bonds decreased from 600 pN to 320 pN under twist, but was independent of twist direction.

The dynamics of the construction, destruction, and cross-linking of actin filaments has been explored extensively by the microrheology community. Microrheometry at the molecular level was pioneered by Ziemann and co-workers in 1994 [88], who measured the viscoelastic moduli of an F-actin network along a single axis using magnetic particles. The magnetically driven beads which were tracked optically provided a quantitative measurement of the frequency-dependent storage and loss moduli at low frequencies (0.1–5 Hz). These measurements were later extended to two dimensions using a magnetic micromanipulator which also controlled rotation [173]. For more active manipulation, the flexibility of a dual beam optical tweezer has been used to tie a knot with a diameter of less than 400 nm in an actin filament in a sucrose solution using 1 pN of force [174]. The knots often broke within 10 s, and this raises the question of how often actin filaments spontaneously break or are actively broken in cells, because only relatively small perpendicular forces are required (1.6 pN), within the range of myosin motors.

5.2.2.4 Microtubules: Protofilaments of polymerized tubulin subunits are complex structural components used for many purposes within eukaryotic cells. Thirteen protofilaments assemble into microtubule assemblies with a 25 nm outside diameter and a 15 nm hollow interior, used in the mitotic spindle during cell division, intracellular transport, and ciliary and flagella motion. In the case of cilia and flagella, the microtubules are arranged in nine pairs of microtubules forming the outer wall and a pair of microtubules in the center (9+2). Microtubules are polarized and have the interesting property of being dynamically unstable, associated with a change in conformation and a negative feedback role in translation and transcription.

The mechanical properties of microtubules have been investigated extensively using optical tweezers [175, 176], with the rigidity found to be dependent on contour length, with a persistence length of the order of 1–10 μm [177], making them stiff on the size scale of a cell. The rigidity of microtubules is 4–34 pN μm^2 , and it has been suggested that this variation is due to growth rate and potential bending modes [178].

The manipulation of microtubules and their dynamic instability are of great interest for intracellular work, for example, to explore nuclear positioning [179]. Further work to include microtubule associated proteins and their influence on both the static and dynamic characteristics of microtubule networks may provide further insight into cellular functions and structure.

5.2.2.5 Intermediate Filaments: In addition there are a range of flexible, nonpolar filaments which provide support in metazoan creatures and a range of eukaryotic cell types. This superfamily of self-assembled filaments are generally cytoplasmic, typically 10–12 nm in diameter, and composed of a range of proteins (40–280 kDa) which include keratins, neurofilaments, and desmin. The intricate structure of these filaments is still debated, though the persistence length of vimentin has been measured with an AFM and is surprisingly short at 0.3–1 μm [180]. Magnetic microrheology has suggested that intermediate filaments play a role in cell stiffening, both naturally and under applied loads [181], though there is still much to discover about this large family of structural biopolymers.

5.2.2.6 Proteins: Proteins are single-stranded biopolymers composed of up to several thousand amino acid residues which fold into a three-dimensional structure which is the key to its function. As a rule of thumb, the persistence length of a protein chain is approximately 5 amino acids, though the presence of charged residues, secondary structures, and background buffer expands the range to 1–10 amino acids [182]. An understanding of protein folding has been a key driving force in single-molecule imaging and manipulation, in part because of the difficulty in determining their structure from sequence alone and in crystallizing many proteins. A number of in-depth reviews of single-molecule protein

studies have been published [183], and only a brief selection of results on particular proteins are considered here.

The first studies of the mechanical unfolding of proteins were carried out on titin, the protein responsible for the passive elasticity of muscle, using AFM [184] and optical tweezers [185, 186], resulting in a force extension (Figure 17) corresponding to a persistence length of 1 nm in the folded state. In the later paper, forces above 400 pN were used to completely unfold the titin molecules. Follow-up work in the Bustamante group observed mechanical failure in titin under repeated stretching [187], another noteworthy result.

Spectrin, a structural protein found in human erythrocytes, consists of two pairs of chains with an end-to-end length of approximately 200 nm. The persistence length has been measured by holding an erythrocyte in a flow chamber with optical tweezers and observing the shape of the cytoskeleton [188]. The persistence length was found to be 5–20 nm depending on salt concentration, and the shear modulus approximately 8.3 $\mu\text{N/m}$ [189].

Collagen, the primary protein in connective tissue, forms a variety of mat and rope structures. Type I collagen is a 1.5 nm diameter helix of three amino acids per turn, and three such strands form a larger molecule called tropocollagen. This has been stretched using optical tweezers [190], and the spring constant measured to be approximately 0.3 pN/nm, though the short length of the collagen (290 nm) and small sample size ($n = 5$) limited accuracy. Follow-up work, using a three-bead design and interferometric imaging, measured the force extension curve of collagen (Figure 18), and fitted it to a worm-like chain model with a contour length of 300 nm and a persistence length of 14 nm [191]. Type II collagen filaments have also been stretched by the same group and found to have a similar persistence length (11.2 nm) and contour length (296 nm), while the cartilage polysaccharide hyaluronan has a smaller persistence length of 4.5 nm [192]. The higher organization of tropocollagen into collagen fibrils, with a diameter of 10–300 nm has yet to be probed at the single-molecule level.

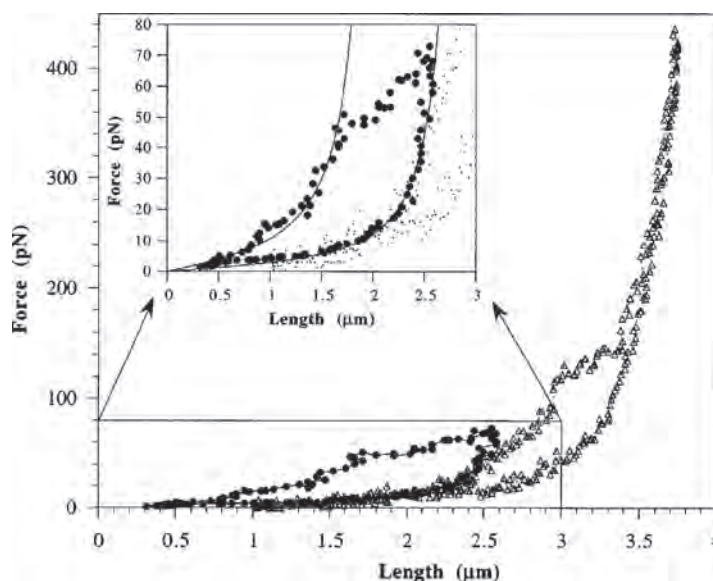


Figure 17. Stretching of a multi-domain titin protein using optical tweezers at a constant rate (65 nm/s). Both partial (closed circles) and complete (open triangles) denaturation were observed. Fitting the partial denaturing results with a worm-like chain model (solid lines) gave persistence lengths of 0.4 nm and 0.9 nm during stretch and release, respectively [reprinted from Ref. 186 by permission of Elsevier].

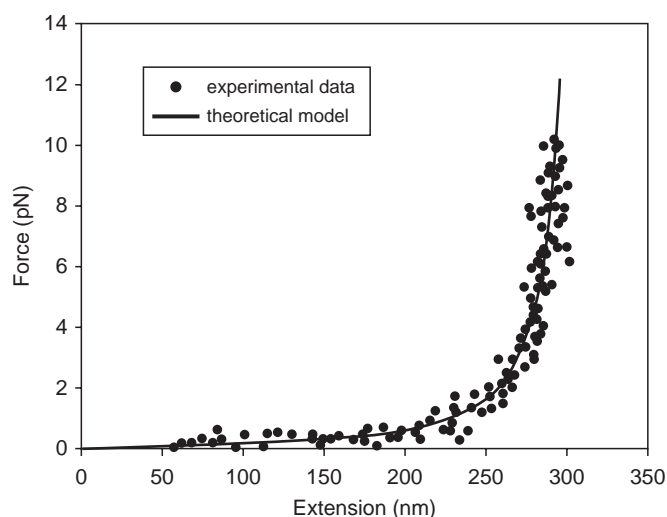


Figure 18. Force extension curve of collagen I stretched using optical tweezers. Fitting with a worm-like chain model gives a contour length of 320 nm and a persistence length of 14 nm [reprinted from Ref. 191 by permission of Elsevier].

As mentioned earlier, membrane proteins can be difficult to isolate and study, but the pigment protein bacteriorhodopsin, composed of seven transmembrane helices, has been unfolded by forces of 100–200 pN [193]. In addition, a number of extracellular proteins, including fibrin with a persistence length of 0.5 μm [194], myelin with a contour length of 53 nm and a persistence length of 0.5 nm [195], and the related bovine A1 protein with a persistence length of 1.6 nm [196] and fibronectin with three subdomains and a persistence length of 0.5 nm [197] have all been characterized. The diversity of proteins and their interactions provide a wealth of systems which can be studied *in vitro*, in addition to the complex problem of protein folding.

5.2.2.7 Polysaccharides: Polysaccharides, originally conceived as biologically inert molecules, have been found to play an active role in a number of important cellular functions, from storing energy to intracellular communication and adhesion. As with other biopolymers, these carbohydrate chains have structural and mechanical properties determined by the glycosidic linkages and the monosaccharide building blocks, but they are often decorated with other groups, which are likely to provide specific recognition in the correct conformation, and also modify the mechanical properties. Unlike proteins or nucleic acids, however, polysaccharides are not genetically encoded, and unlike microtubules or actin, the variability in monomer sequence can lead to a large variety of structures [198].

The basic structure of polysaccharides is determined by the conformation of each individual sugar ring, the stacking orientation of these rings, and finally the coiling induced by entropic or decoration groups. This variation in polysaccharide structure and challenges in isolation and purification make experimental determination more technically demanding. Structural information of bulk polysaccharides can be found from mass spectrometry and X-ray diffraction, though this final approach is limited by the ability to grow crystals and purify a sufficiently large sample. Therefore, there is a hope that force spectroscopy can be used to provide a level of characterization for unknown polysaccharide chains based on their force-extension curves.

The persistence lengths of a number of polysaccharide chains, including cellulose (5 nm), xyloglucan (6–8 nm), xanthan (120 nm), and schizophyllan polymers (180 nm) have been measured using ensemble methods [199], but not yet tackled at the single-molecule level.

The majority of bacterial polysaccharides have repeating motifs of 2–8 residues in helical structures, and can be decomposed into oligomers by mild acid hydrolysis, simplifying sequence analysis. At a more basic level, researchers have focused on monomers which have been purified and reconstituted as homopolymers and naturally occurring oligomers. The persistence length of homopolymers, such as dextran, sclerex, and alginate, has been observed to be 1–20 nm [200], similar to nucleic acids, which are also stacked sugar rings. Since 1997, when dextran chains were stretched by AFM and significant conformational changes observed for forces above 250 pN [201], a number of other polysaccharides have been examined. These experiments have focused on the high force (>1 nN) structural transitions and have not revealed significant information on changes at the low forces around equilibrium, likely to be relevant to cellular interactions. Complementary work with optical and magnetic tweezers would provide a more complete understanding of polysaccharide dynamics in this low force regime.

5.2.3 Force Spectroscopy of Enzymes

The catalytic behavior of some proteins was recognized one hundred and fifty years ago by Louis Pasteur, but not characterized until the work of J.B. Sumner sixty years later. Enzymes can accelerate the rate of a reaction by several orders of magnitude, though the complexity of their structure leads to strong dependence on temperature, pH, pressure, and ion concentrations. The field of proteomics is accelerating our knowledge of proteins, their structure and their function, revealing a dynamic and complicated environment which includes separate but necessary co-factors, activators, prosthetic groups, and inhibitors.

Enzymes perform six basic operations, but of greatest interest for single-molecule studies are the processive enzymes, which are generally associated with creating, repairing, or destroying biopolymers, in particular DNA, RNA, and proteins. These enzymes carry out many rounds of catalysis often by translocation along the substrate before dissociation, making their observation and manipulation more observable than trying to detect single events on a single molecule.

Single events, such as protein binding and dissociation, can be measured in a single-molecule experiment, for example by measuring the dissociation rate k_{off} of a labeled bead from a substrate on a surface as a function of force [140], or by examining the effect of force on the footprint of enzymes which bind specific DNA sequences. Force microscopy has started to provide an enhanced understanding of the dynamics involved in each step of an enzyme's pathway [202]. The majority of enzymes perform only a single catalytic cycle between association and dissociation, generally creating or breaking a covalent bond, making single-molecule observation less beneficial, so research has focused on some of the processive enzymes now described.

5.2.3.1 Exonuclease: Exonucleases are part of the DNA repair process, individually operating to delete mismatched regions, as well as being built into other complexes such as DNA polymerase to allow editing during DNA and RNA synthesis. They are enzymes which hydrolyze nucleotides one at a time from the end of a polymer chain, in contrast to endonucleases which cleave the backbone once at a particular site in the chain. Digestion of DNA or RNA can take place from either the 5' end or the 3' end with a blunt end or an overhang, depending on the flavor on enzyme used.

Of greatest interest have been the enzymes which only convert dsDNA to ssDNA, including lambda, T7, and Exo III exonucleases. The digestion of single dsDNA strand by lambda exonuclease was first studied using magnetic tweezers [203] and more recently by flow [204] and optical tweezers [205], observing a sequence and motif dependent rate. The rate of digestion observed for lambda exonuclease was approximately 6–12 nt/s punctuated by pauses, with a processivity of more than 15000 bp. In contrast, a broad distribution of rates

centered around 100 nt/s has been reported for exonuclease I, also a highly processive DNA exonuclease [206]. At low forces (< 3 pN) the digestion rate was found to be insensitive to loading force, though it is not clear what happens at higher loading forces, due to failure of the tethering complex. The T7 gene 6 exonuclease which is non-processive and the ExoIII nuclease which is processive and conformationally sensitive have yet to be extensively examined at the single-molecule level.

5.2.3.2 RNA Polymerase: Central to the current dogma of biology, the enzyme RNA polymerase transcribes DNA into a mRNA template which is subsequently translated into proteins by the ribosome. The one bacterial and three eukaryotic polymerases are relatively large protein complexes which bind to specific DNA promoter regions and processively transcribe the DNA template using NTP hydrolysis, until termination is initiated by a number of mechanisms.

The force generated by RNA polymerase during transcription was first measured ten years ago using optical tweezers [207]. As with many of these enzymatic experiments, the polymerase was immobilized to a surface, while the biopolymer substrate was attached to a bead held in a trap. The stall force has been measured for a variety of RNAP to be 14 pN to 34 pN [208], with an average velocity of 7–16 bp/s with no applied force. Interestingly, the enzyme utilizes only a small fraction of the energy liberated from ATP hydrolysis for mechanical work [209].

Translocation of the RNAP is not a rate-limiting step because an opposing force up to 10–20 pN does not slow the rate; but ≥ 30 pN of opposing force triggers a conformational change in RNAP that allows backtracking over 5–10 bp [210]. More recently, the binding, elongation, and escape of RNAP has been observed, with a $k_{off} = 2.9 \text{ s}^{-1}$ and a processivity of $k_{pol} = 43 \text{ nt/s}$ [211].

There is much concerning the stability and processivity of RNAP that is poorly understood. Beyond working towards a more complete understanding of the molecular mechanisms underlying transcription [212], a more complete analysis of conditions for the initial ~ 8 bp hybrid formation before formation of a stable elongation complex in bacteria would distinguish between a number of competing models, and the prediction of pauses and backtracking [213] would assist in understanding transcription fidelity. The more complex eukaryotic polymerases pose as many challenging questions, among which are the interactions between the transcription complex and nucleosomes, and whether propagation causes torsional tension and the activation of DNA promoter sites.

5.2.3.3 Helicases: The stable double-stranded nature of DNA requires that for many processes to occur, unwinding needs to be amongst the first steps. There are tens of enzymes in the helicase family that carry out unwinding of DNA or RNA as part of recombination, repair, replication, and splicing. They are flexible in polarity and substrate, and processive, consuming ATP as they translocate along the strands. Recent structural data on these enzymes has helped elucidate the nature of both the dimeric and hexameric subfamilies, though many questions remain on how hydrolysis couples to unwinding and translocation and whether a rolling model or inchworm model is appropriate [214]. Mutations in the RecQ helicase have been associated with Bloom, Werner, and Rothmund-Thompson's syndromes, though how these affect the different roles of RecQ is not clear.

A number of helicase enzymes have been examined using single-molecule force spectroscopy, observing a variety of results. RecBCD, a processive, DNA motor enzyme with both helicase and nuclease activities, can unwind DNA at rates of 500 bp/s, has a processivity of more than 40000 bp [215], and has been characterized using optical tweezers (Figure 19) [216]. Stop/start motion and backtracking were observed, as well as a substantial variation in unwinding rates, with the enzyme migrating at a rate of 21 bp/s for extended periods, substantially different from previous results.

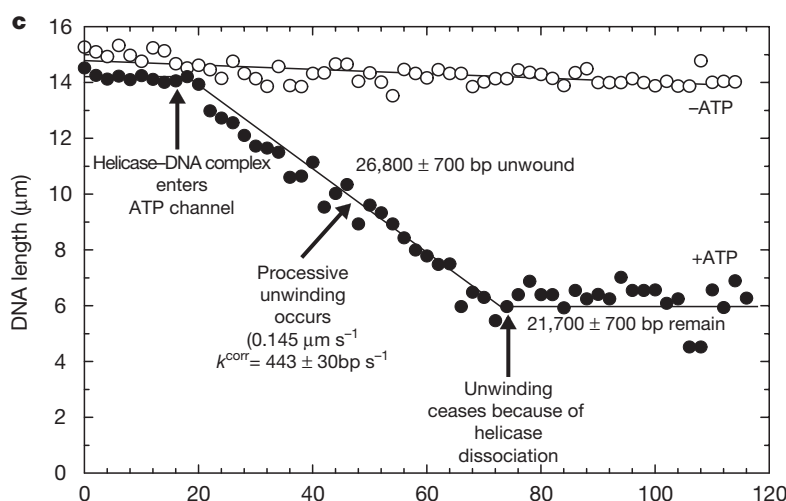


Figure 19. Unwinding of dsDNA by a RecBCD enzyme tethered to a bead held in an optical trap in the flow cell. The dsDNA, stretched by the flow, was fluorescently tagged to determine its length [reprinted from Ref. 215 by permission of Macmillan Publishers Ltd].

Another member of the family, the RuvAB helicase complex, which mediates the Holliday junction migration by denaturing and reannealing, has been studied recently with magnetic tweezers [217, 218]. The branch migration rate was observed to be 43–98 bp/s with pauses of inactivity and a processivity of 7000 bp. Positive and negative loading forces had minimal impact, up to the maximum applied force of 23 pN.

UvrD, a DNA repair enzyme with helicase activity, has also been studied using magnetic tweezers [219]. The number of bases unwound per catalytic cycle was estimated to be 6 bp, with a slow unzipping and reziping rate of approximately 250 bp/s, and fast rehybridization events of 2300 bp/s with complicated burst patterns. Results also suggest that the enzyme unwinds as it moves 3' to 5' on one strand and allows hybridization as it switches across to the other strand, as opposed to dissociating. The purpose of strand switching is not clear, or whether stretching the DNA substrate has a significant effect on the rate and efficiency of the enzyme, an important consideration in any of these enzymatic studies.

5.2.3.4 Topoisomerase and Gyrase: In the course of unwinding DNA for processing, additional coiling can cause the formation of secondary structures which could potentially interfere with processing. Topoisomerases guard against excessive positive and negative supercoiling of the DNA in vivo. The subfamilies are distinguished by whether the cleavage used to relax the supercoiling is single-stranded or doubled-stranded [220]. The importance of these enzymes is exemplified by the role reverse gyrase plays in stabilizing the DNA structure of extremophiles and by the fact that many antibiotic and chemotherapy drugs interfere with topoisomerase function. An in-depth article describing the single-molecule research carried out on topoisomerase using optical and magnetic tweezers has recently been published [221] and highlights are only briefly mentioned here.

Using magnetic tweezers, the supercoiling of DNA [76], and the operation of IA [222] IB [223], II [224] and IV [225] topoisomerases involved in the formation or relaxing of supercoils have been examined. Each enzyme has been found to have its own operating characteristics, preference for relaxing left- or right-handed supercoiling, and rates. For example, the rate of supercoil relaxation of eukaryotic type II topoisomerase decays exponentially from the maximum of ~3 cycles/s with applied force, whereas prokaryotic type IV has a rate

~2.3 cycles/s independent of force up to 2 pN, but rapidly drops to zero above 2 pN [221]. The rates measured in these single-molecule experiments are eight times greater than equivalent ensemble measurements [226], though it should be noted that single-molecule experiments focus on the movement on the enzyme once it is bound and do not provide good statistics on the unbound activity.

As with many single-molecule experiments, work on topoisomerase has started to answer questions about the physiological functions and limitations of these enzymes, but in the process have raised as many questions, such as those concerning their specificity and sensitivity to global topology while acting at a local level.

5.2.4 Molecular Motors

A wide range of motor proteins exist in nature, with a diversity of structures and functions. From the linear cytoskeleton motors, kinesin and myosin, to the rotary membrane motors, ATP synthase and bacterial flagella, motors provide active transport, defeating the limitations of diffusion, and allowing the construction of macromolecular structures such as muscle and axons many times longer than a normal cell.

The majority of motors bind, hydrolyse, and unbind ATP or GTP to induce conformational changes, providing motion through a process of detachment, movement, and rebinding. Some motors, such as ATP synthase, can run the process in reverse, generating conformational changes to store chemical energy. In their operation, motors trade off speed for processivity, step size for load size, and overall size with all other factors. Each ATP hydrolysis supplies approximately $\sim 20 k_B T$, or 80–120 pN nm, which places an upper limit on the step size and torques possible in a single hydrolysis cycle. The maximum catalytic rate is determined by availability and diffusion ($\sim 10 \mu m^2/s$) of ATP and by the hydrolysis cycle time (~ 1 –100 ms).

Beyond the motors considered here, a number of other motors have been examined at the single-molecule level, most notably the portal motor of the phi-29 virus which has been investigated using dual optical tweezers [227]. The motor packs the viral DNA into the capsid with such efficiency that the pressure inside is about 60 atmospheres, working against forces of up to 57 pN, slightly higher than the estimated 50 pN repulsive force from the fully packed 6.6 μm long viral genome. The step size per ATP cycle was found to be less than 5 bp with a rate of packing fluctuating up to a maximum of 20 bp/s and pauses of variable duration as well as occasional slippages.

Our knowledge of molecular motors, as with most proteins, is inversely proportional to their molecular weight, with kinesin being the most closely studied. We will now consider some of the more common motors.

5.2.4.1 ATPase: The ATP synthase enzyme is one of the most conserved enzymes in eukaryotes, acting as the source for the ubiquitous energy currency adenosine triphosphate (ATP). Generally, ATP synthase is a membrane rotational motor which catalyses the synthesis of ATP from ADP, driven by a flux of protons due to the electrochemical potential across the membrane, and operates with an efficiency close to 100%. The motor is fully reversible and stoichiometric measurements had suggested, assuming integer values, that three protons were required to synthesize one ATP in mitochondria, while more surprisingly four protons were required in chloroplasts.

One of the simplest forms of ATP synthase is that of *E. coli*, the soluble portion of which, F_1 ATP-ase, can be dissociated from the hydrophobic F_0 proton channel by relatively mild salt treatment. Dramatic support of the rotational model came in 1997 from Masasuke Yoshida's group in Japan [134]. They tethered the β subunit of F_1 ATP-ase to a glass surface and attached a fluorescently-labelled actin filament to the central γ subunit, and observed counterclockwise rotation only under conditions of ATP hydrolysis. In the same year, an alternative approach using a small chromophore on the γ subunit instead of the long actin filament, observed the polarization anisotropy on activation, again consistent with the three-step

rotary model [228]. This work was followed by Yasuda et al. [229], who observed discrete 120° rotations under low ATP concentrations, as illustrated in Figure 20, and judged the distribution of the dwell times to be concentration dependent, with a torque of up to 80 pN nm generated on ATP hydrolysis. The reversibility of the motor was demonstrated more recently [230] using a magnetic field to rotate a magnetic particle attached to the stalk to generate ATP.

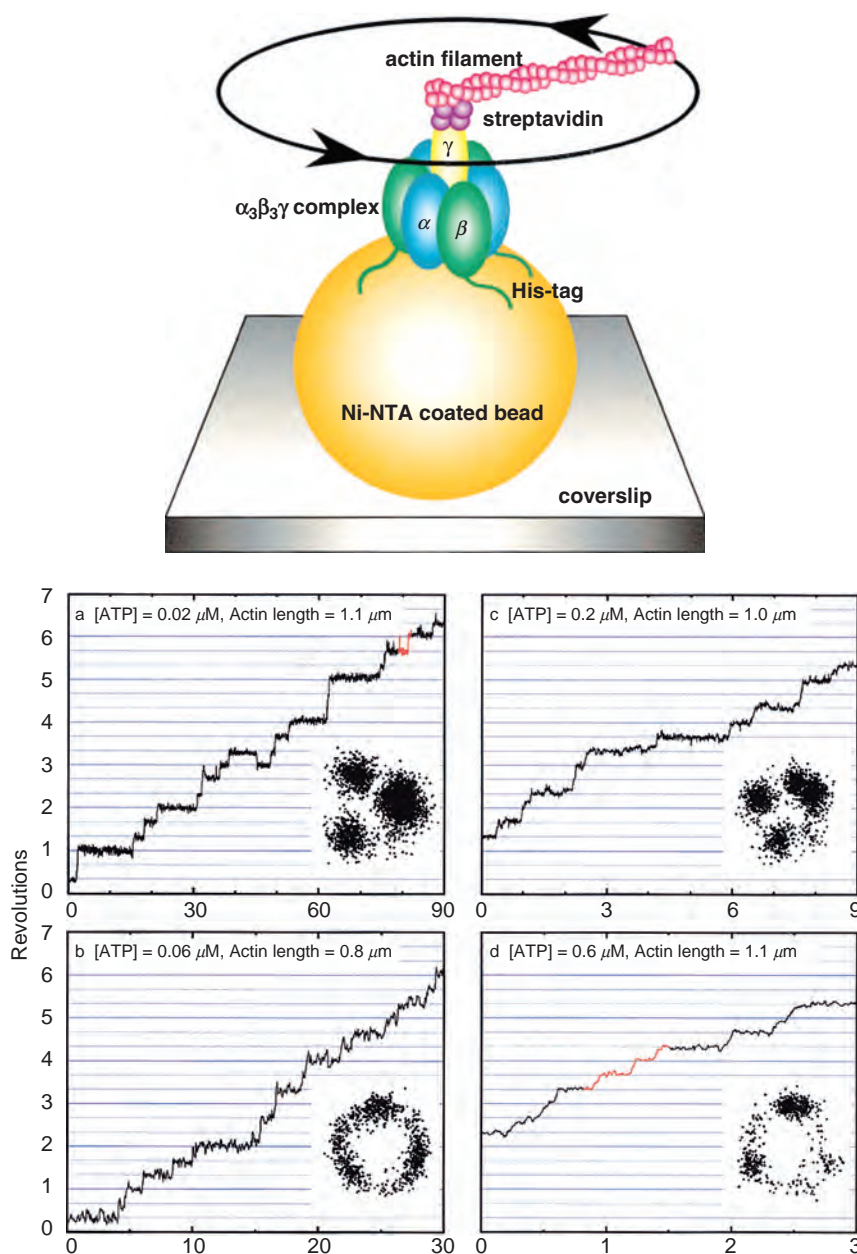


Figure 20. (A) Experimental setup used to measure the rotation of the F1 ATPase subunit. (B) Discrete rotations of 120° can be seen in the time course of the rotating filament [reprinted from Ref. 229 by permission of Elsevier]. (See Color Plates)

Isolation of the full F_0F_1 complex is now possible, and substeps of 40° and 80° have been observed along with the concentration dependent rotation rate of up to 350 rps under saturating ATP concentrations [231].

Although there is now good understanding of the structure and kinetics of the F_1 subunit, there are still many interesting questions to be addressed concerning the mechanism of the F_0 subunit and whether the ATP synthase assembly in eukaryotes and chloroplasts is significantly different from those in bacteria.

5.2.4.2 Myosin: The myosins are a huge family of linear motors which move non-reversibly toward the positive end of actin microfilaments. Actin is the principle component of thin filaments in muscle fiber, which slides past the thick filaments consisting mainly of myosin, driven by ATP and the presence of Ca^{2+} . Polymerized F-actin forms a right-handed helix with a 72 nm pitch, with each individual myosin in the thick filament binding only briefly and each head contributing an average force of 3–6 pN.

A representative member of the family is myosin II, a two-headed motor involved in cell movement and also found in skeletal muscle, which shares many of the same structural features as kinesin [232], but is nonprocessive. This makes measurement more problematic because a single molecule will not track along a filament over a long distance; instead each catalytic cycle is punctuated by a diffusional pause. Therefore a myosin molecule must be artificially held in close proximity to an actin filament by a weak trap to observe multiple steps in a reasonable time period. It is worth remembering that thermal fluctuations on a trapped particle can result in displacements of tens of nanometers, further complicating the process.

The first single-molecule measurements of the myosin II step size used an actin filament stretched out between two polystyrene beads and held close to myosin bound on a surface-immobilized bead [233]. Although there were numerous experimental issues with this setup, many of which have continued to plague these measurements, a mean displacement of 11 nm of the beads holding the actin filament was observed. A complementary variability in step size, in the range of 3–17 nm, has also been observed by a number of optical tweezer studies [130, 234]. Complementary work using a microneedle [235] measured the peak force to be 6 pN, with an average of 3 pN and a cycle rate of 10–20 Hz with step sizes of 20 nm. A more careful analysis, using aligned mixtures of actin and myosin as opposed to the random orientations used earlier, found that the step size was strongly dependent on orientation [236]. The effect of load has been difficult to quantify; however, there is evidence that the normally low duty cycle myosin II may become a high duty-ratio motor under force [237], though the effect of force on the kinetic and molecular mechanics is not well understood.

The diversity of the myosin family is illustrated by the contrast between myosin II and V. Myosin V is a two-headed motor which transports vesicles along actin filaments over long distances. The ADP release step is rate limiting, resulting in the bound state being the predominant intermediate. Several groups have tried to identify what determines the step size of myosin-V with a wide range of results [238]. The length of the arm is determined by the IQ motifs and this in turn is thought to determine the overall transport velocity [239]. Experiments have observed 36 nm [240] and 74 nm [241] steps leading to consideration of both inchworm and hand-over-hand models, while experiments with myosin-Vs containing reduced or increased numbers of IQ repeats (and thus lever arm length) concluded that the longer this arm, the faster the transport velocity in vivo [239]. More recent results [242, 243] have confirmed the 72–74 nm step, hand-over-hand model.

In addition to myosin II and V, the mechanics of myosin VI [244] and I [245] have also been the subject of single-molecule experiments, as well as the biochemistry of the power-stroke cycle [246, 247]. The adaptation of the power stroke by each member of the myosin family to meet its biological function has provided a rich diversity in similar experiments. Many challenges remain in characterizing these linear motors, but further quantitative

measurements will provide insight into a wide range of active transport processes, from muscle contraction to intracellular transport. These studies help underline a major quest of the single-molecule biophysics community, that of assigning potential cellular functions based on mechanical characterization.

5.2.4.3 Kinesin: Kinesin is a processive, linear cytoskeleton motor which moves non-reversibly toward the positive end of microtubules. Microtubules are 30 nm diameter polar helices composed of thirteen tubulin subunits per turn and critical to structures such as flagella, cilia, and the mitotic spindle, as well as maintaining cell shape and a transport network. Kinesin is a tetramer, composed of two light chains connecting to the cargo and two heavy chains containing the motor domain heads, one of which was believed to be bound to the microtubule at all times [248] to give the ability to transverse many microns at a rate of ~ 800 nm/s before dissociation [249].

Both tubulin and kinesin can be purified and reconstituted *in vitro*, making single-molecule experiments possible. The first direct measurement of the proposed 8 nm step size, corresponding to the tubulin repeat distance, came from the Block lab, with a silica bead attached to a kinesin and tracked as it advanced along microtubules immobilized on a coverslip [117]. The rate of movement was found to slow linearly with increasing force, up to a stall force of 7 pN, with the occasional step backwards [250] explained by the increasing load decreasing the probability of the catalytic cycle producing a mechanical step. Analysis of the dwell time [251] and of the fluctuations [252] concluded that an ATP binding, rate limiting process occurred before the 8 nm advance, as illustrated in Figure 21.

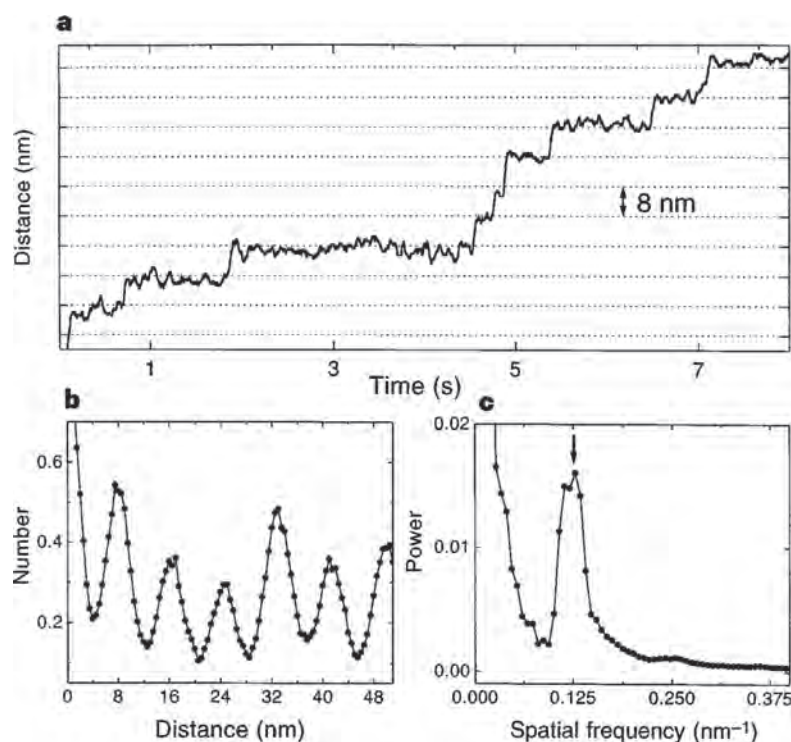


Figure 21. (A) Position of an optically trapped bead being pulled by a single kinesin protein. 8 nm center of mass steps are observable with variable dwell times. (B) Histogram of a pairwise comparison of distances from (A), clearly illustrating a 8 nm periodicity. (C) Power spectrum of the data from (B) showing a peak at the reciprocal of 8 nm. [reprinted from Ref. 252 by permission of Macmillan Publishers Ltd].

As with myosin there has been controversy over whether kinesin moves by a hand-over-hand motion or an inchworm motion where one head always leads. Recent measurements [253] strongly support the hand-over-hand model, with tracking of fluorescent-labeled heads supporting alternate 17 nm and 0 nm step sizes for each head, and a corresponding 8 nm movement of the center-of-mass for each ATP cycle. Further, both heads are bound or interacting with the filament during the dwell time between ATP binding events, and the hand-over-hand motion is likely asymmetric to avoid twisting the cargo, though the expected limping due to twisting of the stalk in this model has not been observed in wild-type kinesin [254]. Direct observation of the motion of the heads and stalk during the step process requires faster time resolution than currently available, but would help solve some of the unresolved uncertainties.

Work is ongoing [255], studying a range of other kinesins, including mitotic kinesin and the four-headed BimC, as well as the effect of mutations, some of which are associated with neurological diseases. Beyond these single-molecule experiments, the question of how a number of kinesins can carry cargo cooperatively over much longer distances still has to be addressed.

5.2.4.4 Dynein: Complementing kinesin, dynein is a linear cytoskeleton motor which move non-reversibly toward the negative end of microtubules. It is a large motor protein derived from the AAA family and well conserved. Dynein comes in two flavors: axonemal dynein, which provides the connective bridge and motor in cilia and sperm tails; and cytoplasmic dynein, which complements kinesin in subcellular vesicle transport.

An early experiment showed that latex beads coated with cytoplasmic dynein moved smoothly along microtubules in comparison to the step-wise motion of kinesin [256]. Follow-up reports noted that cytoplasmic dynein moved with an average speed of 5 $\mu\text{m/s}$ along the microtubules and were able to backtrack distances of up to 100 nm [257], with some diffusing randomly along the microtubule [258]. Using optical tweezers, the maximum stall force was found to be 1.1 pN with ATP concentrations above saturation and linearly dependent on ATP concentration below saturation [259], similar to the stall force measured for axonemal dynein [260]. The step size has also been observed to decrease from a mixture of 24 nm and 32 nm steps down to 8 nm with increasing load, in contrast to the constant step sizes of kinesin and myosin under load. As with the other linear motors, dynein is driven by ATP hydrolysis, though from these measurements it operates with only 10% efficiency in comparison to the 50% efficiency of kinesin.

There is still much to be learned about the mechanics and kinetics of dynein [261] in its various roles: for example, where the ATP binding takes place, both physically and within the power stroke; why the step size is geared to load; and what the effect of mutations linked to inherited motor neuron disease is on transport. These are all unresolved questions which can potentially be answered using a single-molecule, force spectroscopy approach.

5.2.4.5 Cilia and Flagella: The flagella motor, with variations found in many bacteria and protists, is a rotational motor which can change direction under physiological control. It is driven by a proton or sodium gradient, producing very high torque with a small step size. The flagellum and cilium are constructed from microtubules in a 9+2 arrangement, with force being created by dynein motors pushing against parallel microtubules to create motion. Cilia, shortened forms of flagella, appear in all vertebrate cells in the form of a primary, non-motile cilium with 9+0 arrangement, while motile forms have the 9+2 arrangement. Cilia play an important role in our sensory perception as well as enabling protists to move.

Motile bacteria like *E. coli* are propelled by a number of flagella forming a bundle several microns long. Block et al. [262], making one of the first quantitative measurements

with optical tweezers, measured the nonlinear torsional compliance of tethered *Escherichia coli* and a motile *Streptococcus*. Follow-up work in the Berg lab, using a piezoelectric stage to rotate the tethered *E. coli*, found that the motor generated ~ 4500 pN nm of torque at all angles, regardless of whether or not it was stalled [263].

In addition to *E. coli*, the swimming force of a wide range of other motile cell types have been characterized, including human sperm [264], *Chlamydomonas* [265], and *spiroplasma* [266]. In the case of sperm, near-infrared light at 760 nm was found to lead to paralysis and cell death within a minute [267]; but this has not prevented optical tweezers operating at 1064 nm being used to insert sperm into a trapped oocyte [268], and to study the influence of pentoxifylline, to decrease the viscosity of blood, on the swimming behavior of sperm [269]. Potentially there are many other force characterizations which have yet to be carried out on the many varieties of algae and ciliates, perhaps addressing unresolved questions on the beating of cilia and the influence of drugs on motile opportunistic bacteria.

5.3 Cellular and System-Level Force Spectroscopy

One of the greatest challenges working within a cell or organism is to interact with and only with the targets of interest in a controlled way. Optical and magnetic tweezers require an object of at least 100 nm in diameter with favorable properties in order to exert a useful force. The presence of such a particle would displace at least 10,000 biomolecules within a cell and be constrained by the cytoskeleton. Imaging in and around live cells is also hampered by the refractive index changes and increased scattering, limiting resolution and signal to noise. In addition, the presence of an uncontrolled environment can lead to multiple specific and nonspecific interactions, complicating analysis. Therefore the majority of in vivo studies with optical and magnetic tweezers have focused on the plasma membrane and on the manipulation of whole cells.

5.3.1 Membrane and Cytoplasm Force Spectroscopy

The ability to apply a mechanical force to a cell or one of its components is of fundamental interest in understanding the influence of environment on cell development. Biomechanics has made great strides in describing the effects of force at the macroscopic ensemble level; and contact/fluid flow techniques have been used to observe the effects of force at the cellular level, though these approaches are limited to applying force to the outside of the plasma membrane over a relatively large area. The non-contact manipulation of submicron particles with optical and magnetic tweezers has refined these studies, creating as many new questions as answering existing ones, thanks to the complexity of the cellular environment.

Following Crick and Hughes's twisting, dragging, and prodding of the cytoplasm of an explant using magnetic particles in the 1950s [1], Yagi examined the properties of the protoplasm of an amoeba [270], again exploiting the then unique ability to apply a force to a particle within a cell. In the 1970s, Cohen [271] and Valberg et al. [272] started studying the retention of magnetic aerosols of ferromagnetic particles in the lung macrophages, which led to the development of magnetic twisting cytometry by Valberg and Butler [273] in 1987. Butler went on to work with Wang and Ingber [274] to study the effect of mechanotransduction using magnetic particles and to propose a tensegrity model for cell structure. Askhin began the optical manipulation of cells, studying the viscoelastic properties of plant cells in 1989 [121], leading over the next fifteen years to a wide range of studies of motile and immotile cells, focused on characterizing cell morphology and manipulating cell functions. Recent reviews of cell mechanics and mechanotransduction [275] and of mechanical manipulation of cell membrane [276] have been published, and only some notable results are considered here.

Measurement of the mechanical forces involved in focal adhesions created by integrin proteins, the bridging focal adhesion proteins, and their associated complexes has been carried out with both optical [277] and magnetic tweezers [91]. Force applied to transmembrane proteins involved in these processes is met with increased traction forces and less displacement [278], while other membrane proteins not involved can be dragged around the membrane to probe structures which cannot freely diffuse [279]. A permanent magnetic microneedle has been used recently to probe a single β 1 integrin adhesion site [81]. Small ($< 0.1 \mu\text{m}$) displacements for forces as high as 130 pN were observed and were dependent on the degree of assembly of the focal adhesion site. The formation and disassembly of cell adhesion sites involves complicated dynamics and assemblies of proteins, but good progress has been made toward pulling together single-molecule force spectroscopy and the results from more traditional molecular biology.

Other membrane proteins have been investigated using optical or magnetic tweezers, including the cell adhesion proteins LFA-1 [280], NrCAM [281], and E-cadherin [282]; the λ receptor in *E. coli* [283]; the transferrin receptor [284]; the transmembrane band 3 in erythrocytes [285]; and the adhesion of the von Willebrand factor (found in the subendothelium) to wild-type and mutant platelet membrane receptors [286]. The tracking of membrane proteins is particularly relevant in understanding how cells react to and survive mechanical stress and how movement, adhesion, and repair processes are governed [287].

The influence of drugs on the plasma membrane has begun to be investigated and will be of growing interest as the properties of cells and proteins become better known. The effect of the amphipathic drug salicylate on the mechanical properties of the plasma membrane was found to be minimal, discounting one of the competing theories for a side effect of the drug [288]. Using similar approaches, optical tweezers may help to play a role in pharmacology, providing a way of screening drugs [289].

Observation and manipulation of intracellular transport using optical and magnetic tweezers has been of interest to a small but growing number of microbiologists. Optical tweezers have the advantage here of being able to apply force directly on an organelle. Ashkin used this advantage in 1990 to manipulate organelles and estimate the force used to translate them along microtubules at 2.6 pN [290]. Optical tweezers have also been used to measure the forces involved in lipid vesicle trafficking in *Drosophila* embryogenesis, observing discrete steps in the applied force up to the stall force of 1.1 pN, associated with decreasing numbers of motors [291].

In addition to tracking and manipulating organelles, intense light can also be used for optoporation [292], and to cut [12], manipulate [293], and isolate [294] chromosomes and human gametes [295]. Optical scalpels have also been used on trapped plant cells to perforate the cell wall, the mitochondria, and chloroplasts, and to move them around [296]. A more comprehensive review of the destructive use of lasers in cell biology has recently been published [297].

There are many unresolved questions concerning the dynamics of membranes and associated proteins, lipids, and polysaccharides which optical and magnetic tweezers can help address. For example, questions on the nature of lipid rafts and the function of polysaccharides in adhesion, defense, and signaling could be addressed by force spectroscopy in the range of 1–100 pN. Although mechano-transduction and light-directed cell growth have already demonstrated the ability to manipulate cell functions, there is significant interest in manipulating tagged transmembrane proteins and organelles to characterize and control more defined cell functions, for example, cell growth, division, signaling, and movement.

5.3.3 Cell Manipulation and Characterization

A wide range of cells have been trapped and manipulated, in particular with optical tweezers, to explore motility and other cell functions. The ability to trap a cell without

damage and either manipulate or observe it using another technique is a very powerful asset in understanding cellular properties.

As mentioned early in the chapter, motile cells have been examined at various levels, from the force generated by swimming sperm to the coordination of flagella in *E.coli*. Motile cells sensitive to their environment, for example, the gravisensing *Chara* rhizoids [298] and magnetotactic bacterium *Magnetospirillum magnetotacticum* [299], have been explored using optical and magnetic tweezers, respectively. The vast diversity of archae, protists, and multicellular organisms that can sense and respond to fields means there are many more examples to explore which will further our understanding of many processes, including how organisms can navigate according to the Earth's magnetic field.

The interaction of immotile cells with their environment and each other can also be probed using optical tweezers. The binding of cells to a surface, such as the binding of fibroblasts to a fibronectin coated surface [300] and *E.coli* to a self-assembled monolayer of mannose [301], has been explored. Contact between effector cells of the immune system and their target cells held in optical traps can be used to establish the attack kinetics of a natural killer on an erythroleukemia cell [296]. There are many interesting interactions to explore, from the gruesome predator skills of *Didinium* to the more benign questions of plant cell adhesion under the environmental extremes to which they are exposed.

The morphology of cells can be characterized passively by their light refractive and scattering properties, and the results routinely used in automated cell sorting machines. It is unclear whether the information gained by magnetic or optical tweezer assays can outweigh the assays' complexity and limitations in throughput, when compared to competing cell characterization techniques such as fluorescent labeling, scattering, and dielectric spectroscopy, all of which offer single-molecule analysis and fast, straightforward screening. But in large cell populations where traditional cell sorting is not preferable, then optical tweezers can be used to isolate single cells [302], though throughput is substantially lower. Optical tweezers have also been used to isolate archaea according to 16S RNA labeling and to carry out PCR to identify the population [303].

The mechanical deformation of red blood cells, typically 7–9 μm in diameter, has been of particular interest because the cells can deform and flow in capillaries less than 3 μm in diameter. Intense light has been used to actively deform cells and to observe their recovery, in particular red blood cells [304] and chloroplasts in leaf tissue [305]. The spread in elasticity of sickle-shaped red blood cells has been found to be marginally different from that of normal red blood cells [306]. However, the story is not straightforward as red blood cells are themselves subject to a range of factors affecting their elasticity [307]. Although a powerful demonstration of the ability to manipulate and quantify the mechanical properties of individual cells, the complexity of and poor distinction between normal and sickle cells are unlikely to lead to a competitive assay.

The dual role of particles for both passively measuring displacements and actively applying force is highlighted in a recent study of single cardiac myocytes [308]. Heart cells can beat spontaneously, or be induced to beat, causing micron deformations with an average contractile force of 13 μN , which can be observed by a labeled bead. The authors then proceeded to apply a reported force of 5 μN to the 20 μm bead, two orders of magnitude higher than any other magnetic force reported on a single bead, using a 5 mm diameter permanent magnet at a distance of 5 mm, and observed a shortening in the contraction length of the myocyte.

These are only a few of the many examples where whole cells have been manipulated using optical and magnetic tweezers. Interactions cannot be quantified as clearly at the cellular level as in the single-molecule studies described earlier, though qualitative observations and estimations can be made.

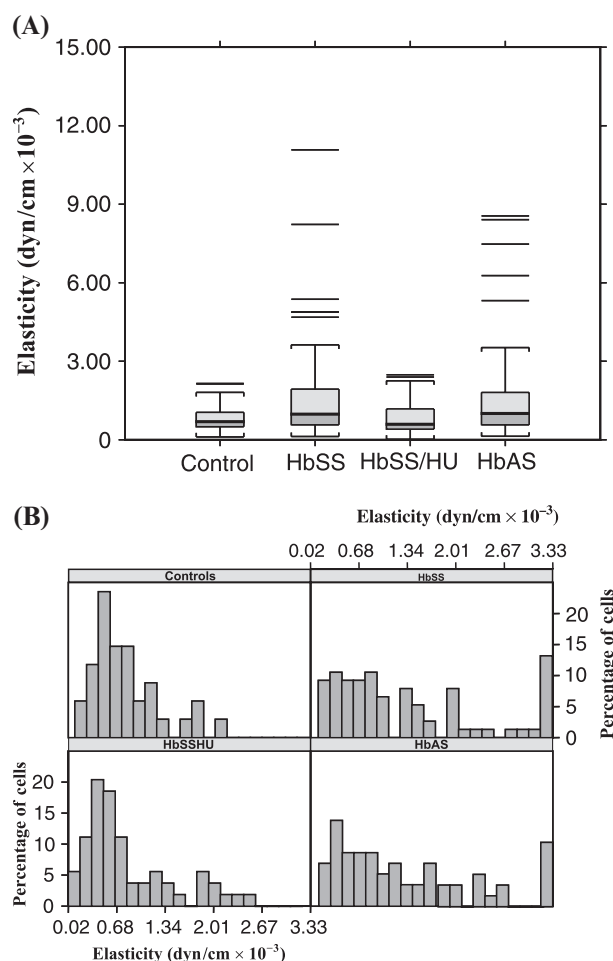


Figure 22. (A) Box plot and (B) histograms of the elasticity of red blood cells from subjects measured using optical tweezers. HbAS are homozygous sickle cell mutants, with HbSS showing characteristic traits, and HbSS/HU are subjects treated with hydroxyurea [reprinted from Ref. 306 by permission of Macmillan Publishers Ltd].

6 Conclusions and Future Prospects

Optical and magnetic tweezers are unique tools for force microscopy at the cellular level. They are unmatched in the sensitivity and flexibility of the force they can apply. The non-contact nature of both techniques removes complicating surface interactions or limiting environmental conditions and leads to the ability to rapidly and completely release trapped objects. As described in the first half of this chapter, the ability to develop techniques which can image particles with nanometer resolution and resolve piconewton forces at kilohertz frequencies has pushed back the limits in studying the force spectroscopy of single molecules and their interactions. Although their use in non-specialized labs has come about only in the last fifteen years, the success and commonplace usage of both techniques are perhaps best indicated by the decrease in their use as keywords in published papers.

The low force regime available with optical or magnetic tweezers means there are a range of forces, nanonewtons and higher, that can only be probed by contact probe methods.

In addition, the complexity and rate of dynamic processes can exceed the resolution and feedback possible in current optical detection systems. Furthermore, both of these non-contact techniques have a limited depth of operation, favoring single-molecule *in vitro* studies. However, from a biological perspective, the largest handicap to both approaches is the need to artificially attach a micron-sized handle with which to apply a significant force without causing modification of behavior. Steric constraints from the presence of these particles again favor minimally reconstituted biological systems and are always a consideration in interpreting results. Nonetheless, these disadvantages are not show-stoppers, as illustrated by the depth and breadth of the studies described in the second half of this chapter. Table 2 summarizes the physical properties of a number of biomolecules examined with optical or magnetic tweezers and discussed in this chapter.

There are many challenges and opportunities to meet in the coming decade. There is still a wide diversity of biomolecules and interactions to be characterized *in vitro* at the single-molecule level. With the rapidly growing commercial availability of biomolecules and new techniques to isolate and purify them, reproducibility and range of measurement will improve our understanding of molecular structure and dynamics. Controlled manipulation of intracellular organelles, membrane proteins, and cells themselves will open avenues for exploring systems biology at the single-cell level, linking with the ensemble methods currently used.

Table 2. Dimensions and persistence lengths of biopolymers.

	Length (nm)	Diameter (nm)	Persistence Length (nm)
Nucleic Acids			
dsDNA	$1 - 10^7$	2	50
ssDNA	$1 - 10^7$	1	0.75 – 3
dsRNA	$1 - 10^4$	2.6	60 – 75
ssRNA	$1 - 10^4$	1	3.5
Actin	$1 - 10^5$	5 – 7	15000
Microtubules	$1 - 10^4$	25	$1 - 8 \times 10^6$
Intermediate Filaments	$1 - 10^4$	10 – 12	300 – 1000
Proteins	$1 - 10^3$	0.5	
Titin	1200	2.5	1 – 9
Spectrin	200	6	5 – 20
Collagen	290	1.5	4.5 – 14
Fibrin	45	10	500
Myelin	53		0.5
Fibronectin	120 – 160		0.5
Polysaccharides			
Cellulose			5
Xyloglucan			6 – 8
Xanthan			120
Schizophyllan Polymers			180
Dextran, Sclerox, Alginate			1 – 20

Symbols used in this chapter:

- α is the relative complex polarizability
 κ is the viscosity of the surrounding medium (water is 10^{-3} s/m³)
 κ is the trap stiffness
 λ is the wavelength of incident light
 \mathbf{K} is the wave vector of the light $\left(k = \frac{2\pi}{\lambda}\right)$
 c is the speed of light in a vacuum ($\sim 3 \times 10^8$ m/s)
 σ is the optical scattering cross section (cm²)
 h is Planck's constant (6.6×10^{-34} Js)
 n_p is the particle refractive index
 n_m is the surrounding medium refractive index
 n_c is the refractive index contrast $\left(n_c = \frac{n_p}{n_m}\right)$
 r_p is the particle radius
 R is the reflectivity coefficient
 TF is the transmission coefficient
 T is the Maxwell stress tensor
 p is the electric dipole moment
 m is the magnetic dipole moment
 α is the complex polarizability
 B is the magnetic induction (Webers/m²)
 H is the external magnetic field strength (A/m)
 M is the magnetization (A/m)
 E is the electric field
 D is the electric field displacement
 ϵ_0 is the permittivity of free space (8.85×10^{-12} F/m)
 μ_0 is the permeability of free space ($4\pi \times 10^{-7}$ Wb A⁻¹ m⁻¹)
 χ_m is the magnetic susceptibility
 $\Delta\chi$ is the susceptibility contrast ($\Delta\chi = \chi_{particle} - \chi_{liquid}$)

Acknowledgements

RC acknowledges the support of a National Research Council Research Associateship Award, held at NINDS.

References

1. Crick, F. H. C.; Hughes, A. F. W., The physical properties of cytoplasm. *Experimental Cell Research* **1950**, (1), 37–80.
2. Ashkin, A., Acceleration and Trapping of Particles by Radiation Pressure. *Phys. Rev. Lett.* **24**, 156–159 (1970).
3. Lebedev, P. N., Experimental Examination of Light Pressure. *Annalen der Physik* **1901**, **6**, 433–458.
4. Ashkin, A.; Dziedzic, J. M.; Bjorkholm, J. E.; Chu, S., Observation of a Single-Beam Gradient Force Optical Trap for Dielectric Particles. *Optics Letters* **1986**, **11**, (5), 288–290.
5. Ashkin, A.; Dziedzic, J. M., Optical Trapping and Manipulation of Viruses and Bacteria. *Science* **1987**, **235**, (4795), 1517–1520.
6. Ashkin, A.; Dziedzic, J. M.; Yamane, T., Optical Trapping and Manipulation of Single Cells Using Infrared-Laser Beams. *Nature* **1987**, **330**, (6150), 769–771.
7. Burke, P. J., Encyclopedia of Nanoscience and Nanotechnology. American Scientific: Stevenson Ranch, CA, 2004; Vol. 6, p 623–641.
8. Markelz, A. G.; Roitberg, A.; Heilweil, E. J., Pulsed terahertz spectroscopy of DNA, bovine serum albumin and collagen between 0.1 and 2.0 THz. *Chemical Physics Letters* **2000**, **320**, (1–2), 42–48.

9. Naumann, D., *Encyclopedia of Analytical Chemistry*. John Wiley & Sons Ltd: Chichester, **2000**; p 102–131.
10. Buican, T. N.; Smyth, M. J.; Crissman, H. A.; Salzman, G. C.; Stewart, C. C.; Martin, J. C., Automated Single-Cell Manipulation and Sorting by Light Trapping. *Applied Optics* **1987**, 26, (24), 5311–5316.
11. Ashkin, A.; Dziedzic, J. M., Internal Cell Manipulation Using Infrared-Laser Traps. *Proceedings of the National Academy of Sciences of the United States of America* **1989**, 86, (20), 7914–7918.
12. Liang, H.; Wright, W. H.; Cheng, S.; He, W.; Berns, M. W., Micromanipulation of Chromosomes in Ptk2 Cells Using Laser Microsurgery (Optical Scalpel) in Combination with Laser-Induced Optical Force (Optical Tweezers). *Experimental Cell Research* **1993**, 204, (1), 110–120.
13. Yodh, A. G.; Lin, K. H.; Crocker, J. C.; Dinsmore, A. D.; Verma, R.; Kaplan, P. D., Entropically driven self-assembly and interaction in suspension. *Philosophical Transactions of the Royal Society of London Series a-Mathematical Physical and Engineering Sciences* **2001**, 359, (1782), 921–937.
14. Galajda, P.; Ormos, P., Complex micromachines produced and driven by light. *Applied Physics Letters* **2001**, 78, (2), 249–251.
15. Wang, G. M.; Seavick, E. M.; Mittag, E.; Searles, D. J.; Evans, D. J., Experimental demonstration of violations of the second law of thermodynamics for small systems and short time scales. *Physical Review Letters* **89**, (5): Art No. 050601 JUL 29 **2002**.
16. Crocker, J. C.; Grier, D. G., Microscopic measurement of the pair interaction potential of charge-stabilized colloid. *Physical Review Letters* **1994**, 73, (2), 352–355.
17. Molloy, J. E.; Padgett, M. J., Lights, action: optical tweezers. *Contemporary Physics* **2002**, 43, (4), 241–258.
18. Lang, M. J.; Block, S. M., Resource letter: LBOT-1: Laser-based optical tweezers. *American Journal of Physics* **2003**, 71, (3), 201–215.
19. Williams, M. C., Optical Tweezers: Measuring Piconewton Forces. In <http://www.biophysics.org/education/williams.pdf>: 1992.
20. Ashkin, A., Forces of a Single-Beam Gradient Laser Trap on a Dielectric Sphere in the Ray Optics Regime. *Biophysical Journal* **1992**, 61, (2), 569–582.
21. Svoboda, K.; Block, S. M., Biological Applications of Optical Forces. *Annual Review of Biophysics and Biomolecular Structure* **1994**, 23, 247–285.
22. Tlustý, T.; Meller, A.; Bar-Ziv, R., Optical gradient forces of strongly localized fields. *Physical Review Letters* **1998**, 81, (8), 1738–1741.
23. Cox, A. J.; DeWeerd, A. J.; Linden, J., An experiment to measure Mie and Rayleigh total scattering cross sections. *American Journal of Physics* **2002**, 70, (6), 620–625.
24. Smith, S. B.; Cui, Y.; Bustamante, C., Optical-trap force transducer that operates by direct measurement of light momentum. *Methods Enzymol* **2003**, 361, 134–62.
25. Conroy, R. S.; Mayers, B. T.; Vezenov, D. V.; Wolfe, D. B.; Prentiss, M. G.; Whitesides, G. M., Optical waveguiding in suspensions of dielectric particles. *Applied Optics* **2005**, 44, (36), 7853–7857.
26. Svoboda, K.; Block, S. M., Optical Trapping of Metallic Rayleigh Particles. *Optics Letters* **1994**, 19, (13), 930–932.
27. Stamper-Kurn, D. M.; Andrews, M. R.; Chikkatur, A. P.; Inouye, S.; Miesner, H. J.; Stenger, J.; Ketterle, W., Optical confinement of a Bose-Einstein condensate. *Physical Review Letters* **1998**, 80, (10), 2027–2030.
28. Nieminen, T. A.; Rubinsztein-Dunlop, H.; Heckenberg, N. R., Calculation and optical measurement of laser trapping forces on non-spherical particles. *Journal of Quantitative Spectroscopy & Radiative Transfer* **2001**, 70, (4–6), 627–637.
29. Harada, Y.; Asakura, T., Radiation forces on a dielectric sphere in the Rayleigh scattering regime. *Optics Communications* **1996**, 124, (5–6), 529–541.
30. Rohrbach, A.; Stelzer, E. H., Trapping forces, force constants, and potential depths for dielectric spheres in the presence of spherical aberrations. *Appl Opt* **2002**, 41, (13), 2494–507.
31. Pralle, A.; Florin, E. L.; Stelzer, E. H. K.; Horber, J. K. H., Localized diffusion measurements by 3D-SPT provide support for membrane microdomains. *Biophysical Journal* **1999**, 76, (1), A390–a390.
32. Guck, J.; Ananthakrishnan, R.; Mahmood, H.; Moon, T. J.; Cunningham, C. C.; Kas, J., The optical stretcher: A novel laser tool to micromanipulate cells. *Biophysical Journal* **2001**, 81, (2), 767–784.
33. Guck, J.; Schinkinger, S.; Lincoln, B.; Wottawah, F.; Ebert, S.; Romeyke, M.; Lenz, D.; Erickson, H. M.; Ananthakrishnan, R.; Mitchell, D.; Kas, J.; Ulvick, S.; Bilby, C., Optical deformability as an inherent cell marker for testing malignant transformation and metastatic competence. *Biophysical Journal* **2005**, 88, (5), 3689–3698.
34. Smith, S. B.; Cui, Y. J.; Bustamante, C., Overstretching B-DNA: The elastic response of individual double-stranded and single-stranded DNA molecules. *Science* **1996**, 271, (5250), 795–799.
35. Williams, M. C.; Wenner, J. R.; Rouzina, I.; Bloomfield, V. A., Entropy and heat capacity of DNA melting from temperature dependence of single molecule stretching. *Biophysical Journal* **2001**, 80, (4), 1932–1939.
36. Visscher, K.; Brakenhoff, G. J.; Krol, J. J., Micromanipulation by Multiple Optical Traps Created by a Single Fast Scanning Trap Integrated with the Bilateral Confocal Scanning Laser Microscope. *Cytometry* **1993**, 14, (2), 105–114.

37. Visscher, K.; Gross, S. P.; Block, S. M., Construction of multiple-beam optical traps with nanometer-resolution position sensing. *Ieee Journal of Selected Topics in Quantum Electronics* **1996**, 2, (4), 1066–1076.
38. Sasaki, K.; Koshioka, M.; Misawa, H.; Kitamura, N.; Masuhara, H., Pattern-Formation and Flow-Control of Fine Particles by Laser-Scanning Micromanipulation. *Optics Letters* **1991**, 16, (19), 1463–1465.
39. Dufresne, E. R.; Spalding, G. C.; Dearing, M. T.; Sheets, S. A.; Grier, D. G., Computer-generated holographic optical tweezer arrays. *Review of Scientific Instruments* **2001**, 72, (3), 1810–1816.
40. Liesener, J.; Reicherter, M.; Haist, T.; Tiziani, H. J., Multi-functional optical tweezers using computer-generated holograms. *Optics Communications* **2000**, 185, (1–3), 77–82.
41. Curtis, J. E.; Koss, B. A.; Grier, D. G., Dynamic holographic optical tweezers. *Optics Communications* **2002**, 207, (1–6), 169–175.
42. Sanford, J. L.; Greier, P. F.; Yang, K. H.; Lu, M.; Olyha, R. S.; Narayan, C.; Hoffnagle, J. A.; Alt, P. M.; Melcher, R. L., A one-megapixel reflective spatial light modulator system for holographic storage. *Ibm Journal of Research and Development* **1998**, 42, (3–4), 411–426.
43. Kawata, S.; Sugiura, T., Movement of Micrometer-Sized Particles in the Evanescent Field of a Laser-Beam. *Optics Letters* **1992**, 17, (11), 772–774.
44. Taylor, R. S.; Hnatovsky, C., Particle trapping in 3-D using a single fiber probe with an annular light distribution. *Optics Express* **2003**, 11, (21), 2775–2782.
45. Garces-Chavez, V.; Dholakia, K.; Spalding, G. C., Extended-area optically induced organization of microparticles on a surface. *Applied Physics Letters* **2005**, 86, (3), -.
46. Moothoo, D. N.; Arlt, J.; Conroy, R. S.; Akerboom, F.; Voit, A.; Dholakia, K., Beth's experiment using optical tweezers. *American Journal of Physics* 69, (3): 271–276 MAR **2001**.
47. Konig, K.; Liang, H.; Berns, M. W.; Tromberg, B. J., Cell damage in near-infrared multimode optical traps as a result of multiphoton absorption. *Optics Letters* **1996**, 21, (14), 1090–1092.
48. O'Neil, A. T.; Padgett, M. J., Three-dimensional optical confinement of micron-sized metal particles and the decoupling of the spin and orbital angular momentum within an optical spanner. *Optics Communications* **2000**, 185, (1–3), 139–143.
49. Rubinsztein-Dunlop, H.; Nieminen, T. A.; Friese, M. E. J.; Heckenberg, N. R., Optical trapping of absorbing particles. *Advances in Quantum Chemistry, Vol 30* **1998**, 30, 469–492.
50. Gahagan, K. T.; Swartzlander, G. A., Trapping of low-index microparticles in an optical vortex. *Journal of the Optical Society of America B-Optical Physics* **1998**, 15, (2), 524–534.
51. O'Neill, A. T.; Padgett, M. J., Axial and lateral trapping efficiency of Laguerre-Gaussian modes in inverted optical tweezers. *Optics Communications* **2001**, 193, (1–6), 45–50.
52. Allen, L.; Beijersbergen, M. W.; Spreeuw, R. J. C.; Woerdman, J. P., Orbital Angular-Momentum of Light and the Transformation of Laguerre-Gaussian Laser Modes. *Physical Review A* **1992**, 45, (11), 8185–8189.
53. Gahagan, K. T.; Swartzlander, G. A., Optical vortex trapping of particles. *Optics Letters* 1996, 21, (11), 827–829.
54. Simpson, N. B.; Allen, L.; Padgett, M. J., Optical tweezers and optical spanners with Laguerre-Gaussian modes. *Journal of Modern Optics* **1996**, 43, (12), 2485–2491.
55. Arlt, J.; Padgett, M. J., Generation of a beam with a dark focus surrounded by regions of higher intensity: the optical bottle beam. *Optics Letters* **2000**, 25, (4), 191–193.
56. Arlt, J.; Garces-Chavez, V.; Sibbett, W.; Dholakia, K., Optical micromanipulation using a Bessel light beam. *Optics Communications* **2001**, 197, (4–6), 239–245.
57. McGloin, D.; Dholakia, K., Bessel beams: diffraction in a new light. *Contemporary Physics* **2005**, 46, (1), 15–28.
58. Garces-Chavez, V.; McGloin, D.; Melville, H.; Sibbett, W.; Dholakia, K., Simultaneous micromanipulation in multiple planes using a self-reconstructing light beam. *Nature* **2002**, 419, (6903), 145–147.
59. Ke, P. C.; Gu, M., Characterization of trapping force on metallic Mie particles. *Applied Optics* **1999**, 38, (1), 160–167.
60. Plewa, J.; Tanner, E.; Mueth, D. M.; Grier, D. G., Processing carbon nanotubes with holographic optical tweezers. *Optics Express* **2004**, 12, (9), 1978–1981.
61. Gardel, M. L.; Valentine, M. T.; Weitz, D. A., *Microscale Diagnostic Techniques*. Springer-Verlag: Berlin, 2005.
62. *Advances in Biomagnetic Separation*. Eaton Publishing Company: Natick, 1994.
63. Shapiro, E. M.; Skrtic, S.; Sharer, K.; Hill, J. M.; Dunbar, C. E.; Koretsky, A. P., MRI detection of single particles for cellular imaging. *Proceedings of the National Academy of Sciences of the United States of America* **2004**, 101, (30), 10901–10906.
64. Bulte, J. W. M.; Kraitchman, D. L., Iron oxide MR contrast agents for molecular and cellular imaging. *Nmr in Biomedicine* **2004**, 17, (7), 484–499.
65. Berry, C. C.; Curtis, A. S. G., Functionalisation of magnetic nanoparticles for applications in biomedicine. *Journal of Physics D-Applied Physics* **2003**, 36, (13), R198–R206.

66. Takahashi, T.; Dimitrov, A. S.; Nagayama, K., Two-dimensional patterns of magnetic particles at air-water or glass-water interfaces induced by an external magnetic field: Theory and simulation of the formation process. *Journal of Physical Chemistry* **1996**, 100, (8), 3157–3162.
67. Assi, F.; Jenks, R.; Yang, J.; Love, C.; Prentiss, M., Massively parallel adhesion and reactivity measurements using simple and inexpensive magnetic tweezers. *Journal of Applied Physics* **2002**, 92, (9), 5584–5586.
68. Rife, J. C.; Miller, M. M.; Sheehan, P. E.; Tamanaha, C. R.; Tondra, M.; Whitman, L. J., Design and performance of GMR sensors for the detection of magnetic microbeads in biosensors. *Sensors and Actuators a-Physical* **2003**, 107, (3), 209–218.
69. Besse, P. A.; Boero, G.; Demierre, M.; Pott, V.; Popovic, R., Detection of a single magnetic microbead using a miniaturized silicon Hall sensor. *Applied Physics Letters* **2002**, 80, (22), 4199–4201.
70. Barbic, M., Magnetic wires in MEMS and bio-medical applications. *Journal of Magnetism and Magnetic Materials* **2002**, 249, (1–2), 357–367.
71. Kim, K. S.; Park, J. K., Magnetic force-based multiplexed immunoassay using superparamagnetic nanoparticles in microfluidic channel. *Lab on a Chip* **2005**, 5, (6), 657–664.
72. Romano, G.; Sacconi, L.; Capitanio, M.; Pavone, F. S., Force and torque measurements using magnetic micro beads for single molecule biophysics. *Optics Communications* **2003**, 215, (4–6), 323–331.
73. van der Heijden, T.; van Noort, J.; van Leest, H.; Kanaar, R.; Wyman, C.; Dekker, N.; Dekker, C., Torque-limited RecA polymerization on dsDNA. *Nucleic Acids Research* **2005**, 33, (7), 2099–2105.
74. Strick, T. R.; Charvin, G.; Dekker, N. H.; Allemand, J. F.; Bensimon, D.; Croquette, V., Tracking enzymatic steps of DNA topoisomerases using single-molecule micromanipulation. *Comptes Rendus Physique* **2002**, 3, (5), 595–618.
75. Charvin, G.; Allemand, J. F.; Strick, T. R.; Bensimon, D.; Croquette, V., Twisting DNA: single molecule studies. *Contemporary Physics* **2004**, 45, (5), 383–403.
76. Strick, T. R.; Allemand, J. F.; Bensimon, D.; Croquette, V., Behavior of supercoiled DNA. *Biophysical Journal* **1998**, 74, (4), 2016–2028.
77. Simson, D. A.; Ziemann, F.; Strigl, M.; Merkel, R., Micropipet-based pico force transducer: In depth analysis and experimental verification. *Biophysical Journal* **1998**, 74, (4), 2080–2088.
78. Haber, C.; Wirtz, D., Magnetic tweezers for DNA micromanipulation. *Review of Scientific Instruments* **2000**, 71, (12), 4561–4570.
79. Gosse, C.; Croquette, V., Magnetic tweezers: Micromanipulation and force measurement at the molecular level. *Biophysical Journal* **2002**, 82, (6), 3314–3329.
80. Strick, T.; Allemand, J. F. O.; Croquette, V.; Bensimon, D., The manipulation of single biomolecules. *Physics Today* **2001**, 54, (10), 46–51.
81. Matthews, B. D.; Overby, D. R.; Alenghat, F. J.; Karavitis, J.; Numaguchi, Y.; Allen, P. G.; Ingber, D. E., Mechanical properties of individual focal adhesions probed with a magnetic microneedle. *Biochemical and Biophysical Research Communications* **2004**, 313, (3), 758–764.
82. Meyer, A.; Hansen, D. B.; Gomes, C. S. G.; Hobbey, T. J.; Thomas, O. R. T.; Franzreb, M., Demonstration of a strategy for product purification by high-gradient magnetic fishing: Recovery of superoxide dismutase from unconditioned whey. *Biotechnology Progress* **2005**, 21, (1), 244–254.
83. Matthews, B. D.; LaVan, D. A.; Overby, D. R.; Karavitis, J.; Ingber, D. E., Electromagnetic needles with submicron pole tip radii for nanomanipulation of biomolecules and living cells. *Applied Physics Letters* **2004**, 85, (14), 2968–2970.
84. Mirowski, E.; Moreland, J.; Russek, S. E.; Donahue, M. J., Integrated microfluidic isolation platform for magnetic particle manipulation in biological systems. *Applied Physics Letters* **2004**, 84, (10), 1786–1788.
85. Vengalattore, M.; Conroy, R. S.; Rooijakkers, W.; Prentiss, M., Ferromagnets for integrated atom optics. *Journal of Applied Physics* **2004**, 95, (8), 4404–4407.
86. de Vries, A. H. B.; Krenn, B. E.; van Driel, R.; Kanger, J. S., Micro magnetic tweezers for nanomanipulation inside live cells. *Biophysical Journal* **2005**, 88, (3), 2137–2144.
87. Amblard, F.; Yurke, B.; Pargellis, A.; Leibler, S., A magnetic manipulator for studying local rheology and micromechanical properties of biological systems. *Review of Scientific Instruments* **1996**, 67, (3), 818–827.
88. Ziemann, F.; Radler, J.; Sackmann, E., Local Measurements of Viscoelastic Moduli of Entangled Actin Networks Using an Oscillating Magnetic Bead Micro-Rheometer. *Biophysical Journal* **1994**, 66, (6), 2210–2216.
89. Bausch, A. R.; Ziemann, F.; Boulbitch, A. A.; Jacobson, K.; Sackmann, E., Local measurements of viscoelastic parameters of adherent cell surfaces by magnetic bead microrheometry. *Biophysical Journal* **1998**, 75, (4), 2038–2049.
90. Bausch, A. R.; Moller, W.; Sackmann, E., Measurement of local viscoelasticity and forces in living cells by magnetic tweezers. *Biophysical Journal* **1999**, 76, (1), 573–579.
91. Bausch, A. R.; Hellerer, U.; Essler, M.; Aepfelbacher, M.; Sackmann, E., Rapid stiffening of integrin receptor-actin linkages in endothelial cells stimulated with thrombin: A magnetic bead microrheology study. *Biophysical Journal* **2001**, 80, (6), 2649–2657.

92. Moore, L. R.; Zborowski, M.; Nakamura, M.; McCloskey, K.; Gura, S.; Zuberi, M.; Margel, S.; Chalmers, J. J., The use of magnetite-doped polymeric microspheres in calibrating cell tracking velocimetry. *Journal of Biochemical and Biophysical Methods* **2000**, 44, (1–2), 115–130.
93. Todd, P.; Cooper, R. P.; Doyle, J. F.; Dunn, S.; Vellinger, J.; Deuser, M. S., Multistage magnetic particle separator. *Journal of Magnetism and Magnetic Materials* **2001**, 225, (1–2), 294–300.
94. Ghiringhelli, F.; Schmitt, E., Cellular and molecular purification processes based on the use of magnetic micro- and nanobeads. *Annales De Biologie Clinique* **2004**, 62, (1), 73–78.
95. Tibbe, A. G. J.; de Grooth, B. G.; Greve, J.; Liberti, P. A.; Dolan, G. J.; Terstappen, L. W. M. M., Optical tracking and detection of immunomagnetically selected and aligned cells. *Nature Biotechnology* **1999**, 17, (12), 1210–1213.
96. Zigeuner, R. E.; Riesenberger, R.; Pohla, H.; Hofstetter, A.; Oberneder, R., Isolation of circulating cancer cells from whole blood by immunomagnetic cell enrichment and unenriched immunocytochemistry in vitro. *Journal of Urology* **2003**, 169, (2), 701–705.
97. Morisada, S.; Miyata, N.; Iwahori, K., Immunomagnetic separation of scum-forming bacteria using polyclonal antibody that recognizes mycolic acids. *Journal of Microbiological Methods* **2002**, 51, (2), 141–148.
98. Mura, C. V.; Becker, M. L.; Orellana, A.; Wolff, D., Immunopurification of Golgi vesicles by magnetic sorting. *Journal of Immunological Methods* **2002**, 260, (1–2), 263–271.
99. Winkleman, A.; Gudiksen, K. L.; Ryan, D.; Whitesides, G. M.; Greenfield, D.; Prentiss, M., A magnetic trap for living cells suspended in a paramagnetic buffer. *Applied Physics Letters* **2004**, 85, (12), 2411–2413.
100. Simon, M. D.; Geim, A. K., Diamagnetic levitation: Flying frogs and floating magnets (invited). *Journal of Applied Physics* **2000**, 87, (9), 6200–6204.
101. Toussaint, R.; Akselvoll, J.; Helgesen, G.; Skjeltorp, A. T.; Flekkoy, E. G., Interaction model for magnetic holes in a ferrofluid layer. *Physical Review* 69, (1): Art No. 011407 Part 1 JAN **2004**.
102. Lyuksyutov, I. F.; Lyuksyutova, A.; Naugle, D. G.; Rathnayaka, K. D. D., Trapping microparticles with strongly inhomogeneous magnetic fields. *Modern Physics Letters B* **2003**, 17, (17), 935–940.
103. Lecommandoux, S. B.; Sandre, O.; Checot, F.; Rodriguez-Hernandez, J.; Perzynski, R., Magnetic nanocomposite micelles and vesicles. *Advanced Materials* **2005**, 17, (6), 712–+.
104. Gatteschi, D.; Caneschi, A.; Pardi, L.; Sessoli, R., Large Clusters of Metal-Ions - the Transition from Molecular to Bulk Magnets. *Science* **1994**, 265, (5175), 1054–1058.
105. Genç, S. Synthesis and Properties of Magnetorheological (MR) Fluids. University of Pittsburgh, Pittsburgh, **2002**.
106. Hatch, A.; Kamholz, A. E.; Holman, G.; Yager, P.; Bohringer, K. F., A ferrofluidic magnetic micropump. *Journal of Microelectromechanical Systems* **2001**, 10, (2), 215–221.
107. Smith, S. P.; Bhalotra, S. R.; Brody, A. L.; Brown, B. L.; Boyda, E. K.; Prentiss, M., Inexpensive optical tweezers for undergraduate laboratories. *American Journal of Physics* **1999**, 67, (1), 26–35.
108. Laser Tweezers in Cell Biology. Academic Press: San Diego, 1998.
109. Bechhoefer, J.; Wilson, S., Faster, cheaper, safer optical tweezers for the undergraduate laboratory. *American Journal of Physics* **2002**, 70, (4), 393–400.
110. Neuman, K. C.; Block, S. M., Optical trapping. *Review of Scientific Instruments* **2004**, 75, (9), 2787–2809.
111. Schmidt, T.; Schutz, G. J.; Baumgartner, W.; Gruber, H. J.; Schindler, H., Imaging of single molecule diffusion. *Proceedings of the National Academy of Sciences of the United States of America* **1996**, 93, (7), 2926–2929.
112. Thompson, R. E.; Larson, D. R.; Webb, W. W., Precise nanometer localization analysis for individual fluorescent probes. *Biophysical Journal* **2002**, 82, (5), 2775–2783.
113. Ghislain, L. P.; Switz, N. A.; Webb, W. W., Measurement of Small Forces Using an Optical Trap. *Review of Scientific Instruments* **1994**, 65, (9), 2762–2768.
114. Jonas, A.; Zemanek, P.; Florin, E. L., Single-beam trapping in front of reflective surfaces. *Optics Letters* **2001**, 26, (19), 1466–1468.
115. Clapp, A. R.; Ruta, A. G.; Dickinson, R. B., Three-dimensional optical trapping and evanescent wave light scattering for direct measurement of long range forces between a colloidal particle and a surface. *Review of Scientific Instruments* **1999**, 70, (6), 2627–2636.
116. Rohrbach, A.; Kress, H.; Stelzer, E. H. K., Three-dimensional tracking of small spheres in focused laser beams: influence of the detection angular aperture. *Optics Letters* **2003**, 28, (6), 411–413.
117. Svoboda, K.; Schmidt, C. F.; Schnapp, B. J.; Block, S. M., Direct Observation of Kinesin Stepping by Optical Trapping Interferometry. *Nature* **1993**, 365, (6448), 721–727.
118. Gittes, F.; Schmidt, C. F., Interference model for back-focal-plane displacement detection in optical tweezers. *Optics Letters* **1998**, 23, (1), 7–9.
119. Visscher, K.; Block, S. M., Versatile optical traps with feedback control. *Methods Enzymol* **1998**, 298, 460–89.
120. Rice, S. E.; Purcell, T. J.; Spudich, J. A., Building and using optical traps to study properties of molecular motors. *Biophotonics, Pt B* **2003**, 361, 112–133.

121. Ashkin, A.; Dziedzic, J. M., Optical Trapping and Manipulation of Single Living Cells Using Infrared-Laser Beams. *Berichte Der Bunsen-Gesellschaft-Physical Chemistry Chemical Physics* **1989**, 93, (3), 254–260.
122. Liu, Y.; Sonek, G. J.; Berns, M. W.; Tromberg, B. J., Physiological monitoring of optically trapped cells: Assessing the effects of confinement by 1064-nm laser tweezers using microfluorometry. *Biophysical Journal* **1996**, 71, (4), 2158–2167.
123. Neuman, K. C.; Chadd, E. H.; Liou, G. F.; Bergman, K.; Block, S. M., Characterization of photodamage to *Escherichia coli* in optical traps. *Biophysical Journal* **1999**, 77, (5), 2856–2863.
124. Wuite, G. J. L.; Davenport, R. J.; Rappaport, A.; Bustamante, C., An integrated laser trap/flow control video microscope for the study of single biomolecules. *Biophysical Journal* **2000**, 79, (2), 1155–1167.
125. Schmitt, K. E. Optical neuronal guiding on the hypothalamic GnRH cell line GT1. The University of Texas at Austin, Austin, **2003**.
126. Liu, Y.; Cheng, D. K.; Sonek, G. J.; Berns, M. W.; Chapman, C. F.; Tromberg, B. J., Evidence for Localized Cell Heating Induced by Infrared Optical Tweezers. *Biophysical Journal* **1995**, 68, (5), 2137–2144.
127. Berns, M. W.; Aist, J. R.; Wright, W. H.; Liang, H., Optical Trapping in Animal and Fungal Cells Using a Tunable, near-Infrared Titanium-Sapphire Laser. *Experimental Cell Research* **1992**, 198, (2), 375–378.
128. Underhill, P. T.; Doyle, P. S., Development of bead-spring polymer models using the constant extension ensemble. *Journal of Rheology* **2005**, 49, (5), 963–987.
129. Evans, E.; Ritchie, K., Dynamic strength of molecular adhesion bonds. *Biophysical Journal* **1997**, 72, (4), 1541–1555.
130. Molloy, J. E.; Burns, J. E.; Kendrickjones, J.; Tregear, R. T.; White, D. C. S., Movement and Force Produced by a Single Myosin Head. *Nature* **1995**, 378, (6553), 209–212.
131. Wright, W. H.; Sonek, G. J.; Berns, M. W., Parametric Study of the Forces on Microspheres Held by Optical Tweezers. *Applied Optics* **1994**, 33, (9), 1735–1748.
132. Pankhurst, Q. A.; Connolly, J.; Jones, S. K.; Dobson, J., Applications of magnetic nanoparticles in biomedicine. *Journal of Physics D-Applied Physics* **2003**, 36, (13), R167–R181.
133. Wang, M. D.; Yin, H.; Landick, R.; Gelles, J.; Block, S. M., Stretching DNA with optical tweezers. *Biophysical Journal* **1997**, 72, (3), 1335–1346.
134. Noji, H.; Yasuda, R.; Yoshida, M.; Kinosita, K., Direct observation of the rotation of F-1-ATPase. *Nature* **1997**, 386, (6622), 299–302.
135. Guthold, M.; Mullin, J.; Lord, S.; Superfine, R.; Taylor, R.; Erie, D., Investigating the mechanical properties of individual fibrin fibers with the nanomanipulator AFM. *Biophysical Journal* **2001**, 80, (1), 307A–307A.
136. Dammer, U.; Popescu, O.; Wagner, P.; Anselmetti, D.; Guntherodt, H. J.; Misevic, G. N., Binding Strength between Cell-Adhesion Proteoglycans Measured by Atomic-Force Microscopy. *Science* **1995**, 267, (5201), 1173–1175.
137. Piran, U.; Riordan, W. J., Dissociation Rate-Constant of the Biotin-Streptavidin Complex. *Journal of Immunological Methods* **1990**, 133, (1), 141–143.
138. Merkel, R.; Nassoy, P.; Leung, A.; Ritchie, K.; Evans, E., Energy landscapes of receptor-ligand bonds explored with dynamic force spectroscopy. *Nature* **1999**, 397, (6714), 50–53.
139. Yuan, C. B.; Chen, A.; Kolb, P.; Moy, V. T., Energy landscape of streptavidin-biotin complexes measured by atomic force microscopy. *Biochemistry* **2000**, 39, (33), 10219–10223.
140. Danilowicz, C.; Greenfield, D.; Prentiss, M., Dissociation of ligand-receptor complexes using magnetic tweezers. *Analytical Chemistry* **2005**, 77, (10), 3023–3028.
141. Helmerson, K.; Kishore, R.; Phillips, W. D.; Weetall, H. H., Optical tweezers-based immunosensor detects femtomolar concentrations of antigens. *Clinical Chemistry* **1997**, 43, (2), 379–383.
142. Kulin, S.; Kishore, R.; Hubbard, J. B.; Helmerson, K., Real-time measurement of spontaneous antigen-antibody dissociation. *Biophysical Journal* **2002**, 83, (4), 1965–1973.
143. Round, A. N.; Berry, M.; McMaster, T. J.; Stoll, S.; Gowers, D.; Corfield, A. P.; Miles, M. J., Heterogeneity and persistence length in human ocular mucins. *Biophysical Journal* **2002**, 83, (3), 1661–1670.
144. Sagis, L. M. C.; Veerman, C.; van der Linden, E., Mesoscopic properties of semiflexible amyloid fibrils. *Langmuir* **2004**, 20, (3), 924–927.
145. Smith, S. B.; Finzi, L.; Bustamante, C., Direct Mechanical Measurements of the Elasticity of Single DNA-Molecules by Using Magnetic Beads. *Science* **1992**, 258, (5085), 1122–1126.
146. Leger, J. F.; Romano, G.; Sarkar, A.; Robert, J.; Bourdieu, L.; Chatenay, D.; Marko, J. F., Structural transitions of a twisted and stretched DNA molecule. *Physical Review Letters* **1999**, 83, (5), 1066–1069.
147. Allemand, J. F.; Bensimon, D.; Croquette, V., Stretching DNA and RNA to probe their interactions with proteins. *Current Opinion in Structural Biology* **2003**, 13, (3), 266–274.
148. Tinland, B.; Pluen, A.; Sturm, J.; Weill, G., Persistence length of single-stranded DNA. *Macromolecules* **1997**, 30, (19), 5763–5765.

149. Bustamante, C.; Smith, S. B.; Liphardt, J.; Smith, D., Single-molecule studies of DNA mechanics. *Current Opinion in Structural Biology* **2000**, 10, (3), 279–285.
150. Conroy, R. S.; Danilowicz, C., Unravelling DNA. *Contemporary Physics* **2004**, 45, (4), 277–302.
151. Bockelmann, U., Single-molecule manipulation of nucleic acids. *Current Opinion in Structural Biology* **2004**, 14, (3), 368–373.
152. Bustamante, C.; Bryant, Z.; Smith, S. B., Ten years of tension: single-molecule DNA mechanics. *Nature* **2003**, 421, (6921), 423–427.
153. Marko, J.; Propperova, A., Environmental Monitoring within the Slovak Republic. *Environmental Monitoring and Assessment* **1995**, 34, (2), 131–136.
154. Strick, T. R.; Bensimon, D.; Croquette, V., Micro-mechanical measurement of the torsional modulus of DNA. *Genetica* **1999**, 106, (1–2), 57–62.
155. Bryant, Z.; Stone, M. D.; Gore, J.; Smith, S. B.; Cozzarelli, N. R.; Bustamante, C., Structural transitions and elasticity from torque measurements on DNA. *Nature* **2003**, 424, (6946), 338–341.
156. Charvin, G.; Vologodskii, A.; Bensimon, D.; Croquette, V., Braiding DNA: Experiments, simulations, and models. *Biophysical Journal* **2005**, 88, (6), 4124–4136.
157. Revyakin, A.; Ebricht, R. H.; Strick, T. R., Single-molecule DNA nanomanipulation: Improved resolution through use of shorter DNA fragments. *Nature Methods* **2005**, 2, (2), 127–138.
158. Bockelmann, U.; Thomen, P.; Essevaz-Roulet, B.; Viasnoff, V.; Heslot, F., Unzipping DNA with optical tweezers: high sequence sensitivity and force flips. *Biophysical Journal* **2002**, 82, (3), 1537–1553.
159. Danilowicz, C.; Coljee, V. W.; Bouzigues, C.; Lubensky, D. K.; Nelson, D. R.; Prentiss, M., DNA unzipped under a constant force exhibits multiple metastable intermediates. *Proceedings of the National Academy of Sciences of the United States of America* **2003**, 100, (4), 1694–1699.
160. Danilowicz, C.; Conroy, R.; Kafri, Y.; Coljee, V.; Prentiss, M., Measurement of the phase diagram of DNA unzipping in the temperature-force plane. *Physical Review Letters* **2004**, 93, (7), 078101.
161. Vorobjev, I. A.; Hong, L.; Wright, W. H.; Berns, M. W., Optical Trapping for Chromosome Manipulation - a Wavelength Dependence of Induced Chromosome Bridges. *Biophysical Journal* **1993**, 64, (2), 533–538.
162. Bennink, M. L.; Leuba, S. H.; Leno, G. H.; Zlatanova, J.; de Grooth, B. G.; Greve, J., Unfolding individual nucleosomes by stretching single chromatin fibers with optical tweezers. *Nature Structural Biology* **2001**, 8, (7), 606–610.
163. Brower-Toland, B. D.; Smith, C. L.; Yeh, R. C.; Lis, J. T.; Peterson, C. L.; Wang, M. D., Mechanical disruption of individual nucleosomes reveals a reversible multistage release of DNA. *Proceedings of the National Academy of Sciences of the United States of America* **2002**, 99, (4), 1960–1965.
164. Storz, G., An expanding universe of noncoding RNAs. *Science* **2002**, 296, (5571), 1260–1263.
165. Hagerman, P. J., Flexibility of RNA. *Annual Review of Biophysics and Biomolecular Structure* **1997**, 26, 139–156.
166. Abels, J. A.; Moreno-Herrero, F.; van der Heijden, T.; Dekker, C.; Dekker, N. H., Single-molecule measurements of the persistence length of double-stranded RNA. *Biophysical Journal* **2005**, 88, (4), 2737–2744.
167. Ha, T.; Zhuang, X. W.; Kim, H. D.; Orr, J. W.; Williamson, J. R.; Chu, S., Ligand-induced conformational changes observed in single RNA molecules. *Proceedings of the National Academy of Sciences of the United States of America* **1999**, 96, (16), 9077–9082.
168. Zhuang, X. W., Single-molecule RNA science. *Annual Review of Biophysics and Biomolecular Structure* **2005**, 34, 399–414.
169. Liphardt, J.; Onoa, B.; Smith, S. B.; Tinoco, I.; Bustamante, C., Reversible unfolding of single RNA molecules by mechanical force. *Science* **2001**, 292, (5517), 733–737.
170. Onoa, B.; Dumont, S.; Liphardt, J.; Smith, S. B.; Tinoco, I.; Bustamante, C., Identifying kinetic barriers to mechanical unfolding of the T-thermophila ribozyme. *Science* **2003**, 299, (5614), 1892–1895.
171. Ott, A.; Magnasco, M.; Simon, A.; Libchaber, A., Measurement of the Persistence Length of Polymerized Actin Using Fluorescence Microscopy. *Physical Review E* **1993**, 48, (3), R1642–R1645.
172. Tsuda, Y.; Yasutake, H.; Ishijima, A.; Yanagida, T., Torsional rigidity of single actin filaments and actin-actin bond breaking force under torsion measured directly by in vitro micromanipulation. *Proceedings of the National Academy of Sciences of the United States of America* **1996**, 93, (23), 12937–12942.
173. Amblard, F.; Maggs, A. C.; Yurke, B.; Pargellis, A. N.; Leibler, S., Subdiffusion and anomalous local viscoelasticity in actin networks. *Physical Review Letters* **1996**, 77, (21), 4470–4473.
174. Arai, Y.; Yasuda, R.; Akashi, K.; Harada, Y.; Miyata, H.; Kinoshita, K.; Itoh, H., Tying a molecular knot with optical tweezers. *Nature* **1999**, 399, (6735), 446–448.
175. Kurachi, M.; Hoshi, M.; Tashiro, H., Buckling of a Single Microtubule by Optical Trapping Forces - Direct Measurement of Microtubule Rigidity. *Cell Motility and the Cytoskeleton* **1995**, 30, (3), 221–228.
176. Felgner, H.; Frank, R.; Schliwa, M., Flexural rigidity of microtubules measured with the use of optical tweezers. *Journal of Cell Science* **1996**, 109, 509–516.

177. Gittes, F.; Mickey, B.; Nettleton, J.; Howard, J., Flexural Rigidity of Microtubules and Actin-Filaments Measured from Thermal Fluctuations in Shape. *Journal of Cell Biology* **1993**, 120, (4), 923–934.
178. Janson, M. E.; Dogterom, M., A bending mode analysis for growing microtubules: Evidence for a velocity-dependent rigidity. *Biophysical Journal* **2004**, 87, (4), 2723–2736.
179. Tolic-Norrelykke, I. M.; Sacconi, L.; Stringari, C.; Raabe, I.; Pavone, F. S., Nuclear and division-plane positioning revealed by optical micromanipulation. *Current Biology* **2005**, 15, (13), 1212–1216.
180. Mucke, N.; Kreplak, L.; Kirmse, R.; Wedig, T.; Herrmann, H.; Aebi, U.; Langowski, J., Assessing the flexibility of intermediate filaments by atomic force microscopy. *Journal of Molecular Biology* **2004**, 335, (5), 1241–1250.
181. Wang, N.; Stamenovic, D., Contribution of intermediate filaments to cell stiffness, stiffening, and growth. *American Journal of Physiology-Cell Physiology* **2000**, 279, (1), C188–C194.
182. Bright, J. N.; Hoh, J. H.; Woolf, T. B., Computational investigation of confined unstructured proteins. *Biophysical Journal* **2001**, 80, (1), 407A–408A.
183. Kellermayer, M. S. Z., Visualizing and manipulating individual protein molecules. *Physiological Measurement* **2005**, 26, (4), R119–R153.
184. Rief, M.; Gautel, M.; Oesterhelt, F.; Fernandez, J. M.; Gaub, H. E., Reversible unfolding of individual titin immunoglobulin domains by AFM. *Science* **1997**, 276, (5315), 1109–1112.
185. Tskhovrebova, L.; Trinick, J.; Sleep, J. A.; Simmons, R. M., Elasticity and unfolding of single molecules of the giant muscle protein titin. *Nature* **1997**, 387, (6630), 308–312.
186. Kellermayer, M. S. Z.; Smith, S. B.; Bustamante, C.; Granzier, H. L., Complete unfolding of the titin molecule under external force. *Journal of Structural Biology* **1998**, 122, (1–2), 197–205.
187. Kellermayer, M. S. Z.; Smith, S. B.; Bustamante, C.; Granzier, H. L., Mechanical fatigue in repetitively stretched single molecules of titin. *Biophysical Journal* **2001**, 80, (2), 852–863.
188. Svoboda, K.; Schmidt, C. F.; Branton, D.; Block, S. M., Conformation and Elasticity of the Isolated Red-Blood-Cell Membrane Skeleton. *Biophysical Journal* **1992**, 63, (3), 784–793.
189. Li, J.; Dao, M.; Lim, C. T.; Suresh, S., Spectrin-level modeling of the cytoskeleton and optical tweezers stretching of the erythrocyte. *Biophysical Journal* **2005**, 88, (5), 3707–3719.
190. Luo, Z. P.; Bolander, M. E.; An, K. N., A method for determination of stiffness of collagen molecules. *Biochemical and Biophysical Research Communications* **1997**, 232, (1), 251–254.
191. Sun, Y. L.; Luo, Z. P.; An, K. N., Stretching short biopolymers using optical tweezers. *Biochemical and Biophysical Research Communications* **2001**, 286, (4), 826–830.
192. Luo, Z. P.; Sun, Y. L.; Fujii, T.; An, K. N., Single molecule mechanical properties of type II collagen and hyaluronan measured by optical tweezers. *Biorheology* **2004**, 41, (3–4), 247–254.
193. Oesterhelt, F.; Oesterhelt, D.; Pfeiffer, M.; Engel, A.; Gaub, H. E.; Muller, D. J., Unfolding pathways of individual bacteriorhodopsins. *Science* **2000**, 288, (5463), 143–146.
194. Storm, C.; Pastore, J. J.; MacKintosh, F. C.; Lubensky, T. C.; Janmey, P. A., Nonlinear elasticity in biological gels. *Nature* **2005**, 435, (7039), 191–194.
195. Mueller, H.; Butt, H. J.; Bamberg, E., Force measurements on myelin basic protein adsorbed to mica and lipid bilayer surfaces done with the atomic force microscope. *Biophysical Journal* **1999**, 76, (2), 1072–1079.
196. Krigbaum, W. R.; Hsu, T. S., Molecular-Conformation of Bovine α -1 Basic-Protein, a Coiling Macromolecule in Aqueous-Solution. *Biochemistry* **1975**, 14, (11), 2542–2546.
197. Oberdorfer, Y.; Schrot, S.; Fuchs, H.; Galinski, E.; Janshoff, A., Impact of compatible solutes on the mechanical properties of fibronectin: a single molecule analysis. *Physical Chemistry Chemical Physics* **2003**, 5, (9), 1876–1881.
198. Sharon, N.; Lis, H., Carbohydrates in Cell Recognition. *Scientific American* **1993**, 268, (1), 82–89.
199. Picout, D. R.; Ross-Murphy, S. B.; Errington, N.; Harding, S. E., Pressure cell assisted solubilization of xyloglucans: Tamarind seed polysaccharide and detarium gum. *Biomacromolecules* **2003**, 4, (3), 799–807.
200. Sletmoen, M.; Maurstad, G.; Sikorski, P.; Paulsen, B. S.; Stokke, B. T., Characterisation of bacterial polysaccharides: steps towards single-molecular studies. *Carbohydrate Research* **2003**, 338, (23), 2459–2475.
201. Rief, M.; Oesterhelt, F.; Heymann, B.; Gaub, H. E., Single molecule force spectroscopy on polysaccharides by atomic force microscopy. *Science* **1997**, 275, (5304), 1295–1297.
202. Janicijevic, A.; Ristic, D.; Wyman, C., The molecular machines of DNA repair: scanning force microscopy analysis of their architecture. *Journal of Microscopy-Oxford* **2003**, 212, 264–272.
203. Dong, C.; So, P. T. C.; Mahadevan, L.; Kaizuka, Y.; Sutin, J. D.; Graton, E., Control of exonuclease digestion activities by microscopic mechanical forces. *Biophysical Journal* **1999**, 76, (1), A132–a132.
204. van Oijen, A. M.; Blainey, P. C.; Crampton, D. J.; Richardson, C. C.; Ellenberger, T.; Xie, X. S., Single-molecule kinetics of lambda exonuclease reveal base dependence and dynamic disorder. *Science* **2003**, 301, (5637), 1235–1238.

205. Perkins, T. T.; Dalal, R. V.; Mitsis, P. G.; Block, S. M., Sequence-dependent pausing of single lambda exonuclease molecules. *Science* **2003**, 301, (5641), 1914–1918.
206. Werner, J. H.; Cai, H.; Keller, R. A.; Goodwin, P. M., Exonuclease I hydrolyzes DNA with a distribution of rates. *Biophysical Journal* **2005**, 88, (2), 1403–1412.
207. Yin, H.; Wang, M. D.; Svoboda, K.; Landick, R.; Block, S. M.; Gelles, J., Transcription against an Applied Force. *Science* **1995**, 270, (5242), 1653–1657.
208. Wuite, G. J. L.; Smith, S. B.; Young, M.; Keller, D.; Bustamante, C., Single-molecule studies of the effect of template tension on T7 DNA polymerase activity. *Nature* **2000**, 404, (6773), 103–106.
209. Thomen, P.; Lopez, P. J.; Heslot, F., Unravelling the mechanism of RNA-polymerase forward motion by using mechanical force. *Physical Review Letters* **2005**, 94, (12), -.
210. Wang, M. D.; Schnitzer, M. J.; Yin, H.; Landick, R.; Gelles, J.; Block, S. M., Force and velocity measured for single molecules of RNA polymerase. *Science* **1998**, 282, (5390), 902–907.
211. Skinner, G. M.; Baumann, C. G.; Quinn, D. M.; Molloy, J. E.; Hoggett, J. G., Promoter binding, initiation, and elongation by bacteriophage T7 RNA polymerase - A single-molecule view of the transcription cycle. *Journal of Biological Chemistry* **2004**, 279, (5), 3239–3244.
212. Wang, H. Y.; Elston, T.; Mogilner, A.; Oster, G., Force generation in RNA polymerase. *Biophysical Journal* **1998**, 74, (3), 1186–1202.
213. Forde, N. R.; Izhaky, D.; Woodcock, G. R.; Wuite, G. J. L.; Bustamante, C., Using mechanical force to probe the mechanism of pausing and arrest during continuous elongation by Escherichia coli RNA polymerase. *Proceedings of the National Academy of Sciences of the United States of America* **2002**, 99, (18), 11682–11687.
214. Waksman, G.; Lanka, E.; Carazo, J. M., Helicases as nucleic acid unwinding machines. *Nature Structural Biology* **2000**, 7, (1), 20–22.
215. Bianco, P. R.; Brewer, L. R.; Corzett, M.; Balhorn, R.; Yeh, Y.; Kowalczykowski, S. C.; Baskin, R. J., Processive translocation and DNA unwinding by individual RecBCD enzyme molecules. *Nature* **2001**, 409, (6818), 374–378.
216. Perkins, T. T.; Li, H. W.; Dalal, R. V.; Gelles, J.; Block, S. M., Forward and reverse motion of single RecBCD molecules on DNA. *Biophysical Journal* **2004**, 86, (3), 1640–1648.
217. Dawid, A.; Croquette, V.; Grigoriev, M.; Heslot, F., Single-molecule study of RuvAB-mediated Holliday-junction migration. *Proceedings of the National Academy of Sciences of the United States of America* **2004**, 101, (32), 11611–11616.
218. Amit, R.; Gileadi, O.; Stavans, J., Direct observation of RuvAB-catalyzed branch migration of single Holliday junctions. *Proceedings of the National Academy of Sciences of the United States of America* **2004**, 101, (32), 11605–11610.
219. Dessinges, M. N.; Lionnet, T.; Xi, X. G.; Bensimon, D.; Croquette, V., Single-molecule assay reveals strand switching and enhanced processivity of UvrD. *Proceedings of the National Academy of Sciences of the United States of America* **2004**, 101, (17), 6439–6444.
220. Champoux, J. J., DNA topoisomerases: Structure, function, and mechanism. *Annual Review of Biochemistry* **2001**, 70, 369–413.
221. Charvin, G.; Strick, T. R.; Bensimon, D.; Croquette, V., Tracking topoisomerase activity at the single-molecule level. *Annual Review of Biophysics and Biomolecular Structure* **2005**, 34, 201–219.
222. Dekker, N. H.; Rybenkov, V. V.; Dugué, M.; Crisona, N. J.; Cozzarelli, N. R.; Bensimon, D.; Croquette, V., The mechanism of type IA topoisomerases. *Proceedings of the National Academy of Sciences of the United States of America* **2002**, 99, (19), 12126–12131.
223. Koster, D. A.; Croquette, V.; Dekker, C.; Shuman, S.; Dekker, N. H., Friction and torque govern the relaxation of DNA supercoils by eukaryotic topoisomerase IB. *Nature* **2005**, 434, (7033), 671–674.
224. Strick, T. R.; Croquette, V.; Bensimon, D., Single-molecule analysis of DNA uncoiling by a type II topoisomerase. *Nature* **2000**, 404, (6780), 901–904.
225. Charvin, G.; Bensimon, D.; Croquette, V., Single-molecule study of DNA unlinking by eukaryotic and prokaryotic type-II topoisomerases. *Proceedings of the National Academy of Sciences of the United States of America* **2003**, 100, (17), 9820–9825.
226. Crisona, N. J.; Strick, T. R.; Bensimon, D.; Croquette, V.; Cozzarelli, N. R., Preferential relaxation of positively supercoiled DNA by E-coli topoisomerase IV in single-molecule and ensemble measurements. *Genes & Development* **2000**, 14, (22), 2881–2892.
227. Smith, D. E.; Tans, S. J.; Smith, S. B.; Grimes, S.; Anderson, D. L.; Bustamante, C., The bacteriophage phi 29 portal motor can package DNA against a large internal force. *Nature* **2001**, 413, (6857), 748–752.
228. Sabbert, D.; Engelbrecht, S.; Junge, W., Functional and idling rotatory motion within F-1-ATPase. *Proceedings of the National Academy of Sciences of the United States of America* **1997**, 94, (9), 4401–4405.
229. Yasuda, R.; Noji, H.; Kinosita, K.; Yoshida, M., F-1-ATPase is a highly efficient molecular motor that rotates with discrete 120 degrees steps. *Cell* **1998**, 93, (7), 1117–1124.

230. Itoh, H.; Takahashi, A.; Adachi, K.; Noji, H.; Yasuda, R.; Yoshida, M.; Kinosita, K., Mechanically driven ATP synthesis by F₁-ATPase. *Nature* **2004**, 427, (6973), 465–468.
231. Ueno, H.; Suzuki, T.; Kinosita, K.; Yoshida, M., ATP-driven stepwise rotation of FOF₁-ATP synthase. *Proceedings of the National Academy of Sciences of the United States of America* **2005**, 102, (5), 1333–1338.
232. Kull, F. J.; Sablin, E. P.; Lau, R.; Fletterick, R. J.; Vale, R. D., Crystal structure of the kinesin motor domain reveals a structural similarity to myosin. *Nature* **1996**, 380, (6574), 550–555.
233. Finer, J. T.; Simmons, R. M.; Spudich, J. A., Single Myosin Molecule Mechanics - Piconewton Forces and Nanometer Steps. *Nature* **1994**, 368, (6467), 113–119.
234. Mehta, A. D.; Finer, J. T.; Spudich, J. A., Detection of single-molecule interactions using correlated thermal diffusion. *Proceedings of the National Academy of Sciences of the United States of America* **1997**, 94, (15), 7927–7931.
235. Ishijima, A.; Kojima, H.; Higuchi, H.; Harada, Y.; Funatsu, T.; Yanagida, T., Multiple- and single-molecule analysis of the actomyosin motor by nanometer piconewton manipulation with a microneedle: Unitary steps and forces. *Biophysical Journal* **1996**, 70, (1), 383–400.
236. Tanaka, H.; Ishijima, A.; Honda, M.; Saito, K.; Yanagida, T., Orientation dependence of displacements by a single one-headed myosin relative to the actin filament. *Biophysical Journal* **1998**, 75, (4), 1886–1894.
237. Geeves, M. A.; Holmes, K. C., Structural mechanism of muscle contraction. *Annual Review of Biochemistry* **1999**, 68, 687–728.
238. Vale, R. D., Myosin V motor proteins: marching stepwise towards a mechanism. *Journal of Cell Biology* **2003**, 163, (3), 445–450.
239. Schott, D. H.; Collins, R. N.; Bretscher, A., Secretory vesicle transport velocity in living cells depends on the myosin-V lever arm length. *Journal of Cell Biology* **2002**, 156, (1), 35–39.
240. Rief, M.; Rock, R. S.; Mehta, A. D.; Mooseker, M. S.; Cheney, R. E.; Spudich, J. A., Myosin-V stepping kinetics: A molecular model for processivity. *Proceedings of the National Academy of Sciences of the United States of America* **2000**, 97, (17), 9482–9486.
241. Yildiz, A.; Forkey, J. N.; McKinney, S. A.; Ha, T.; Goldman, Y. E.; Selvin, P. R., Myosin V walks hand-over-hand: Single fluorophore imaging with 1.5-nm localization. *Science* **2003**, 300, (5628), 2061–2065.
242. Snyder, G. E.; Sakamoto, T.; Hammer, J. A.; Sellers, J. R.; Selvin, P. R., Nanometer localization of single green fluorescent proteins: Evidence that myosin V walks hand-over-hand via telemark configuration. *Biophysical Journal* **2004**, 87, (3), 1776–1783.
243. Warshaw, D. M.; Kennedy, G. G.; Work, S. S.; Kremntsova, E. B.; Beck, S.; Trybus, K. M., Differential Labeling of myosin V heads with quantum dots allows direct visualization of hand-over-hand processivity. *Biophysical Journal* **2005**, 88, (5), L30–L32.
244. Rock, R. S.; Ramamurthy, B.; Dunn, A. R.; Beccafico, S.; Rami, B. R.; Morris, C.; Spink, B. J.; Franzini-Armstrong, C.; Spudich, J. A.; Sweeney, H. L., A flexible domain is essential for the large step size and processivity of myosin VI. *Molecular Cell* **2005**, 17, (4), 603–609.
245. Veigel, C.; Coluccio, L. M.; Jontes, J. D.; Sparrow, J. C.; Milligan, R. A.; Molloy, J. E., The motor protein myosin-I produces its working stroke in two steps. *Nature* **1999**, 398, (6727), 530–533.
246. Tyska, M. J.; Warshaw, D. M., The myosin power stroke. *Cell Motility and the Cytoskeleton* **2002**, 51, (1), 1–15.
247. De La Cruz, E. M.; Ostap, E. M., Relating biochemistry and function in the myosin superfamily. *Current Opinion in Cell Biology* **2004**, 16, (1), 61–67.
248. Howard, J., Molecular motors: structural adaptations to cellular functions. *Nature* **1997**, 389, (6651), 561–567.
249. Howard, J.; Hudspeth, A. J.; Vale, R. D., Movement of Microtubules by Single Kinesin Molecules. *Nature* **1989**, 342, (6246), 154–158.
250. Kojima, H.; Muto, E.; Higuchi, H.; Yanagida, T., Mechanics of single kinesin molecules measured by optical trapping nanometry. *Biophys J* **1997**, 73, (4), 2012–22.
251. Hua, W.; Young, E. C.; Fleming, M. L.; Gelles, J., Coupling of kinesin steps to ATP hydrolysis. *Nature* **1997**, 388, (6640), 390–393.
252. Schnitzer, M. J.; Block, S. M., Kinesin hydrolyses one ATP per 8-nm step. *Nature* **1997**, 388, (6640), 386–390.
253. Yildiz, A.; Tomishige, M.; Vale, R. D.; Selvin, P. R., Kinesin walks hand-over-hand. *Science* **2004**, 303, (5658), 676–678.
254. Higuchi, H.; Bronner, C. E.; Park, H. W.; Endow, S. A., Rapid double 8-nm steps by a kinesin mutant. *Embo Journal* **2004**, 23, (15), 2993–2999.
255. Yildiz, A.; Selvin, P. R., Kinesin: walking, crawling or sliding along? *Trends in Cell Biology* **2005**, 15, (2), 112–120.

256. Kuo, S. C.; Gelles, J.; Steuer, E.; Sheetz, M. P., A Model for Kinesin Movement from Nanometer-Level Movements of Kinesin and Cytoplasmic Dynein and Force Measurements. *Journal of Cell Science* **1991**, 135–138.
257. Wang, Z. H.; Khan, S.; Sheetz, M. P., Different Patterns of Kinesin and Cytoplasmic Dynein Movement - a Single Mechanism. *Biophysical Journal* **1995**, 68, (4), S328-S328.
258. Wang, Z. H.; Sheetz, M. P., One-dimensional diffusion on microtubules of particles coated with cytoplasmic dynein and immunoglobulins. *Cell Structure and Function* **1999**, 24, (5), 373–383.
259. Mallik, R.; Carter, B. C.; Lex, S. A.; King, S. J.; Gross, S. P., Cytoplasmic dynein functions as a gear in response to load. *Nature* **2004**, 427, (6975), 649–652.
260. Sakakibara, H.; Kojima, H.; Sakai, Y.; Katayama, E.; Oiwa, K., Inner-arm dynein of Chlamydomonas flagella is a single-headed processive motor. *Nature* **1999**, 400, (6744), 586–590.
261. Gee, M.; Vallee, R., The role of the dynein stalk in cytoplasmic and flagellar motility. *European Biophysics Journal with Biophysics Letters* **1998**, 27, (5), 466–473.
262. Block, S. M.; Blair, D. F.; Berg, H. C., Compliance of Bacterial Flagella Measured with Optical Tweezers. *Nature* **1989**, 338, (6215), 514–518.
263. Berry, R. M.; Berg, H. C., Absence of a barrier to backwards rotation of the bacterial flagellar motor demonstrated with optical tweezers. *Proceedings of the National Academy of Sciences of the United States of America* **1997**, 94, (26), 14433–14437.
264. Tadir, Y.; Wright, W. H.; Vafa, O.; Ord, T.; Asch, R. H.; Berns, M. W., Force Generated by Human Sperm Correlated to Velocity and Determined Using a Laser Generated Optical Trap. *Fertility and Sterility* **1990**, 53, (5), 944–947.
265. McCord, R. P.; Yukich, J. N.; Bernd, K. K., Analysis of force generation during flagellar assembly through optical trapping of free-swimming Chlamydomonas reinhardtii. *Cell Motility and the Cytoskeleton* **2005**, 61, (3), 137–144.
266. Gilad, R.; Porat, A.; Trachtenberg, S., Motility modes of Spiroplasma melliferum BC3: a helical, wall-less bacterium driven by a linear motor. *Molecular Microbiology* **2003**, 47, (3), 657–669.
267. König, K.; Svaasand, L.; Liu, Y. G.; Sonek, G.; Patrizio, P.; Tadir, Y.; Berns, M. W.; Tromberg, B. J., Determination of motility forces of human spermatozoa using an 800 nm optical trap. *Cellular and Molecular Biology* **1996**, 42, (4), 501–509.
268. Schutze, K.; Clementsengewald, A.; Ashkin, A., Zona Drilling and Sperm Insertion with Combined Laser Microbeam and Optical Tweezers. *Fertility and Sterility* **1994**, 61, (4), 783–786.
269. Patrizio, P.; Liu, Y. G.; Sonek, G. J.; Berns, M. W.; Tadir, Y., Effect of pentoxifylline on the intrinsic swimming forces of human sperm assessed by optical tweezers. *Journal of Andrology* **2000**, 21, (5), 753–756.
270. Yagi, K., The mechanical and colloidal properties of Amoeba protoplasm and their relations to the mechanism of amoeboid movement. *Comp Biochem Physiol* **1961**, 3, 73–91.
271. Cohen, D., Ferromagnetic Contamination in Lungs and Other Organs of Human Body. *Science* **1973**, 180, (4087), 745–748.
272. Valberg, P. A.; Meyrick, B.; Brain, J. D.; Brigham, K. L., Phagocytic and Motile Properties of Endothelial-Cells Measured Magnetometrically - Effects of Endotoxin. *Tissue & Cell* **1988**, 20, (3), 345–354.
273. Valberg, P. A.; Butler, J. P., Magnetic Particle Motions within Living Cells - Physical Theory and Techniques. *Biophysical Journal* **1987**, 52, (4), 537–550.
274. Wang, N.; Butler, J. P.; Ingber, D. E., Mechanotransduction across the Cell-Surface and through the Cytoskeleton. *Science* **1993**, 260, (5111), 1124–1127.
275. Huang, H. D.; Kamm, R. D.; Lee, R. T., Cell mechanics and mechanotransduction: pathways, probes, and physiology. *American Journal of Physiology-Cell Physiology* **2004**, 287, (1), C1–C11.
276. Ikai, A.; Afrin, R.; Sekiguchi, H.; Okajima, T.; Alam, M. T.; Nishida, S., Nano-mechanical methods in biochemistry using atomic force microscopy. *Current Protein & Peptide Science* **2003**, 4, (3), 181–193.
277. Galbraith, C. G.; Yamada, K. M.; Sheetz, M. P., The relationship between force and focal complex development. *Journal of Cell Biology* **2002**, 159, (4), 695–705.
278. Choquet, D.; Felsenfeld, D. P.; Sheetz, M. P., Extracellular matrix rigidity causes strengthening of integrin-cytoskeleton linkages. *Cell* **1997**, 88, (1), 39–48.
279. Kusumi, A.; Sako, Y.; Fujiwara, T.; Tomishige, M., Application of laser tweezers to studies of the fences and tethers of the membrane skeleton that regulate the movements of plasma membrane proteins. *Methods in Cell Biology*, Vol 55 **1998**, 55, 173–194.
280. Peters, I. M.; van Kooyk, Y.; van Vliet, S. J.; de Grooth, B. G.; Figdor, C. G.; Greve, J., 3D single-particle tracking and optical trap measurements on adhesion proteins. *Cytometry* **1999**, 36, (3), 189–194.
281. Falk, J.; Thoumine, O.; Dequidt, C.; Choquet, D.; Faivre-Sarrailh, C., NrcAM coupling to the cytoskeleton depends on multiple protein domains and partitioning into lipid rafts. *Molecular Biology of the Cell* **2004**, 15, (10), 4695–4709.

282. Sako, Y.; Nagafuchi, A.; Tsukita, S.; Takeichi, M.; Kusumi, A., Cytoplasmic regulation of the movement of E-cadherin on the free cell surface as studied by optical tweezers and single particle tracking: Corraling and tethering by the membrane skeleton. *Journal of Cell Biology* **1998**, 140, (5), 1227–1240.
283. Oddershede, L.; Flyvbjerg, H.; Berg-Sorensen, K., Single-molecule experiment with optical tweezers: improved analysis of the diffusion of the lambda-receptor in E-coli's outer membrane. *Journal of Physics-Condensed Matter* **2003**, 15, (18), S1737-S1746.
284. Sako, Y.; Kusumi, A., Barriers for Lateral Diffusion of Transferrin Receptor in the Plasma-Membrane as Characterized by Receptor Dragging by Laser Tweezers - Fence Versus Tether. *Journal of Cell Biology* **1995**, 129, (6), 1559–1574.
285. Tomishige, M.; Sako, Y.; Kusumi, A., Regulation mechanism of the lateral diffusion of band 3 in erythrocyte membranes by the membrane skeleton. *Journal of Cell Biology* **1998**, 142, (4), 989–1000.
286. Arya, M.; Lopez, J. A.; Romo, G. M.; Cruz, A. A.; Kasirer-Friede, A.; Shattil, S. J.; Anvari, B., Glycoprotein Ib-IX-mediated activation of integrin alpha(IIb)beta(3): effects of receptor clustering and von Willebrand factor adhesion. *Journal of Thrombosis and Haemostasis* **2003**, 1, (6), 1150–1157.
287. Stoltz, J. F.; Dumas, D.; Wang, X.; Payan, E.; Mainard, D.; Paulus, F.; Maurice, G.; Netter, P.; Muller, S., Influence of mechanical forces on cells and tissues. *Biorheology* **2000**, 37, (1–2), 3–14.
288. Ermilov, S. A.; Murdock, D. R.; El-Daye, D.; Brownell, W. E.; Anvari, B., Effects of salicylate on plasma membrane mechanics. *Journal of Neurophysiology* **2005**, 94, (3), 2105–2110.
289. Zahn, M.; Seeger, S., Optical tweezers in pharmacology. *Cellular and Molecular Biology* **1998**, 44, (5), 747–761.
290. Ashkin, A.; Schutze, K.; Dziedzic, J. M.; Euteneuer, U.; Schliwa, M., Force Generation of Organelle Transport Measured In vivo by an Infrared-Laser Trap. *Nature* **1990**, 348, (6299), 346–348.
291. Welte, M. A.; Gross, S. P.; Postner, M.; Block, S. M.; Wieschaus, E. F., Developmental regulation of vesicle transport in Drosophila embryos: Forces and kinetics. *Cell* **1998**, 92, (4), 547–557.
292. Schneckenburger, H.; Hendinger, A.; Sailer, R.; Strauss, W. S. L.; Schmitt, M., Laser-assisted optoporation of single cells. *Journal of Biomedical Optics* **2002**, 7, (3), 410–416.
293. Aufderheide, K. J.; Du, Q.; Fry, E. S., Directed Positioning of Micronuclei in Paramecium-Tetraurelia with Laser Tweezers - Absence of Detectable Damage after Manipulation. *Journal of Eukaryotic Microbiology* **1993**, 40, (6), 793–796.
294. Liu, X.; Wang, H.; Li, Y.; Tang, Y.; Liu, Y.; Hu, X.; Jia, P.; Ying, K.; Feng, Q.; Guan, J.; Jin, C.; Zhang, L.; Lou, L.; Zhou, Z.; Han, B., Preparation of single rice chromosome for construction of a DNA library using a laser microbeam trap. *J Biotechnol* **2004**, 109, (3), 217–26.
295. Conia, J.; Voelkel, S., Optical Manipulations of Human Gametes. *Biotechniques* **1994**, 17, (6), 1162–1165.
296. Leitz, G.; Weber, G.; Seeger, S.; Greulich, K. O., The Laser Microbeam Trap as an Optical Tool for Living Cells. *Physiological Chemistry and Physics and Medical Nmr* **1994**, 26, (1), 69–88.
297. Thalhammer, S.; Lahr, G.; Clement-Sengewald, A.; Heckl, W. M.; Burgemeister, R.; Schutze, K., Laser micro-tools in cell biology and molecular medicine. *Laser Physics* **2003**, 13, (5), 681–691.
298. Leitz, G.; Schnepf, E.; Greulich, K. O., Micromanipulation of Statoliths in Gravity-Sensing Chara Rhizoids by Optical Tweezers. *Planta* **1995**, 197, (2), 278–288.
299. Lee, H.; Purdon, A. M.; Westervelt, R. M., Micromanipulation of biological systems with microelectromagnets. *Ieee Transactions on Magnetics* **2004**, 40, (4), 2991–2993.
300. Thoumine, O.; Kocian, P.; Kottelat, A.; Meister, J. J., Short-term binding of fibroblasts to fibronectin: optical tweezers experiments and probabilistic analysis. *European Biophysics Journal with Biophysics Letters* **2000**, 29, (6), 398–408.
301. Liang, M. N.; Smith, S. P.; Metallo, S. J.; Choi, I. S.; Prentiss, M.; Whitesides, G. M., Measuring the forces involved in polyvalent adhesion of uropathogenic Escherichia coli to mannose-presenting surfaces. *Proceedings of the National Academy of Sciences of the United States of America* **2000**, 97, (24), 13092–13096.
302. Grimbergen, J. A.; Visscher, K.; Demesquita, D. S. G.; Brakenhoff, G. J., Isolation of Single Yeast-Cells by Optical Trapping. *Yeast* **1993**, 9, (7), 723–732.
303. Huber, R.; Burggraf, S.; Mayer, T.; Barns, S. M.; Rossnagel, P.; Stetter, K. O., Isolation of a Hyperthermophilic Archaeum Predicted by in-Situ Rna Analysis. *Nature* **1995**, 376, (6535), 57–58.
304. Bronkhorst, P. J. H.; Streekstra, G. J.; Grimbergen, J.; Nijhof, E. J.; Sixma, J. J.; Brakenhoff, G. J., A new method to study shape recovery of red blood cells using multiple optical trapping. *Biophysical Journal* **1995**, 69, (5), 1666–1673.
305. Bayouduh, S.; Mehta, M.; Rubinsztein-Dunlop, H.; Heckenberg, N. R.; Critchley, C., Micromanipulation of chloroplasts using optical tweezers. *Journal of Microscopy-Oxford* **2001**, 203, 214–222.
306. Brandao, M. M.; Fontes, A.; Barjas-Castro, M. L.; Barbosa, L. C.; Costa, F. F.; Cesar, C. L.; Saad, S. T. O., Optical tweezers for measuring red blood cell elasticity: application to the study of drug response in sickle cell disease. *European Journal of Haematology* **2003**, 70, (4), 207–211.

- 307. Barjas-Castro, M. L.; Brandao, M. M.; Fontes, A.; Costa, F. F.; Cesar, C. L.; Saad, S. T. O., Elastic properties of irradiated RBCs measured by optical tweezers. *Transfusion* **2002**, 42, (9), 1196–1199.
- 308. Yin, S. H.; Zhang, X. Q.; Zhan, C.; Wu, J. T.; Xu, J. C.; Cheung, J., Measuring single cardiac myocyte contractile force via moving a magnetic bead. *Biophysical Journal* **2005**, 88, (2), 1489–1495.
- 309. Curtis, J. E.; Grier, D. G., Structure of optical vortices. *Physical Review Letters* 90, (13): Art. No. 133901 APR 4 **2003**.
- 310. Edelstein, R. L.; Tamanaha, C. R.; Sheehan, P. E.; Miller, M. M.; Baselt, D. R.; Whitman, L. J.; Colton, R. J., The BARC biosensor applied to the detection of biological warfare agents. *Biosensors & Bioelectronics* **2000**, 14, (10–11), 805–813.

Handbook of Molecular Force Spectroscopy

Noy, A. (Ed.)

2008, XII, 300 p. 150 illus., Hardcover

ISBN: 978-0-387-49987-1